MULTIPHOTON LASER SPECTROSCOPY AND PHOTOCHEMISTRY OF ELECTRONICALLY EXCITED HCl.

by

Murray Arthur Brown

A thesis presented for the degree of Doctor of Philosophy
in the Faculty of Science at the University of Edinburgh,
1987.

DECLARATION

I hereby declare that this thesis has been composed by me, and that the work described in it is my own and was carried out at the University of Edinburgh, except where due acknowledgement is made.

Signed: _

Date: 28/10/84

ACKNOWLEDGEMENTS

I wish to record my gratitude to my supervisor Professor R.J. Donovan for his interest, enthusiasm and suggestions throughout the course of this work. I would like also to thank Dr. P.R.R. Langridge-Smith and Dr. K.P. Lawley for many stimulating and clarifying discussions. My gratitude must also extend to Dr. J.P.T. Wilkinson and the laser group technician, Dr. T. Ridley.

I am indebted to the technical staff of the mechanical, electronic and glass-blowing workshops for their expertise and efficiency. To the S.E.R.C. laser-loan pool for allowing the use of the Quantel Datachrom-5000 laser I am also grateful. In addition I wish to thank the Department of Education for Northern Ireland (D.E.N.I.) for a post-graduate Research Studentship.

It is a pleasure also to thank the other research students in the laser group, not only for their assistance with experiments but particularly for their seemingly endless sense of humour.

Finally, I wish to thank all those who assisted in the production of this thesis particularly Joan Stafford for her excellent transformation of my written script into the finished document.

ABSTRACT

Some spectroscopic and photochemical studies of electronically excited HCl have been performed using laser multiphoton excitation techniques. [2+1] Resonance Enhanced Multiphoton Ionisation [REMPI] has been used to study various electronically excited states of HCl in the 75,000-90,000 cm^{-1} energy region. Most of the diffuse $^1\pi$ and $^3\pi$ symmetry 'Rydberg' states are not detected in REMPI due to their rapid predissociation. In contrast, the f $^3\Delta_2$ and F $^1\Delta_2$ 'Rydberg' states are longer lived and give rise to strong signals in the REMPI spectrum. A detailed spectroscopic study of the F $^1\Delta_2$ state in HCl and DCl has been performed. Comparison of the experimental line intensities with those predicted by two-photon line strength theory is made. Vibrational levels above v'=8 of the B $^1\Sigma^+$ 'Ion-pair' state have also been studied. Where this state interacts with nominally 'Rydberg' states of the same electronic symmetry strong mixing occurs. The 'Ion-pair' state fluoresces in the 230 nm region and to shorter wavelengths, as it makes the transition to the ground state, X $^1\Sigma^+$. Those states which are coupled with the 'Ion-pair' state also give rise to this characteristic emission in the same wavelength region. Fluorescence spectroscopy is shown to be a useful means of studying this interstate coupling.

The photochemistry of electronically excited HCl in the presence of Xe and Kr rare gases has also been studied. Reaction occurs leading to the formation of the respective rare gas chloride exciplex. The results obtained are compared to the reactions of electronically excited Xe and Kr with ground state HCl.

Finally, photochemical production of HCl and HBr in low vibrational levels of the respective 'Ion-pair' states, following multiphoton dissociation of C_2H_3Cl and C_2H_3Br respectively, using an ArF (193nm) laser, is discussed.

CONTENTS

CHAPTER 4 MULTIPHOTON IONISATION SPECTROSCOPY OF HYDROGEN CHLORIDE

CHAPTER 5 FLUORESCENCE SPECTROSCOPY OF ELECTRONICALLY EXCITED HCl

CHAPTER 6 REACTIONS OF ELECTRONICALLY EXCITED HCl WITH RARE GASES KRYPTON AND XENON

CHAPTER 7 MULTIPHOTON DISSOCIATION OF C_2H_3Cl and C_2H_3Br - A PHOTOCHEMICAL SOURCE OF B $^1\Sigma^+$ HCl and HBr, RESPECTIVELY

7.3 Results

CHAPTER 1

INTRODUCTION

1.1 MULTIPHOTON PROCESSES - AN OVERVIEW

Most of what is known about the interaction of light with molecules has come from the study of single photon processes such as absorption and emission. With the advent of the laser the observation of many novel and exotic events involving the absorption of more than one photon has been made possible. Two-photon absorption, predicted by Göppert-Mayer [1] as early as 1931, follows a quadratic dependence on the light intensity and can be expected to be difficult to observe with conventional light sources. Brossel et al [2] in 1953 made the first observation of a two-photon absorption in the radio-frequency region of the spectrum. With the development of the laser, two-photon absorption in the visible part of the spectrum became possible. Kaiser and Garrett [3], in 1961, focussed a red ruby laser, lasing at 6943 Å, into a Eu^{2+}-doped CaF_2 crystal and emission of blue light from a two-photon excited band was observed. The advent of the dye laser with attendant tunable, coherent radiation heralded improved detection sensitivity and spectral resolution, turning two-photon absorption into a practical type of spectroscopy. The first experiments were performed with a ruby laser-pumped dye laser source by Bergman and Jortner in 1972 [4]. They studied the two-photon absorption spectrum of anthracene. Vibrationally resolved two-photon spectroscopy of organic molecules was initiated by measurements in crystals at low temperatures. In 1973 Hochstrasser and co-workers published the two-photon spectrum of a biphenyl crystal at 2K using a continuously tunable dye laser pumped by a N_2 laser [5].

Two-photon spectra of gas phase molecules were only obtained as recently as 1974 because, in large measure, of the low particle density in low pressure gases. The feasibility of two-photon spectroscopy of gas phase molecules was demonstrated for the first time using benzene vapour by Hochstrasser et al [6]. Concurrently, Bray et al [7] first demonstrated that two-photon excitation was a good method for inducing electronic transitions in dilute diatomic gases. Using fluorescence excitation they were able to resolve the rotational structure of the $A\ {}^2\Sigma^+ - X\ {}^2\Pi$ transition in NO, despite the rather large bandwidth ($0.4cm^{-1}$) of the exciting laser used. The availability of intense tunable ultra-violet (UV) laser light subsequently allowed the use of two-photon absorption for the excitation of single rotational lines of electronic transitions in the vacuum ultra-violet (VUV), as first shown by Filseth et al [8] for CO and N_2.

The first observation of multiphoton ionisation [MPI] in the form of a spark at the focal point of a focussed ruby laser was made by Maker et al [9] in 1964. The demonstration of multiphoton ionisation as a new spectroscopic tool was credited to Johnson et al [10] for work on NO, and to Dalby et al [11] for their work on I_2, both in 1975.

Measurement of a multiphoton absorption as suggested above can be performed in a variety of ways. Classically the measurement of absorption requires measuring the light intensity first in front of the sample and then after passing through it. Qualitatively, it is clear that absorption measurements in multiphoton spectroscopy may be possible for samples of high density, i.e. liquids and solids. It is not feasible for gas-phase spectroscopy, since it is impossible to keep the laser light focussed over the then necessary long absorption path.

One convenient and sensitive method for measurement of two-photon spectra is the detection of fluorescence from the electronically excited molecules. For example, as a consequence of two-photon absorption most molecules emit a photon at about twice the energy of those absorbed. These emitted photons can be detected with high sensitivity.

After a molecule has been excited in an intense radiation field by two, three or more photon-absorption, it is very likely to absorb further photons, which result finally in its ionisation. Thus, another sensitive technique for the detection of multiphoton absorption processes in gases is based on the subsequent ionisation of the molecule after transition to an excited electronic state. The interesting feature of this multiphoton ionisation, from a spectroscopic point of view, is the resonance enhancement by resonant intermediate states. As the ionisation efficiency is strongly enhanced when the photon energy is in resonance with real intermediate states, scanning the wavelength of the laser leads to a modulation of the ion current, which reflects the spectrum of the intermediate states. Thus it is possible to acquire the intermediate state (multiphoton) spectrum by measuring the ion current.

As compared to fluorescence, the ionisation technique offers much greater sensitivity due to the higher collection efficiency of charged particles (~100% compared to ~5% for photon collection). In addition, problems arising from the detection of unwanted scattered laser light do not arise.

S.H. Lin et al [18] discuss various other less commonly used techniques for measuring two-photon absorptions, including photoacoustic spectroscopy and thermal blooming measurements.

Since the pioneering experiments mentioned, multiphoton excitation and ionisation have now become a powerful tool in the study of both atomic and molecular systems. High power lasers commonly used in multiphoton processes not only increase the signal-to-noise ratio thereby making processes of very high order observable but also provide extremely high energy and quantum state selectivity.

The study of excited electronic state spectroscopy [12] and photochemistry [13] by multiphoton techniques is of direct relevance to this work. The high-lying excited electronic states of small molecular species are of considerable interest to spectroscopists, photochemists and those studying the dynamics of chemical reactions. Absorption spectroscopy has long been the traditional method for studying the highly excited electronic states of small gas-phase molecular species. However, the experimental study of the latter are hindered by the lack of sufficiently intense, tunable, monochromatic VUV light sources, by the operational difficulties working at such wavelengths and by the spectral congestion that arises because of the high density of accessible electronic states. Moreover, one-photon absorption spectroscopy generally reveals only a fraction of the total number of excited states belonging to a particular molecule, restricted as it is by the selection rules that govern electric dipole- allowed transitions and also by the constraints of the Franck-Condon principle.

There are, however, possible advantages to be gained from using multiphoton excitation methods. Typically multiphoton absorption cross-sections are small for a representative molecule (typical values for coherent two- and three-photon cross-sections are, respectively, $10^{-51}cm^4s$ and $10^{-82}cm^6s^2$ [14]). Thus, high light intensities are essential for the creation of a significant excited state population. The necessary intensities can be obtained by focussing the output from an excimer or Nd:YAG-pumped tunable dye laser (see Chapter 3). This focussing requirement is in practice incompatible with the relatively long path lengths required for absorption detection methods. As has been discussed, multiphoton resonances can be detected by various means, commonly, by the observation of emission from the excited state, or, alternatively, by the structure the resonances provide in the multiphoton ionisation [MPI] spectrum.

The excited electronic states which dominate the one-photon absorption spectra of small molecules are those which may be reached by electric dipole-allowed transitions from the ground electronic state. The parity selection rules ensure that only g <-> u transitions occur in molecules with a centre of symmetry. Hence gerade (g) excited states of molecules that possess a gerade (g) ground state are not observed in VUV absorption. However g <-> g, u <-> u excitations are possible via coherent, two-photon excitation. A classic illustration of this is the [2+1] MPI spectroscopy of the E,F $^1\Sigma^+_g$ double-minimum state of H_2 [15]. Coherent N-photon excitation also provides a means of populating excited states whose Λ quantum number differs from that of the ground state by up to ±N. Good examples of this are to be found in the observation of the D $^1\Delta$ - X $^1\Sigma^+$ two-photon transition in CO [16], the F $^1\Delta_2$ - X $^1\Sigma^+$ two-photon transition in HCl discussed in this work and that of a $^1\Phi_u$ - X $^1\Sigma_g^+$ three-photon transition in C_2H_2, observed by Ashfold et al [17]. If a multiphoton excitation spectrum shows resolved rotational structure then considerable spectroscopic information can be derived, even the excited state symmetry. By their very nature, multiphoton excitation techniques are sensitive to the lifetime of the excited state and the observed spectrum is often a manifestation of this. This behaviour will be discussed more fully in Chapter 2.

In summary, the past decade has seen the very rapid growth in the study of multiphoton phenomena, one of the most interesting fields of research made possible by the development of powerful, pulsed lasers. The field is still in a stage of rapid development, with new observations and theories being documented at an impressive rate. Nonetheless, there are several noteworthy review articles which give excellent accounts of the present 'state of the art' [12-14,18-23].

In the work described in this thesis, multiphoton laser excitation techniques have been addressed to the study of the spectroscopy and photochemistry of electronically excited HCl. Spectroscopic studies were made using two-photon fluorescence excitation, dispersed fluorescence and resonance-enhanced multiphoton ionisation methods. The experimental study of the interaction between the 'Ion-pair' state and the nominally 'Rydberg' states of the same electronic symmetry has been of particular interest. The associated photochemical studies are concerned primarily with the reactions and quenching of electronically excited HCl with ground electronic state rare gas atoms.

Following this introductory Chapter, Chapter 2 discusses the essentials of two-photon absorption theory and some important features of multiphoton, particularly ionisation, spectroscopy. Chapter 3 summarises the experimental apparatus and techniques used in the course of this work. Chapter 4 illustrates in some detail the application of multiphoton ionisation spectroscopy to the spectroscopic study of electronically excited HCl both in a static room temperature gas sample (298K) and one cooled to low temperatures (<30K) in a supersonic free jet expansion. Chapter 5 follows on naturally, and is devoted to the study of the perturbative interactions between the 'Ion-pair' state and states of the same electronic symmetry using fluorescence spectroscopy. Chapter 6 discusses the reactions and quenching of electronically excited HCl with rare gases.

Finally, in Chapter 7, the photochemical production of electronically excited HCl by laser multiphoton dissociation methods is discussed, and its relation to results in the previous chapters shown.

1.2 REFERENCES

1. M.Göppert-Mayer, Ann. Phys., 9, 273 (1931).
2. J. Brossel, B. Cagnac and A. Kastler, C.R. Acad. Sci. [Paris], 237, 984 (1953).
3. W. Kaiser and C.G.B. Garrett, Phys. Rev. Lett., 7, 229 (1961).
4. A. Bergman and J. Jortner, Chem. Phys. Lett., 15, 309 (1972).
5. R.M. Hochstrasser, H.N. Sung and J.E. Wessel, J. Chem. Phys., 58, 4694 (1973).
6. R.M. Hochstrasser, J.E. Wessel and H.N. Sung, J. Chem. Phys., 60, 317 (1974).
7. R.G. Bray, R.M. Hochstrasser and J.E. Wessel, Chem. Phys. Lett., 27, 167 (1974).
8. S.V. Filseth, R. Wallenstein and H. Zacharias, Opt. Commun., 23, 231 (1977).
9. P.D. Maker, R.W. Terhune and C.M. Savage in 'Quantum Electronics', p.1559 (Columbia University Press, New York, 1964).
10. P.M. Johnson, M.R. Berman and D. Zakheim, J. Chem. Phys., 62, 2500 (1975).
11. G. Petty, C. Tai and F.W. Dalby, Phys. Rev. Lett., 34, 1207 (1975).
12. M.N.R. Ashfold, Mol. Phys., 58, 1 (1986).
13. R.J. Donovan, in 'Gas Kinetics and Energy Transfer'. Specialist Periodical Reports, Vol. 4, p.117, edited by P.G. Ashmore and R.J. Donovan,

(Royal Society of Chemistry, 1981).

14. P.M. Johnson and C.E. Otis, Ann. Rev. Phys. Chem., 32, 139 (1981).

15. E.E. Marinero, R. Vasudev and R.N. Zare, J. Chem. Phys., 78, 692 (1983).

16. C. Kittrell, S. Cameron, L. Butler, R.W. Field and R.F. Barrow, J. Chem. Phys., 78, 3623 (1983).

17. M.N.R. Ashfold, R.N. Dixon, J.D. Prince and B. Tutcher, Mol. Phys., 56, 1185 (1985).

18. S.H. Lin, Y. Fugimura, H.J. Neusser and E.W. Schlag, in 'Multiphoton Laser Spectroscopy of Molecules.', Quantum Electronics-Principles and Applications, (Academic Press, 1984).

19. R.L. Swofford and A.C. Albrecht, Ann. Rev. Phys. Chem., 29, 421 (1978).

20. D.M. Friedrich and W.M. McClain, Ann. Rev. Phys. Chem., 31, 559 (1980).

21. 'Advances in Multiphoton Processes and Spectroscopy, Vol. 1', edited by S.H. Lin, (World Scientific Publishing Co. Ltd., 1984).

22. R.R. Birge, p.109, (Chapter 2) and D.H. Parker, p.233, (Chapter 4) in 'Ultrasensitive Laser Spectroscopy', edited by D.S. Kliger (Academic Press, 1983).

23. J.H. Glownia, A. Hartford. Jnr, G.W. Loge, R.K. Sander, J.J. Tiee and F.B. Wampler, p.105, (Chapter 4) in 'Advances in Laser Spectroscopy Vol. 2' edited by B.A. Garetz and J.R. Lombardi, (John Wiley and Sons, Ltd., 1983).

CHAPTER 2

MULTIPHOTON PROCESSES - SOME THEORETICAL CONSIDERATIONS

2.1 INTRODUCTION

In this Chapter a brief description of the important features observed in any multiphoton excitation process will be given. Two-photon absorption theory is particularly relevant to this study of electronically excited HCl. Its application in the determination of rotational line intensities observed during two-photon transitions will be summarised. Finally, a discussion of multiphoton ionisation phenomena is provided. In particular, the important factors that can contribute to line broadening of transitions in a multiphoton ionisation spectrum are considered.

2.2 TWO-PHOTON ABSORPTION THEORY

Two-photon absorption spectroscopy is the study of a non-linear optical phenomenon. Moreover, for quite some time now, there has been considerable interest in not just two- but multiphoton excitation processes. The use of two-photon excitation techniques for the study of electronically excited states is of interest for several reasons, a number of which have been mentioned already in Chapter 1. These are now considered further.

1. The selection rules for two-photon absorption permit the creation of excited states that cannot be accessed by one photon, electric dipole-allowed selection rules. Thus, if a molecule has a ground electronic state of gerade (g) symmetry and orbital angular momentum Λ, then gerade (g) excited states with a change in orbital angular momentum $\Delta\Lambda = 0, \pm 1, \pm 2$ are allowed by two-photon absorption.

   Two-photon absorption can also create two-electron excitations in molecules which would otherwise be forbidden or be allowed only very weakly. This excitation may involve two orbital promotions of one electron, or promotion for each of two electrons.

2. Two-photon spectra of gases may be obtained free of Doppler broadening [22] by using tunable, counter-propagating laser beams of narrow line-width [1-3]. In this way, measurement of natural line-widths in polyatomic molecules is possible. This is, of course, of great interest to those studying radiationless processes in molecules. In addition, the high resolution spectroscopic measurements permitted by two-photon Doppler-free techniques allows research into molecular perturbation effects hitherto undetectable.

3. Optical polarisation methods available in two-photon spectroscopy make it possible to identify transition symmetries by completely empirical means [4].

4. Excited electronic states lying at energies deep in the VUV can be studied by two-photon excitation, with fewer experimental difficulties, using tunable, high intensity, pulsed UV laser radiation.
5. Finally, the intensity from pulsed lasers used for two-photon excitation of electronically excited states is often high enough for subsequent photon absorption and ionisation of the molecule to occur. Thus, the application of resonance-enhanced multiphoton ionisation (REMPI) spectroscopy is being pursued.

The basic physics of two-photon absorption, in particular the development of two-photon rotational line-strength formulae has been described by several workers [4-9]. Most of the theory described in the following pages and in Appendix I is a summary of the treatment adopted by McClain and Harris [4] which emphasises the tensorial nature of two-photon absorption. These workers used a semi-classical perturbation theory for the interaction of radiation with matter and carried it to second order to represent correctly the route from the second order perturbed wave function of the states being considered to the observable two-photon absorption.

Consider a two-photon vibronic transition from an initial state $|g\rangle = |JKM\rangle|EV\rangle$ to a final state $|f\rangle = |J'K'M'\rangle|E'V'\rangle$ where J, K and M are rotational quantum numbers of a rotating symmetric top molecule, with E and

V, the corresponding electronic and vibrational quantum numbers. A typical pathway for two-photon absorption via a virtual, intermediate state $|k\rangle$ is as shown in Figure 2.1. Note that, the molecule by virtue of its symmetry possesses two identical principal moments of inertia. The symmetric rotor case includes, as special limiting cases, the spherical rotor with three identical principal moments of inertia, and the simple diatomic rotor with a vanishing moment around the diatomic axis and two equal moments perpendicular to it.

The two-photon absorptivity, δ_{gf}, as defined by McClain and Harris [4] is given by:

$$\delta_{gf} = 8\pi^3 \alpha \omega_1 \omega_2 g_m(\omega_1+\omega_2)|S_{gf}|^2 \qquad 2.1$$

where $\alpha = q^2/4\pi\varepsilon_o\hbar c$ is a dimensionless fine-structure constant with value $\sim 1/137$.

q is the charge on an electron

ε_o is the permittivity constant

h is Planck's constant, $\hbar = h/2\pi$

c is the speed of light

ω_1 and ω_2 are the frequencies of the two photons (in Hz)

$g_m(\omega_1+\omega_2)$ is the absorption line shape.

S_{gf} is given by:

$$S_{gf} = \sum_k \left\{ \frac{\langle g|\underline{e}_1\cdot\underline{r}|k\rangle\langle k|\underline{e}_2\cdot\underline{r}|f\rangle}{\omega_{kg}-\omega_1+i\Gamma_k} + \frac{\langle g|\underline{e}_2\cdot\underline{r}|k\rangle\langle k|\underline{e}_1\cdot\underline{r}|f\rangle}{\omega_{kg}-\omega_2+i\Gamma_k} \right\} \qquad 2.2$$

where $\underline{e}_1$ and $\underline{e}_2$ are the polarisation vectors of the

FIGURE 2.1 Typical pathway for two-photon absorption via a virtual, intermediate state |k>.

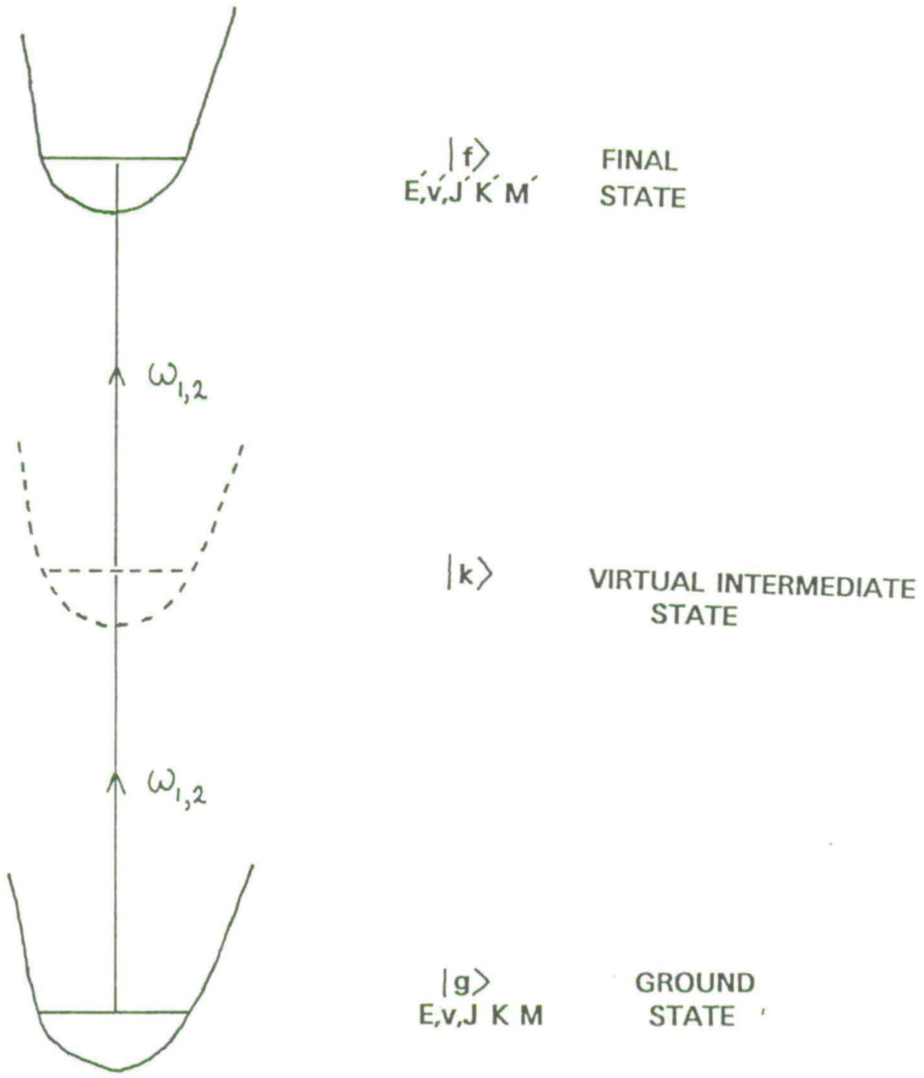

photons ω_1 and ω_2. Here $\underline{r}$ represents the vectorial dipole moment operator of the molecule under consideration.

State $|k\rangle$ is the virtual intermediate state which is located above the ground state at an energy difference ω_{kg} and with a homogeneous half-width $i\Gamma_k$.

In defining the absorptivity, δ_{gf}, we have created a measurable quantity that is independent of optical intensity. It is still not a molecular property as it contains the polarisation vectors $\underline{e}_1$ and $\underline{e}_2$ of the laser light.

To separate the polarisation, equation 2.2 can be re-written as:

$$S_{gf} = \sum_{a,b=x,y,z} \underline{e}_{1a}\cdot\mathcal{S}^{gf}_{ab}\cdot\underline{e}_{2b} \qquad 2.3$$

where $\mathcal{S}^{gf}_{ab}$ is the two-photon transition tensor in molecular co-ordinates defined as:

$$\mathcal{S}^{gf}_{ab} = \sum_k \left\{ \frac{\langle g|\underline{r}_a|k\rangle\langle k|\underline{r}_b|f\rangle}{\omega_{kg}-\omega_1+i\Gamma_k} + \frac{\langle g|\underline{r}_b|k\rangle\langle k|\underline{r}_a|f\rangle}{\omega_{kg}-\omega_2+i\Gamma_k}, \right\} \qquad 2.4$$

Vectors $\underline{e}_1$ and $\underline{e}_2$ are usually expressed in the laboratory co-ordinate system, while the vectors $\underline{r}$ are in the molecular system. A co-ordinate transformation must be included, thus:

$$S_{gf} = \sum_{a,b=x,y,z} \underline{e}_{1A}\cdot\ell_{Aa}\cdot\mathcal{S}_{ab}\cdot\ell_{bB}\cdot\underline{e}_{2B} \qquad 2.5$$

where ℓ_{Aa} is the cosine of the angle between axis A of the laboratory system and axis a of the molecular system. The transformation:

$$\mathcal{S}_{AB} = \ell_{Aa} \cdot \mathcal{S}_{ab} \cdot \ell_{bB} \qquad 2.6$$

is the defining property of a second rank Cartesian tensor, so the intrinsic molecular quantity governing two-photon absorption is a transition tensor $\mathcal{S}$. $\mathcal{S}$ is a quantum mechanical matrix element between ground state $|g>$ and the final state $<f|$ of a two-photon transition operator defined as:

$$\hat{\mathcal{S}}_{ab} = \sum_{k} \left\{ \frac{\underline{r}_a |k><k| \underline{r}_b}{\omega_{kg} - \omega_1 + i\Gamma_k} + \frac{\underline{r}_b |k><k| \underline{r}_a}{\omega_{kg} - \omega_2 + i\Gamma_k} \right\} \qquad 2.7$$

The calculation of the explicit dependence of the two-photon absorption tensor elements upon the rotational quantum number is greatly facilitated by linear transformation from the Cartesian representation of the tensor into a representation known as 'spherical' and from there into the 'irreducible representation'. Taking the scalar products of the tensor elements with the polarisation vectors allows the formation of a probability amplitude. Again this is done by transferring the Cartesian polarisation vectors into the irreducible representation. The result is squared and summed over the M degeneracies present to arrive at δ, the absorptivity of the transition. A discussion of the procedures involved may be found in Appendix I.

Rotational selection rules for two-photon transitions can be derived [4] and are summarised below:

For a $0^+ - 0^+$ electronic transition in HCl, with Hund's case (c) coupling [10,11], the change in the rotational quantum number $\Delta J = 0, \pm 2$ is allowed. Thus O,Q and S branches may be expected to occur. For a $1 - 0^+$ or a $2 - 0^+$ transition, $\Delta J = 0, \pm 1, \pm 2$ is allowed. Hence, O, P, Q, R and S branches should be observed. In the case of a $0^- - 0^+$ transition, the transition proceeds with the selection rule $\Delta J = 0, \pm 1$ only for photons of markedly different frequencies and of different polarisations from each other. The selection rules for electronic states of Hund's case (a) remain the same. In summary:

Hund's (case(a)), case(c)

Electronic transition	Rotational selection rule
$(^1\Sigma^+),0^+$ <-> $(^1\Sigma^+),0^+$	$\Delta J = 0, \pm 2$
$(^1\pi),1$ <-> $(^1\Sigma^+),0^+$ or $(^1\Delta),2$ <-> $(^1\Sigma^+),0^+$	$\Delta J = 0, \pm 1, \pm 2$
$(^1\Sigma^-),0^-$ <-> $(^1\Sigma^+),0^+$	$\Delta J = 0, \pm 1$

Using the formalism of Bray and Hochstrasser [6] or that of Maïnos et al [7] or most recently that of Zare et al [9] rotational line-strength formulae have been derived in terms of the orbital angular momentum and rotational angular momentum quantum numbers, Λ and J, respectively, for molecules following Hund's case (a) coupling. For intermediate case (a), case (b) coupling the treatments of Maïnos and Le Duff [8] or Halpern et al [6] can be applied. For the spectral simulations described in Chapter 4, HCl was considered to have its electronic ancestry in a Hund's case (a) state and thus the tabulated line-strength formulae given by Bray and Hochstrasser [6] or Zare et al [9] are extremely useful for incorporation directly into a computer program. The relative line intensities of individual ro-vibronic lines can be obtained from:

$$I = CS_{J'J''}\exp(-E_{ROT}/kT) \qquad 2.8$$

where C is a proportionality factor independent of the rotational transition, $S_{J'J''}$ is the rotational two-photon absorption line strength, and $\exp(-E_{ROT}/kT)$ is the Boltzmann factor, with k Boltmann's constant, and T the temperature in Kelvin.

2.3 RESONANCE ENHANCED MULTIPHOTON IONISATION (REMPI) SPECTROSCOPY.

One of the most useful recent developments in molecular spectroscopy has been the ability to observe transitions where more than one photon is absorbed simultaneously. A spectrum of these multiphoton transitions often displays characteristics quite different from those of a single photon spectrum because of altered selection rules and transition intensities. Thus potentially, new states, vibrations, and rotations are seen in multiphoton spectra. Analysis of the latter can then provide a much more complete understanding of the excited state structure.

The experiments performed in the work described here involve multiphoton spectroscopy with fluorescence detection and ionisation detection of the excited electronic state (HCl in this case) formed by a multiphoton transition. Thus, the primary concern is in deriving information from the multiphoton absorption step. Events subsequent to this which do not appear directly in the spectrum concern us in as much as they may affect intensities. Hence, rotational line intensities predicted by two-photon absorption theory can be usefully compared with those experimentally observed.

The simplest and most common MPI experiment consists of focussing a tunable pulsed dye laser beam into a low pressure gas and then monitoring the consequences. Any electrons or ions created by the laser pulse are collected, the current amplified and the resultant signal is recorded as a function of excitation wavelength. When the laser photon energy is some small integral fraction of a bound-bound transition energy from the ground state of the molecule, a significant increase in signal (the resonance enhancement, discussed in Chapter 1) is seen in the spectrum.

Several basic molecular parameters must be kept in mind before attempting to record a multiphoton spectrum. Typical absorption cross-sections for a multiphoton process are small $\sim 10^{-51} cm^4 s$ for a two-photon absorption and $\sim 10^{-82} cm^6 s^2$ for a resonant three-photon absorption [12,13]. Very high light fluxes are needed to achieve a significant transition probability and hence, lasers are the only viable choice as a light source. A typical modern pulsed laser can easily deliver $10^5 W$ in a $10^{-8} s$ pulse. At these laser powers no single transition can be considered in isolation. A complete picture of all possible excitation pathways in the molecule would have to include a variety of processes, i.e. Raman phenomena, harmonic generation, Rabi cycling, ionisation, photodissociation, radiationless transitions, saturation and polarisation effects. All of these processes should be included in the overall description of transitions in an intense radiation field. However, this can be done, if at all, only with difficulty [14].

Johnson and Otis [13] have shown that many of the important features of multiphoton ionisation can be described by kinetic rate equations. The rate equation model provides a convenient description of multiphoton ionisation in the following cases [15]:

1. The laser band-width is much larger than the natural line-width of the resonant multiphoton transition.
2. The coherence time of the laser is short relative to the Rabi cycling frequency of the resonant transition.
3. The Rabi cycling frequency is much slower than the rate of ionisation.

Further discussion of 2 and 3 is in order. A pulsed multi-mode dye laser of band-width $\Delta\nu_L \sim 1\ \mathrm{cm}^{-1}$ has a coherence time of $1/\Delta\nu_L, \sim 33$ ps, which is short compared to the pulse length. In any multiphoton excitation scheme the populations of each state are coupled at the Rabi frequency and driven coherently in time. The general expression for the Rabi frequency Ω is given by Parker [16] as:

$$\Omega = [(2dE/\hbar)^2 + (W_L - W_A)^2]^{\frac{1}{2}} \qquad 2.9$$

where d is the transition dipole matrix element

E is the laser field amplitude

W_L is the laser frequency (in Hz)

W_A is the molecular transition frequency (in Hz)

The most general treatment of MPI dynamics is provided by the equations of motion for the density matrix of the system [17]. If the coherence of the system and laser field is completely preserved then a full quantum mechanical approach is appropriate. Population rate equation analysis arises at the other extreme when coherence properties play an insignificant role in the dynamics. Most molecular MPI experiments to date have been performed with a pulsed multi-mode dye laser. The large band-widths ($\sim 1\mathrm{cm}^{-1}$) employed in these experiments imply a short phase coherence time and hence, a minimal influence of coherence effects on MPI dynamics.

Following the treatment of Zakheim and Johnson

[12], equations can be derived describing a [n+m] photon ionisation from the ground state X, through the resonant state A, to the ionisation continuum with a single resonance at the n-photon level. Figure 2.2 shows a schematic representation of the levels involved in a [2+1] REMPI process. The notation used is as follows:

I is the laser intensity (photons $cm^{-2}s^{-1}$).

$\alpha = \sigma_1 I^n$ and $\beta = \sigma_{II} I^m$. When n = 2 and m = 1 then σ_I and σ_{II} are two-photon ($cm^4 s$) and one-photon (cm^2) cross-sections, respectively.

γ is the radiative or fluorescence decay rate (s^{-1}).

δ is the radiationless transition rate (s^{-1}) to a species that does not ionise.

For square-pulse laser excitation of duration t it can be shown that the ion concentration C is given by:

$$C = \frac{\beta \chi_o}{(\beta+\delta)} \left[1 + \frac{L}{K-L} \exp(-Kt) - \frac{K}{K-L} \exp(-Lt) \right] \qquad 2.10$$

where χ_o is the ground state molecular concentration

$$K = \frac{Y}{2} + \frac{1}{2}(Y^2 - 4\alpha Z)^{\frac{1}{2}} \qquad 2.11$$

$$L = \frac{Y}{2} - \frac{1}{2}(Y^2 - 4\alpha Z)^{\frac{1}{2}} \qquad 2.12$$

$$Y = 2\alpha + \beta + \gamma + \delta \qquad 2.13$$

$$Z = \gamma + \beta \qquad 2.14$$

FIGURE 2.2 Schematic representation of the levels involved in a [2 + 1] REMPI process.

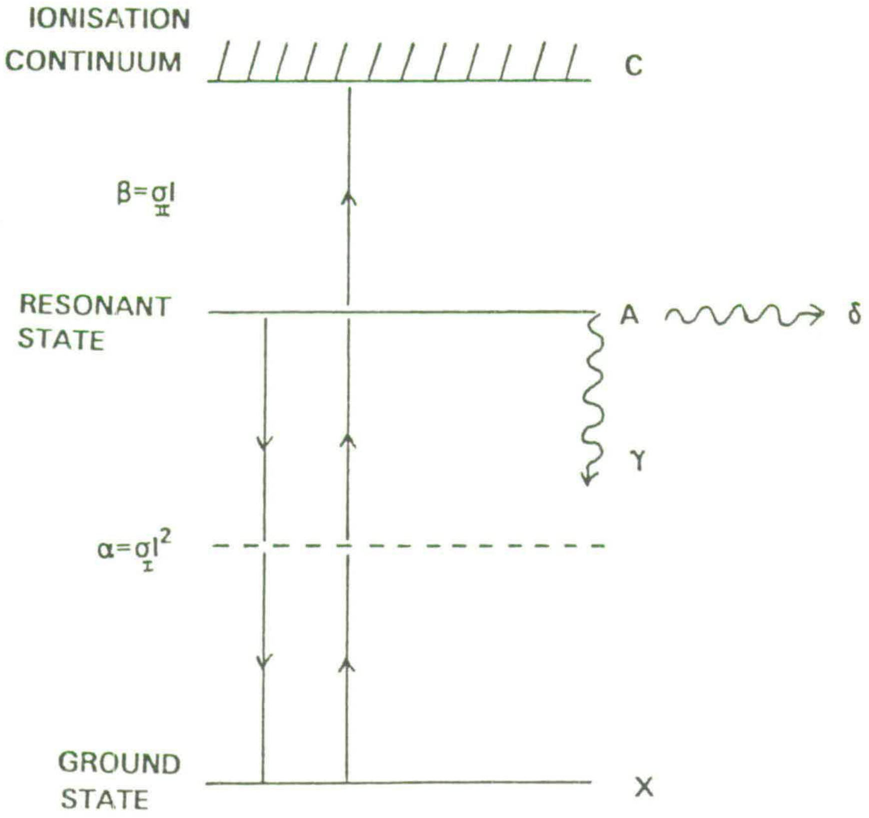

Certain limiting forms can be readily identified. At the limit of low laser intensities or small cross-sections the overall ionisation probability to the continuum is simply $\sigma_I \sigma_{II} I^{m+n}$. At moderate intensities under normal situations where $\beta >> \alpha$, the ionisation step will be kinetically 'saturated' and the overall probability should be proportional to $\sigma_I I^n$. The rate equation model will be discussed later in conjunction with power dependence measurements for the [2+1] MPI of HCl. One important point of note arises whenever the dissipative rate δ exceeds the ionisation rate β by a substantial amount. Should this be, then the radiationless transition will preferentially occur and the electronic state associated with it will not appear in the ionisation spectrum. From conventional high resolution absorption spectra many excited electronic states (usually valence states) can undergo some rapid energy evolution as evidenced by line-width measurements. This can, and does, prevent them from appearing in MPI spectra [27], as will be shown in this work for certain excited electronic states of HCl. The non-appearance of an excited electronic state in a MPI spectrum must however be treated with caution as there may be effects other than radiationless transitions depleting the excited state population. Recently, optical non-linear processes , for example, third harmonic generation have been found to effectively quench the [3+1] MPI signal from C_2H_2 at elevated pressures [18,19]. Similar effects have been noticed, by Johnson and co-workers [20], in the multiphoton excitation and dissociation of Cl_2. Indeed, third harmonic generation, enhanced by a two-photon resonance in CO, has been observed [21]. Generally however, a non-radiative loss process of an excited state manifests itself in a MPI spectrum by a reduction in the line intensity and by an increase in the spectral line-width i.e. lifetime broadening.

A variety of other line-broadening mechanisms can result under the very high laser intensities used in a typical MPI experiment. These effects can all be minimised by reducing the photon flux at the focus region, but this may adversely affect the total signal available.

Before discussing some of these line-broadening effects a brief diversion into some of the major factors contributing to spectral line profiles will be discussed. An excellent summary of these can be found in reference [22].

The emission of excitation energy from an excited molecular state can be described by a homogeneous, Lorentzian line profile with a particular natural line-width. The mean lifetime, τ, of a molecular level E which decays exponentially by spontaneous emission is related to the Einstein A coefficient by $\tau = \frac{1}{A}$. The half-width, $\delta\nu$, of a spectral line spontaneously emitted from the level E is given by:

$$\delta\nu = A/2\pi = \frac{1}{(2\pi\tau)}\ \text{Hz} \qquad 2.15$$

Generally the Lorentzian line profile, with natural line-width $\delta\nu$ as above, cannot be observed without special techniques because it is completely concealed by other broadening effects. One of the major contributions to the spectral line-width in gases at low pressures is the Doppler width, which is due to the thermal motion of the absorbing or emitting molecules. The Doppler line profile can be defined by a Gaussian line-shape function with a half-width, δ w, determined by:

$$\delta w = \frac{w_o}{c}\,(8kT\ell n2/m)^{\frac{1}{2}} \qquad 2.16$$

where w_o is the centre frequency (in Hz) of the molecular transition line. Here:

c is the speed of light

k is Boltzmann's constant

T is the temperature in Kelvin

m is the mass of the molecule.

More detailed consideration shows that a Doppler broadened spectral line cannot be represented by a pure Gaussian profile. The intensity profile is in fact a convolution of the Lorentzian lifetime profile and the Gaussian profile and is called a Voigt profile. Collisional broadening can also be an important line-broadening mechanism. Both elastic and inelastic collisions can contribute [22] and it is often called pressure broadening because of its marked pressure dependence.

When a radiation field (laser) interacts with molecules, if the interaction time of the molecules with the radiation field is small compared with the spontaneous lifetime, then time-of-flight broadening can result [22]. At the high laser intensities required to perform a MPI experiment other line broadenings can drastically affect the resolution of the MPI spectrum. The observed line-widths may be large due to lifetime broadening induced by the laser. It is usually the case that the ionisation step is more probable than the multiphoton step to the resonant state. When reasonable signal levels are obtained the excited state lifetime is considerably shortened and thus line-widths are broadened. The greater the difference between the order of the critical resonant transition versus that of the ionisation step, the more likely there is to be lifetime broadening. One common loss of resolution comes from the conical geometry of the focussed light beam and the high order of non-linearity of the ionisation. Near the focus region a more-or-less cylindrical geometry can be assumed. Outside this, the conical geometry creates a rapid intensity decrease as one moves away from the focus. Saturation of the ionisation is frequently attained in the focal region. Increasing the laser intensity generates no more ion signal, but the ionisation region begins to move out into the conical focus regions. It can be shown that power dependence scales as $I^{\frac{3}{2}}$ (where I is the laser intensity) no matter how many photons are involved in the ionisation process [12,13,23]. When the on-resonance signal is saturated, the off-resonance signal (usually a continuum background) still has a high order of non-linearity and the background signal will increase until it too is saturated. This type of phenomena caused, by incorrect focussing parameters, is commonly called geometric saturation. It can easily be alleviated by reducing the laser intensity or using a lens system which produces a larger focal radius.

Another major perturbation in multiphoton ionisation spectra stems from the quadratic a.c. Stark effect, so called because the energy level shift (Stark shift) depends quadratically on the field strength. At the simplest level this effect tends to broaden and shift the spectral lines. In order to use high power lasers in quantitative studies, it is necessary to take the a.c. Stark effect into account, including the temporal and spatial characteristics of the laser used in the analysis. Johnson et al [24] have derived methods for determining the line-shape of a molecular transition in the presence of a large a.c. field associated with the laser light. They showed that the remarkable change from a sharp line (laser-limited line-width) at low intensities to broad asymmetric lines (which depend very sensitively on the focussing conditions) can be understood and reproduced by considering the quadratic a.c. Stark effect combined with the spatial and temporal variation of the laser intensity.

Qualitatively, consider two molecules, one at point A and the other at point B in the focussed laser beam with the laser intensity (I_A) at point A greater than that (I_B) at point B, $I_A > I_B$. It follows, therefore because the quadratic a.c. Stark shift of the resonance frequency ν_r of the molecular transition is proportional to the radiation intensity [24] that the line shift for the molecule at A is greater than that for the molecule at B. These two molecules will have different resonance frequencies for the same electronic transition. The spectral intensity difference at E_A and E_B arises because there are more molecules in the low intensity contour containing point B than in the contour containing point A. The broad line-shape then is a function of the continuous distribution of molecules over the intensity contours of the focussed beam. In the most common case the laser beam is conically focussed, the spectral line is simply broadened in the direction of the quadratic a.c. Stark shift of the electronic transition. The intensity variation throughout the focussed beam causes a large variation in the shift of the levels for molecules in various positions of the focal region. There are many more molecules in the low intensity regions than at the focal centre, so obviously the highest signal is seen near the unshifted transition energy, with the minority of molecules contributing to the tail. Here then the spatial inhomogeneity dominates the time dependence of the intensity.

The other operational extreme is with a high intensity unfocussed laser beam. In this case the spatial inhomogeneity is not so large, so the time evolution of the intensity is more important. In any non-linear process the signal will be greatest at highest intensity, therefore most of the ions will be produced at the peak of the pulse, which coincides with the maximum Stark shift. The peak of the spectral line will therefore be near the maximum shift position and tail towards zero at the molecular transition energy. Figure 2.3 shows schematically the type of line-shape expected due to a.c. Stark broadening.

Johnson et al [24-26] have shown that the quadratic a.c. Stark effect is the major cause of asymmetric broadening in the low pressure MPI spectrum of NO. They also noticed that the broadening is quenched with increasing pressure of NO. An explanation of this effect has been offered quantitatively in terms of a collective a.c. Stark effect, which depends in a complicated way on the pressure, laser band-width and intensity [26]. In low pressure gases the a.c. Stark shift of a molecule, absorbing and emitting a photon simultaneously or emitting and re-absorbing the identical photon should be independent of the states of other molecules. However, this neglects the fact that all molecules are interacting

FIGURE 2.3 Typical effects of laser intensity and focussing on the line-shape of a single rotational transition induced by the a.c. Stark effect.

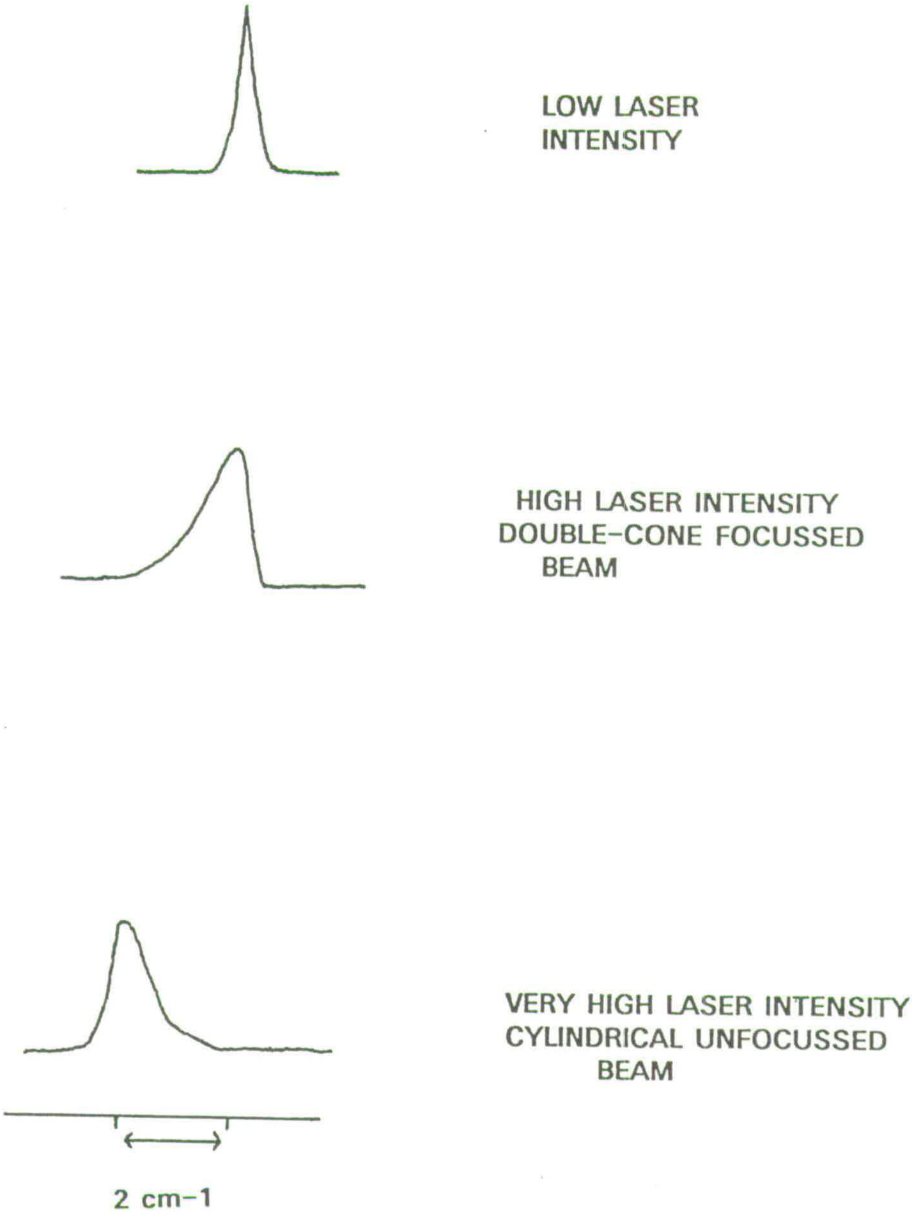

with, and 'see' each other through the common laser field. Thus it is the ensemble of such molecules that must be taken as the system interacting with the photons, even when the pressure is so low that direct mutual interaction of molecules may be ignored. A full description of this dramatic pressure narrowing of a.c. Stark-broadened lines in MPI spectra can be quantitatively explained as a collective and quantum interference effect [26].

One final point of note is the care that must be taken in the interpretation of ionisation power dependence i.e. the number of photons needed to cause ionisation of a ground state molecule, when a.c. Stark broadening is suspected. For example, much higher orders than expected have been observed on a.c. Stark-broadened MPI transitions in NO [25] and this could be quite misleading in determining the total number of photons required to reach the ionisation continuum.

In conclusion, some of the contributory factors for the transition profiles and line-widths observed in MPI spectra can be usefully summarised as in Figure 2.4. For all of the multiphoton ionisation experiments performed in this work particular care was taken to avoid line-broadening effects due to excessive laser intensity. Generally, the problem can be alleviated simply by reducing the laser pulse energy or changing the focussing lens to one of longer focal length hence reducing the photon intensity at the focal region.

FIGURE 2.4 Factors contributing to transition profile and line-width in MPI spectroscopy.

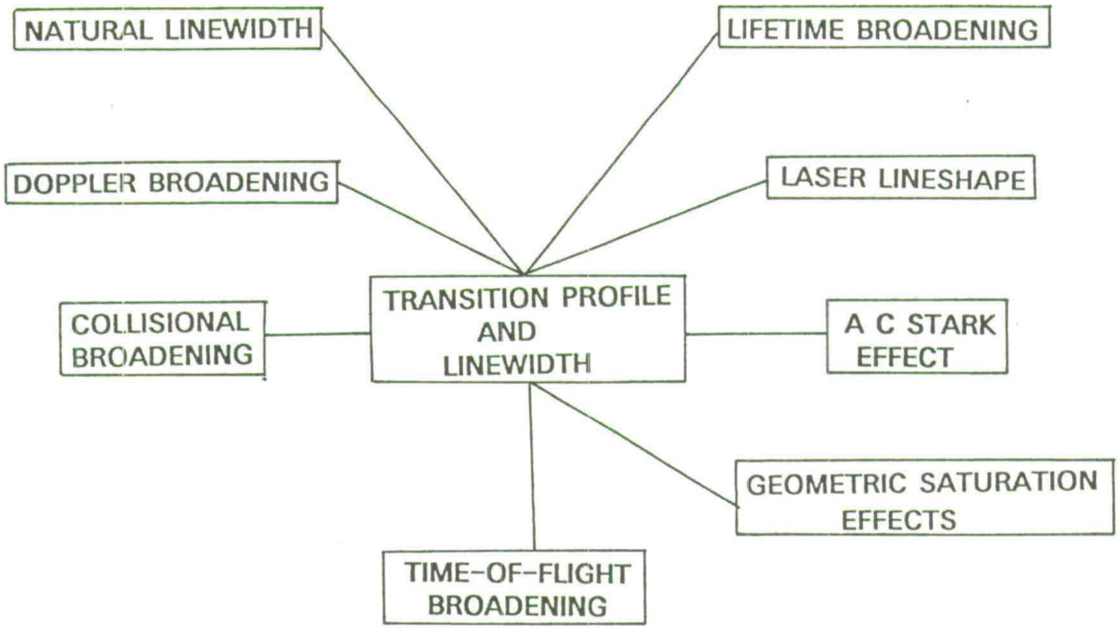

2.4 REFERENCES

1. S.V. Filseth, R. Wallenstein and H. Zacharias, Opt. Commun., 23, 231 (1977).
2. E. Riedle, H. Stepp and H.J. Neusser, Chem. Phys. Lett., 110, 452 (1984).
3. M.N.R. Ashfold, R.N. Dixon, K.N. Rosser, R.J. Stickland and C.M. Western, Chem. Phys., 101, 467 (1986).
4. W.M. McClain and R.A. Harris, p.1, Chapter 1 in 'Excited States', Volume 3, edited by E.C. Lim (Academic Press, 1977).
5. R.G. Bray and R.M. Hochstasser, Mol. Phys., 31, 1199 (1976).
6. J.B. Halpern, H. Zacharias and R. Wallenstein, J. Mol. Spectrosc., 79, 1 (1980).
7. C. Maïnos, Y. Le Duff and E. Boursey, Mol. Phys., 56, 1165 (1985).
8. C. Maïnos and Y. Le Duff, Mol. Phys., 60, 383 (1987).
9. A.C. Kummel, G.O. Sitz and R.N. Zare, J. Chem. Phys., 85, 6874 (1986).
10. G. Herzberg in 'Molecular Spectra and Molecular Structure, Vol. I - spectra of Diatomic Molecules', 2nd Edition (D. Van Nostrand Company, Princeton, 1950).
11. P.W. Atkins in 'Molecular Quantum Mechanics', p.319, 2nd Edition (Oxford University Press, 1983).

12. D.S. Zakheim and P.M. Johnson, Chem. Phys., 46, 263 (1980).

13. P.M. Johnson and C.E. Otis, Ann. Rev. Phys. Chem., 32, 139, (1981).

14. P. Lambropoulos, Adv. At. Mol. Phys., 12, 87 (1976).

15. D.C. Jacobs and R.N. Zare, J. Chem. Phys., 85, 5457 (1986).

16. D.H. Parker, p.233, Chapter 4 in 'Ultrasensitive Laser Spectroscopy', edited by D.S. Kliger (Academic Press, 1983).

17. P. Agostini, A.T. Georges, S.E. Wheatley, P. Lambropoulos and M.D. Levenson, J. Phys. B. Atom. Mol. Phys., 11, 1733 (1978).

18. T.M. Orlando, L. Li, S.L. Anderson and M.G. White, Chem. Phys. Lett., 129, 31 (1986).

19. M.N.R. Ashfold, C.D. Heyret, J.D. Prince and B. Tutcher, Chem. Phys. Lett., 131, 291 (1986).

20. L. Li, M. Wu and P.M. Johnson, J. Chem. Phys., 86, 1131 (1987).

21. C.T. Rettner, E.E. Marinero, R.N. Zare and A.H. Kung, J. Phys. Chem., 88, 4459 (1984).

22. W. Demtröder in 'Laser Spectroscopy - Basic Concepts and Instrumentation', (Springer-Verlag, 1982).

23. M.R. Cervenan and N.R. Isenor, Opt. Commun., 13, 175 (1975).

24. L. Li, B-X. Yang and P.M. Johnson, J. Opt. Soc. Am. B., 2, 748 (1985).

25. C.E. Otis and P.M. Johnson, Chem. Phys. Lett., 83,

73 (1981).

26. L. Li, R.N. Porter and P.M. Johnson, Phys. Rev. Lett., 53, 1336 (1984).

27. M.N.R. Ashfold, J.M Bayley and R.N. Dixon, Can. J. Phys., 62, 1806 (1984).

CHAPTER 3

EXPERIMENTAL DETAILS

3.1 INTRODUCTION

The study of the spectroscopy and photochemistry of excited electronic states of molecules has been limited until very recently to well tried experimental techniques. In particular, high resolution absorption and discharge-excited emission have provided a plethora of spectroscopic information on diatomic molecules [1]. With the development of high power, fixed frequency and tunable laser technology a new tool has become available for studying electronically excited states of diatomic molecules.

The following pages provide a brief discussion of the experimental systems and techniques used in the course of this work.

3.2 LASERS

Central to all the work performed has been the use of a laser. Three systems will be described in detail. One system based on an argon fluoride (ArF, 193nm) excimer laser [2,3] for the VUV multiphoton dissociation of C_2H_3Cl experiments, as described in Chapter 7. The other two laser systems were used to directly excite electronic states in HCl by producing intense, tunable UV radiation in the 220-260nm region. One system for this technique was based on a xenon chloride (XeCl) excimer

[2,3] pumped-dye laser [2,4], the second was a Neodymium Nd^{3+}, Yttrium Aluminium Garnet (Nd:YAG) [2,5] pumped-dye laser system. Both were distinctly different, as will be described below.

3.2.1 EXCIMER PUMPED-DYE LASER SYSTEM

A Lambda Physik EMG 201 MSC excimer laser [2,3] operating on the XeCl exciplex emission line at 308nm was used to pump a tunable dye laser, either a Lambda Physik FL2002 or FL3002 system. The excimer laser was capable of generating a maximum of 400mJ per pulse with a typical pulse width of 15ns at a 2Hz repetition rate. (All laser pulse energies above ~1mJ were measured by either a Gen-Tec ED200 Joulemeter or various Photon Control 'average power' meters.) At a normal running rate of 5-10 Hz a pulse energy from the excimer of 300mJ was easily obtainable.

In the FL2002 or FL3002 dye laser 5% of this pump beam was used to transversely pump a cuvette containing recirculating dye solution positioned in a Hänsch-type oscillator cavity having a prism beam expander [2,6]. Wavelength selection was provided by a grating (600 lines/mm) which could be tilted between the Littrow angles of 42.5° and 72.5°. The vertically polarised multi-mode oscillator output had a band-width of ~ 0.18 cm^{-1} as measured with a fused silica Fabry-Perot monitor etalon [2]. (Lambda Physik FL82, free spectral range 0.67 cm^{-1}, finesse ~16). The dye flow cuvette of the oscillator also served as the dye cuvette for the pre-amplifier. Again $\sim$5% of the 308nm pump beam was used for pre-amplification of the oscillator output. Further amplification was provided in a final dye cuvette with its own recirculating dye solution pumped transversely with the remainder of the 308nm pump beam. A polariser (Lambda Physik FL50) could be inserted prior to the amplifier stage to improve the vertical polarisation characteristics of the radiation.

For this work the solutions of Lambda Physik dyes, as listed below (together with their lasing wavelength ranges), were used.

(i)	Coumarin 307	(Lambdachrome 5000)	479-553nm
(ii)	Coumarin 102	(Lambdachrome 4800)	460-510nm
(iii)	Coumarin 47	(Lambdachrome 4700)	440-484nm
(iv)	Coumarin 2	(Lambdachrome 4500)	432-475nm

Energy conversions of 10-15% could be achieved towards the middle of these wavelength ranges and thus typical dye laser pulse energies of 35-40mJ were obtainable.

The required radiation in the 220-260nm range was generated by passing 440-520nm dye laser fundamental through a potassium pentaborate (KPB) second harmonic generating (SHG) crystal [2], which was mounted after the final amplifier stage in the dye laser. The details of the three Lambda Physik KPB crystals used, along with the wavelengths of laser light produced, are listed below. In addition, the angle of cut of the individual crystals with respect to their optical axis are as shown [2].

(i)	KPB crystal FL 32	230-275nm	56.2°
(ii)	KPB crystal FL 33	220-233nm	69.98°
(iii)	KPB crystal FL 34	217-222nm	82.87°

For the above fundamental energies, these crystals had a conversion efficiency of $\sim$1% i.e. 300-400 μJ of UV output pulse energy could be produced. (Recently, a new material beta barium borate (BBO) has become available which has considerably better SHG efficiency than the KPB crystals required to cover the wavelength ranges above.)

The KPB crystals were mounted on a motorised crystal tilter (Lambda Physik FL532B) which allowed angle tuning of the crystal so as to maintain the phase matching conditions necessary for second harmonic generation [2]. The tilt axis of the crystal must be perpendicular to the polarisation of the fundamental laser light. A quartz compensator crystal could also be mounted on the tilter after the SHG crystal for automatic beam displacement correction.

The UV light was separated from the fundamental using either a single Pellin-Broca quartz prism or the Lambda Physik FL35 frequency separation device. This consisted of four quartz Pellin-Broca prisms set to nearly Brewster's angle so reflection losses were reduced. A diaphragm stopped the fundamental beam after the second prism. The UV output was in the optical axis of the dye laser.

To scan the UV laser wavelength the crystal must be tilted or 'angle-tuned' as the fundamental was changed by moving the grating. In the FL2002 dye laser this was achieved using a dedicated microcomputer (Lambda Physik FL582, TRS80 Radio Shack) system to control the grating and the crystal tilter stepper motors. Movement of the crystal and the grating on the FL3002 dye laser was also achieved using an integrated microprocessor based system. To ensure proper 'tracking' of the crystal with the grating movement, the UV pulse energy can be conveniently monitored using a photodiode (EG & G UV-215 BQ), with care being taken not to saturate the response.

3.2.2 Nd:YAG PUMPED-DYE LASER SYSTEM

The Nd:YAG pumped-dye laser system was the Quantel Datachrom-5000. A YG 581-20 Nd:YAG 'Q'-switched [5] pump laser was capable of delivering upwards of 280mJ per pulse of 532nm radiation at a repetition rate of 20 Hz. The 532nm radiation was produced by frequency doubling the 1064nm Nd:YAG fundamental in a potassium dihydrogen phosphate (KDP) crystal. The two wavelengths were separated using dichroic mirrors [2]. The 532nm laser light pumped a TDL-50 dye laser. In the dye laser about 5% of the pump beam was used to transversely pump a cuvette containing recirculating dye solution positioned in a Moya-type oscillator cavity. This design differs from the Hänsch-type, Littrow-incidence grating and uses the grazing-incidence method for wavelength selection [2,7]. Tuning was accomplished by mirror rotation using a d.c. motor rather than a stepper motor system. This technique potentially can give a narrower line-width for the dye laser fundamental without having to resort to angle or pressure tuning of an intracavity etalon [7]. By recording iodine I_2, B-X fluorescence excitation spectra and comparing these with the known B-X absorption spectrum [8] the band-width was estimated to be ~ $0.08cm^{-1}$. The output from the oscillator was amplified in a transversely-pumped amplifier cuvette using the same recirculating dye solution as that in the oscillator. Further amplification was provided with the remainder of the 532nm pump beam in a second amplifier dye cell with its own recirculating dye solution. This dye cell was a transversely-pumped broad bore capillary. The dye laser light produced from this dye cell had a relatively homogeneous spatial intensity distribution free from local 'hot' spots. This was important at subsequent stages of frequency doubling and mixing where good spatial beam quality and 'fade' across the monitor bi-photodiodes was essential for good crystal 'tracking'.

For this work the solutions of Exciton laser dyes as listed below (together with their lasing wavelength ranges), were used.

(i)	DCM	594-630nm
(ii)	Kiton Red	578-606nm
(iii)	Rhodamine 610	567-599nm
(iv)	Rhodamine 590	552-580nm.

At the middle of the tuning range about 15-20%

energy conversion was possible and thus typical dye laser pulse energies were ~45-55mJ.

The required radiation in the 220-260nm region was produced using frequency mixing after frequency doubling [2], as described below.

The dye laser fundamental (typically 560-640nm) was frequency doubled by second harmonic generation in a KDP crystal. This produced UV radiation in the region 280-320nm with typical pulse energies of 10-12mJ. This UV laser light was then sum-frequency mixed in a KDP mixing crystal with residual (~100mJ pulse energy) 1064 nm fundamental radiation from the Nd:YAG laser [2]. The resulting UV radiation in the 222-245nm wavelength range had a band-width ~1-1.5cm^{-1} and a pulse energy of ~0.8-1 mJ. The band-width was obviously dominated by that of the 1064nm radiation, (~0.7cm^{-1}). This UV laser radiation again was separated from that frequency doubled and the dye laser fundamental with a Pellin-Broca prism. Spatial filtering with an iris ensured only the required radiation reached the experiment. Any residual 1064nm Nd:YAG fundamental radiation was dumped safely in a beam stop in the dye laser. Quartz compensators after each KDP crystal allowed for correction of any beam displacement.

'Auto-tracked' angle-tuning of the KDP crystals and quartz compensators was accomplished using a bi-photodiode based servo-tracking system with modules which separately monitored the frequency-doubled and mixed-UV radiation. The successful operation of these depended on critical alignment of the requisite beams and rejection of any unwanted laser radiation falling on the bi-photodiodes. After the frequency-doubling crystal a small portion of the laser radiation was directed, via a filter housing, onto a bi-photodiode. A Schott UG5 colour glass filter removed the fundamental dye laser light and several Melles Griot neutral density filters attenuated the residual UV light so as to avoid saturating the bi-photodiode. At the frequency mixing stage a Schott UG 1 colour glass filter removed the dye laser fundamental and one of two Oriel narrow band-pass interference filters [2] isolated the required UV radiation. One filter had a nominal peak transmission wavelength of 240nm, the other was centred at 220nm. Both had a bandpass of ~25nm. Neutral density filters were also used when required. With careful alignment an 'auto-tracking' range of up to 4nm in the 225-245nm wavelength region could be accomplished. Figure 3.1 illustrates schematically the layout of the Quantel Datachrom-5000 laser.

3.2.3 ArF EXCIMER LASER SYSTEM

The work described in Chapter 7 on the multiphoton dissociation of C_2H_3Cl and C_2H_3Br was performed using a Lambda Physik EMG 500 argon fluoride (ArF) excimer laser [2,3]. The latter produced broadband VUV radiation centred at 193.3nm with the wings of the emission

FIGURE 3.1 Schematic representation of the Quantel Datachrom-5000 laser used to produce tunable UV radiation by frequency doubling and mixing techniques.

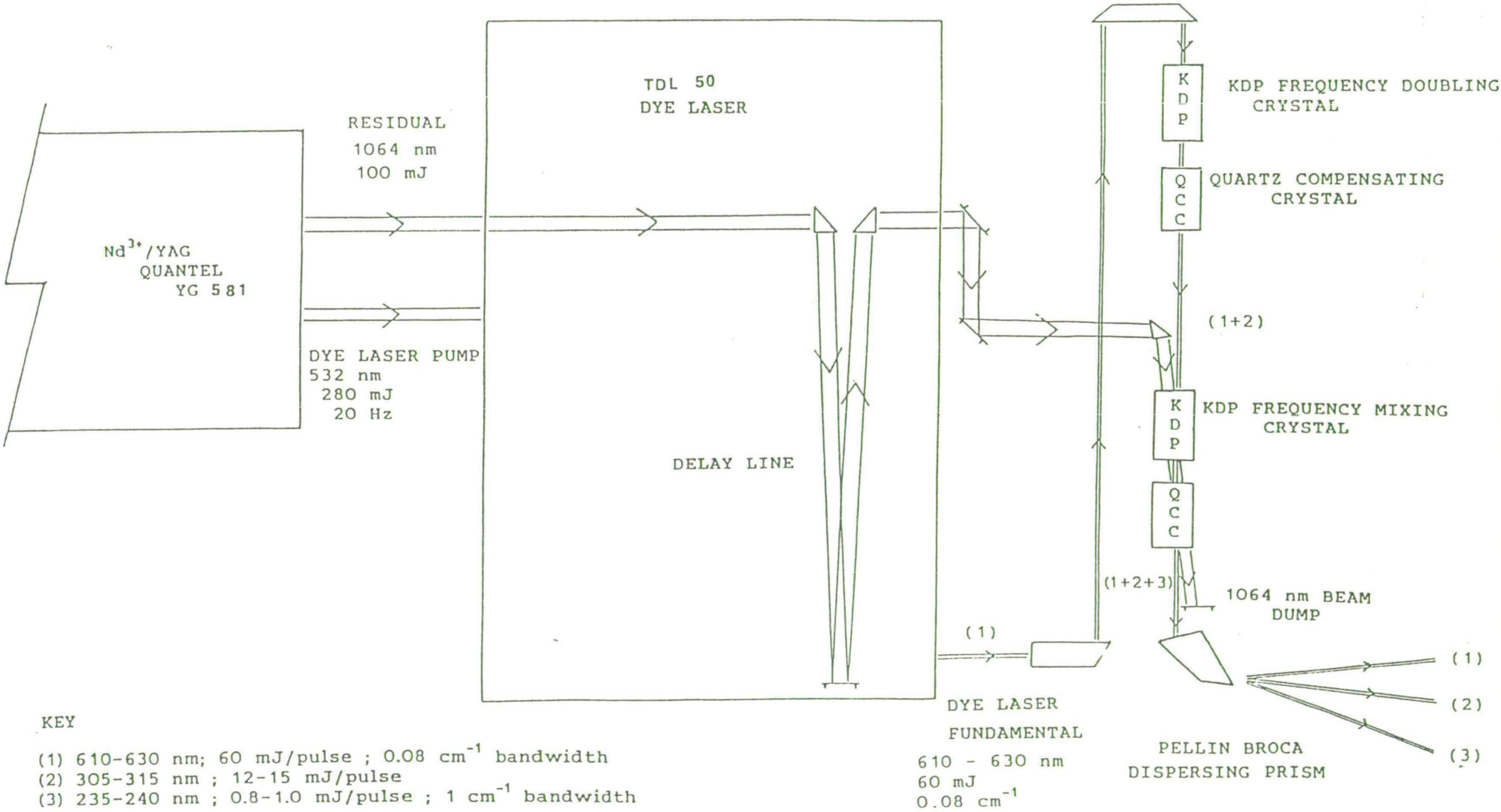

profile extending significantly to ~192.6nm and ~193.8nm. At a 2Hz repetition rate 60mJ (maximum energy) was delivered during a pulse width of ~15ns. The unfocussed output beam profile dimensions were ~2.5cm x 1cm.

3.3 RESONANCE ENHANCED MULTIPHOTON IONISATION (REMPI) SPECTROSCOPY

The REMPI experiments described in this work were performed in both a low pressure static gas cell and in a supersonic free jet expansion.

3.3.1 MULTIPHOTON IONISATION CELL

The cell used was 20cm in length, made of Pyrex glass, with 5cm diameter Comar Optics Spectrosil B windows at either end of the body of the cell, mounted at the Brewster's angle with 'Halocarbon' wax. Wood's horns were also included to help trap laser light scattered from the windows. At the centre of the cell were two 2.5cm diameter ports, again equipped with Spectrosil B windows, for viewing fluorescence. Through holes in the cell body, perpendicular to these ports, two nickel (Ni) ion collection plates, with spot-welded Ni wire feedthroughs, were positioned 1cm apart. The feedthroughs, and hence the collection plates, were held in place by sealing the holes in the glass with Varian 'Torr-Seal' high vacuum epoxy resin. Typically, 200-800 mTorr (26.66-106.66Nm^{-2}) of HCl was placed in the cell. The pressure was measured by a 0-10 Torr (0-1.33kNm^{-2})

capacitance manometer (MKS Baratron Model 122 AA). Using the above design the 'background' non-resonant ionisation signal was negligible. It was also possible to perform ionisation detection and fluorescence detection of electronically excited HCl in the same cell simultaneously.

The tunable UV laser light was focussed between the Ni plates with a 15cm focal length, plano-convex, fused silica lens. The focal spot was estimated to be 180μ in diameter by the 'knife-edge' method. This entailed mounting a razor blade on a micrometer screw gauge and translating the edge across the focal spot while monitoring the energy.

3.3.2 SUPERSONIC FREE JET APPARATUS

The supersonic free jet expansion was generated by a modified, pulsed Bosch fuel injector nozzle (Volvo 144), similar to the design of Behlen and Rice [9]. The tip of the plunger extending beyond the orifice was removed and the body of the injector machined so that it could be disassembled for cleaning. A variable-duration, variable-voltage square-wave pulse from a home-built control unit was used to control the solenoid in the nozzle. A Farnell PG 102 dual-channel pulse generator controlled the timing to allow synchronous firing of the nozzle with respect to the laser light pulses. Typically the nozzle was triggered ~ 1ms before the laser so as to allow for the solenoid response time. The pulsed nozzle was mounted directly on top of a black-anodised aluminium chamber and pointed directly into the throat of an Edwards E04 4" oil diffusion pump, backed by an Edwards ED200 two stage rotary pump. On top of the diffusion pump a liquid nitrogen cold trap and a quarter-swing 'butterfly' valve were mounted to allow isolation of the chamber from the pumps. The aluminium chamber had four flanges. Two were used to mount 5cm diameter Spectrosil B windows. From the third, the Ni ion collection plates and vacuum feedthroughs were mounted. The fourth was used to mount either an Edwards PRL 10 Pirani gauge or a 0-10 Torr (0-1.33kNm^{-2}) capacitance manometer (MKS Baratron Model 220-AHS). The base pressure of the chamber was better than 10^{-6} Torr (1.33x10^{-4}Nm^{-2}). While the nozzle was operated the solenoid voltage pulse was varied so that the ambient chamber pressure was 10^{-3} Torr (0.133Nm^{-2}) at a repetition rate of 5-10Hz with a backing pressure of ~1-2 atm (1.013x10^{5}-2.026x10^{5}Nm^{-2}) of various concentrations of HCl in argon (Ar).

The fuel injector, as supplied, has a 1000μ diameter orifice. For the experiments performed this was reduced to 500μ by attaching a pinhole (Ealing Electro-Optics) over the original.

The laser light was focussed on the free jet expansion, with the same lens as described previously, about 5-10mm downstream of the orifice. The Ni ion collection plates mounted 20mm below the interrogation region collected any ionic species generated. In both the static cell and the supersonic jet experiments the Ni plates were biased at 90V d.c. Any ion current produced was collected by a home-built differential input operational amplifier with a variable gain of 10^3-10^7 volts amp^{-1} [10] and then sent to the signal processing equipment.

3.4 FLUORESCENCE AND TIME-RESOLVED SPECTROSCOPY

3.4.1 FLUORESCENCE SPECTROSCOPY

In these experiments fluorescence from electronically excited HCl^* was studied following direct two-photon excitation, as discussed in Chapters 5 and 6, or by photochemical production following multiphoton dissociation of C_2H_3Cl, as described in Chapter 7. The aim of each experiment is however the same, to discriminate any HCl^* emission from scattered laser light and to obtain dispersed fluorescence spectra. In the direct, two-photon excitation experiments a conventional spectrometer and photomultiplier tube combination was used. In the multiphoton dissociation work the photon detector was an Optical Multi-channel Analyser (OMA) [2]. The OMA, though less sensitive than a photomultiplier tube, allowed rapid spectral accumulation over a wide wavelength range. As in any experiment involving transmission of light through a spectrometer the maximum photon throughput by 'étendue' matching is important [11]. Thus, to optimise the experiment, the emission under study must be imaged at the entrance slit so as to fill the slit and grating with light. This generally requires at least a two lens combination:- A high aperture (low f-number) 'condenser' lens to project an image onto the entrance slit of the spectrometer and a second 'field lens' close to the entrance slit to image the 'condenser' lens onto the spectrometer's collimator (mirror).

The fluorescence cell design for two-photon excitation of HCl was as described previously. Typical pressures used were 3-5 Torr (399.97-666.61Nm^{-2}) HCl. Fluorescence was imaged with a f/1.5, 4cm focal length, plano-convex, fused silica lens onto the entrance slit of a spectrometer. The inclusion of a second imaging lens of appropriate focal length just in front of the entrance slit proved not to be critical.

To study HCl* emission between 200 and 500nm either a Jobin-Yvon HRS 2, f/7, 0.6m spectrometer or a McKee Pederson MP 1018B, f/9, 0.5m spectrometer was used in conjunction with a photomultiplier tube. Both spectrometers were in the Czerny-Turner configuration [2] and contained 1200 lines/mm gratings blazed for 300nm. A Hamamatsu R928 'side-on' photomultiplier tube could adequately cover the wavelength region 200-500nm, however a Hamamatsu R166 'side-on' solar-blind photomultiplier tube gave better response between 200-300nm. Emission down to 170nm was studied using a low resolution 0.2m Acton Research Corporation (Model VM-502) VUV monochromator (with a concave 1200 lines/mm, holographically-lined grating [12]) in conjunction with the preferred R166 photomultiplier tube. The fluorescence cell in this case was mounted on an evacuable aluminium tube which held an imaging lens as described previously. To work below the quartz cut-off (160nm) would necessitate the use of MgF_2 or LiF optics. The whole system was pumped by a Pfeiffer Turbo-molecular TSH 050 pumping unit to better than 10^{-4} Torr ($1.33 \times 10^{-2} Nm^{-2}$), as measured with an Edwards CR25-K Penning gauge. A home-built pulse generator and stepper motor controller was used to move the grating. With any of the above spectrometers fluorescence excitation spectra were recorded by observing the emission at the appropriate wavelength and using the spectrometer to reject scattered laser light.

The experimental set-up for the multiphoton dissociation work was somewhat different. The ArF laser radiation was focussed, either with a 25 or with a 50cm focal length fused silica lens, into a fluorescence cell. The photo-fragment emission was viewed and imaged as before onto the entrance slit of a spectrometer. One spectrometer used was an f/10, 1m, Czerny-Turner configuration, Hilger and Watts Monospek 1000 fitted with a Jobin-Yvon holographically-lined 1200 lines/mm grating. The second was a Jarell-Ash f/3.8, 0.275m, crossed Czerny-Turner Monospec 27 spectrometer fitted with three holographically-lined gratings mounted on a rotatable turret. The gratings had 600, 300 and 150 lines/mm with a quoted blaze angle for 400, 500, and 450nm, respectively. The exit slit assembly of both spectrometers was removed and replaced by a flange from which an EG & G Princeton Applied Research Corporation Optical Multi-channel Analyser (OMA III) detector head could be attached. This was an EG & G M1420B intensified photodiode array [2], with the response optimised for UV light. The middle 700 of the 1024 photodiode channels were intensified and the detector head could be cooled (to reduce 'thermal' noise) by the 'Peltier effect' [13]. To prevent water vapour condensation, and possible damage, the head was continuously purged with dry 'white spot' nitrogen. The detector head was under the control of a M1460 system processor and its associated very powerful software package for data acquisition and subsequent manipulation. The synchronous operation of the laser and the OMA was controlled by a pulse generator. The OMA detector head used gave fast spectral acquisition over an extended wavelength range. The grating dispersion in the Monospek 1000 allowed ∼20nm to be observed simultaneously. In the Monospec 27 the three gratings gave a wavelength coverage of ∼150, 300 and 600nm, respectively. Wavelength calibration and resolution of all the spectrometers were determined using known emission lines from a mercury (Hg) lamp [14].

3.4.2 TIME-RESOLVED EMISSION SPECTROSCOPY

Time-resolved emission was studied usually with a small, high throughput, Hilger and Watts D292 monochromator and an EMI 9661B 'side-on' photomultiplier tube. The output from the photomultiplier could be viewed on a fast oscilloscope (Tektronix 2445A with a time resolution down to 1ns) or a Gould Biomation 8100 (8-bit resolution, 100MHz maximum sampling rate) transient recorder whose 50Ω input impedance was matched at the photomultiplier. An Apple II microcomputer was interfaced to the transient recorder and to the laser allowing initiation of the experiment and data acquisition, as has been described previously [15].

3.5 WAVELENGTH CALIBRATION

Laser wavelength calibration using the tunable systems was accomplished by deflecting ~4% of the dye-laser fundamental into an Iron hollow-cathode neon discharge lamp powered by a ~500V, 4mA supply (Cathodeon C610). The opto-galvanic effect [16,17] caused by changes in the discharge current when the laser is resonant with an atomic transition of the inert gas, neon, in the lamp produced a series of accurately known air-wavelength markers [18]. Between these reference points regularly energy-spaced transmission fringes from a solid quartz etalon [2] (Technical Optics, finesse ~7) were used for wavelength calibration. The free spectral range of the etalon was slightly wavelength dependent, as expected, being 3.372 cm^{-1} at ~600nm and 3.336cm^{-1} at ~ 480nm. The transmission fringes were detected using a photodiode.

3.6 SIGNAL PROCESSING

The signal processing in the time resolved emission or multiphoton dissociation experiments was under computer control, as has already been briefly described. The pulsed nature of the experiments with the tunable lasers meant that the transient signals produced had to be converted to a continuous signal if their laser or spectrometer wavelength dependence was to be displayed. This was done by a 'sample and hold' gated integrator or 'boxcar' device [2], with Stanford Research Systems SR250 gated integrators used throughout this work. The averaged output from one of the latter was sent, as necessary, either to a chart recorder, or via a Stanford Research Systems SR245 computer interface module, to an IBM PC-XT microcomputer. The data was stored on floppy disc and could be subsequently transferred to a 'mainframe' computer, if required. The high resolution studies in Chapter 4 required simultaneous detection and display of the REMPI signal and wavelength calibration. This was generally done using a two-pen chart recorder because of the duration of continuous scan required (up to 4 hours, on occasions). Power normalisation of signals was performed using the IBM PC-XT computer. The REMPI signal had an observed two-photon dependence on the laser intensity (see Chapter 4). Thus, by recording the ionisation signal (I) and simultaneously monitoring the UV laser light intensity (F), by a photodiode, a corrected signal $S = I/F^2$ could be calculated and displayed. Figure 3.2 shows schematically a typical experimental layout used to study the REMPI or the fluorescence spectroscopy of electronically excited HCl.

3.7 GAS HANDLING

All gas handling was performed on conventional Pyrex glass vacuum lines fitted with Young's P.T.F.E. taps. The vacuum was maintained by a mercury diffusion pump backed by a rotary pump, with a base pressure of 10^{-3} Torr ($0.133 Nm^{-2}$). All gases, where suitable, were purified by a freeze-pump-thaw cycle prior to use. (See Appendix II for sources and purities of the gases used.) Pressures for all the work were measured by three MKS Baratron capacitance manometers listed below.

MKS Baratron Model	Pressure range
122AA	0-10 Torr ($0-1.33 kNm^{-2}$)
222BA	0-100 Torr ($0-13.33 kNm^{-2}$)
221AHS	0-1000 Torr ($0-133.3 kNm^{-2}$)

Where mixtures of gases were required they were pre-mixed and left to stand for a time before being used.

FIGURE 3.2 A typical experimental layout used to study the REMPI or the fluorescence spectroscopy of HCl.

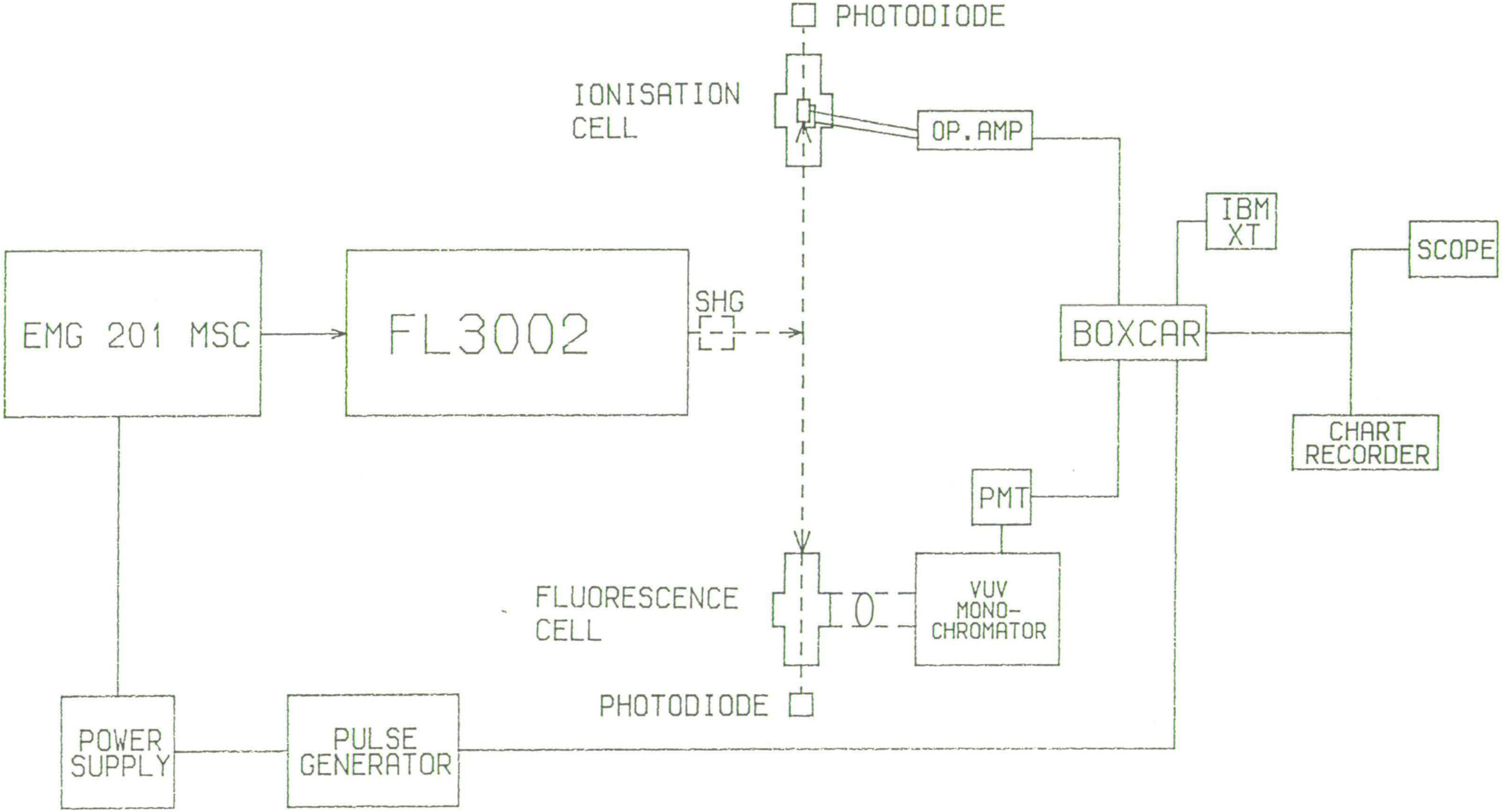

3.8 REFERENCES

1. K.P. Huber and G. Herzberg in 'Molecular Spectra and Molecular Structure IV. Constants of Diatomic Molecules', (Van Nostrand-Reinhold, New York, 1978).
2. W. Demtröder in 'Laser Spectroscopy - Basic Concepts and Instrumentation', 2nd Edition (Springer-Verlag, 1982).
3. C.H. Brau, Chapter 4, p.87 in 'Excimer Lasers' edited by C.K. Rhodes, Topics in Applied Physics, Volume 30, (Springer-Verlag, New York, 1979).
4. F.P. Schäfer, p.271 in 'Lasers: Physics, Systems and Techniques' edited by W.J. Firth and R.G. Harrison. (Proceedings of the 23rd Scottish Universities Summer School in Physics - NATO Advanced Study Institute, 1982).
5. M.C. Richardson, p.1 in 'Lasers: Physics, Systems and Techniques' edited by W.J. Firth and R.G. Harrison. (Proceedings of the 23rd Scottish Universities Summer School in Physics - NATO Advanced Study Institute, 1982).
6. T.W. Hänsch, Appl. Optics., <u>11</u>, 895 (1972).
7. I. Shoshan, N.N. Danon and U.P. Oppenheim, J. Appl. Phys., <u>48</u>, 4495 (1977).
8. S. Gerstenkorn and P. Luc in 'Atlas du spectre d'absorption de la molécule d'iode, 14000-20000 cm^{-1}', (Editions du C.N.R.S., Paris, 1978).
9. F.M. Behlen and S.A. Rice, J. Chem. Phys., <u>75</u>, 5672 (1981).

10. T.E. Adams, R.J.S. Morrison and E.R. Grant, Rev. Sci. Instrumen., 51, 141 (1980).

11. J.F. James and R.S. Sternberg in 'The Design of Optical Spectrometers', (Chapman and Hall Ltd., London, 1969).

12. P. Hariharan in 'Optical Holography - Principles, Techniques and Applications", (Cambridge University Press, 1984).

13. D.A. Fraser in 'The Physics of Semiconductor Devices', 3rd edition, (Clarendon Press, Oxford, 1983).

14. CRC 'Handbook of Chemistry and Physics', 55th edition (1974-75), edited by R.C. Weast (CRC Press, Ohio, U.S.A.).

15. C.J. Nokes and R.J. Donovan, Chem. Phys., 90, 167 (1984).

16. D.S. King, P.K. Schenk, K.C. Smyth and J.C. Travis, Appl. Optics., 16, 2617 (1977).

17. J. Pfaff, M.H. Begemann and R.J. Saykally, Mol. Phys., 52, 541 (1984).

18. 'Massachusettes Institute of Technology Wavelength Tables' edited by G.R. Harrison, (Wiley, New York, 1939).

CHAPTER 4

MULTIPHOTON IONISATION SPECTROSCOPY OF HYDROGEN CHLORIDE

4.1 INTRODUCTION

A quantitative understanding of the excited electronic state, structure, and spectroscopy of HCl are important for a variety of reasons. Useful quantitative data are required for the study not only of the photochemistry of planetary atmospheres [1] but the interstellar medium as well [2,3]. For example, chlorine compounds in the stratosphere of the Earth are of environmental importance because they disturb the balance of ozone at altitudes above 25 km [1]. HCl is a stable molecule in the stratosphere and it can only be removed by chemical reactions (mainly with OH) and photodissociation. HCl has also been found in the atmosphere of Venus [1] and is predicted to exist in detectable amounts in those interstellar clouds containing both hydrogen and chlorine [2,3] where it is destroyed mainly by photodissociation.

HCl is one of the most studied molecules in the field of reaction dynamics [4] and plays a central role in chemical laser action [5]. For these studies a spectroscopic technique having both high sensitivity and high resolution is desirable. The most commonly used method in the past has been infra-red fluorescence [6].

Laser-induced fluorescence and resonance-enhanced multiphoton ionisation (REMPI) are also very sensitive techniques for the detection of gas phase molecules. A number of research investigations have exploited REMPI detection techniques to study the dynamics of gas-gas reactive scattering [7], gas-surface scattering [8], surface desorption [9] and rotational energy transfer in the gas phase [10]. However, these require an intimate knowledge of the behaviour of excited electronic states as 'stepping stones' to the ionisation continuum following a resonant single-photon or multiphoton excitation. Using photoelectron spectroscopy detailed aspects of excited state photoionisation dynamics can be studied [11]. Thus, if [2+1] REMPI detection of HCl is to be employed effectively the excited electronic state properties must be understood.

The remainder of this Chapter falls into two sections. Firstly, a brief discussion of electron configurations and their role in the excited electronic state spectroscopy of HCl, followed by an experimental study of the latter, using REMPI techniques both in a static (room temperature) cell and at low temperatures in a supersonic free jet expansion.

4.2 ELECTRONIC CONFIGURATIONS IN HCl.

The configurational description of both ground and electronically excited states of HCl is a difficult problem, currently of considerable interest and has been studied in several ab-initio quantum calculations [12-16]. The problem central to all this work is the difficulty in describing the nature of the orbital reached in the electronic promotion that transforms the ground electronic state into an excited state. Close to the first ionisation potential 'Rydberg' orbitals become accessible, i.e. an electron from a valence shell orbital has been excited into a non-bonding atomic orbital of higher principal quantum number. Electron promotion into such orbitals gives rise to a dense set of Rydberg states. Similarly, in general terms, electron promotions to the non-bonding and/or anti-bonding valence shell orbitals lying above the highest occupied orbital of the ground state configuration gives rise to a manifold of 'Valence' excited states. Weak interactions between these 'Rydberg' and 'Valence' diabatic Born-Oppenheimer states [17] reveal themselves as local perturbations in the associated vibrational and rotational level structure. Stronger interactions frequently give rise to 'avoided-crossings' [17] between diabatic potential energy surfaces of the same electronic symmetry. This then necessitates detailed electronic structure calculations to establish which electronic configuration makes the dominant contribution at a given region to the resultant 'adiabatic' potential function.

The ground electronic state of HCl, X $^1\Sigma^+$, close to the equilibrium separation, is characterised by the configuration $\phi_1 = \ldots 4\sigma^2\ 2\pi^4\ 5\sigma^2$ where the 5σ orbital is a bonding orbital formed from Cl $3p_z$ and H 1s atomic orbitals. The dissociation at long bond length of the ground state to Cl (^2P) and H(^2S) requires an additional configuration $\phi_2 = ...4\sigma^2\ 2\pi^4\ 5\sigma\ 6\sigma^*$, where $6\sigma^*$ is the anti-bonding partner of the 5σ orbital. At intermediate bond length a third configuration $\phi_3 = ...4\sigma^2 2\pi^4 6\sigma^{*2}$ has been shown to contribute [12]. The hydrogen contribution is present in the 4σ (at very small internuclear separations), 5σ and $6\sigma^*$ molecular orbitals. The 4σ orbital is essentially the Cl 3s atomic orbital. The hydrogen contribution decreases steadily in the 5σ orbital as the bond length is increased, conversely the $6\sigma^*$ acquires more and more hydrogen admixture. Thus at large internuclear separation HCl possesses predominantly covalent character while close to the equilibrium geometry strong ionic $H^+...Cl^-$ contributions from the double occupation of the 5σ or $6\sigma^*$ orbitals exist [12].

The excited electronic states in HCl result from excitation into the anti-bonding $6\sigma^*$ molecular orbital and into various s,p and d members of the Rydberg series. The Rydberg limit, i.e. the $^2\pi$ HCl^+ ion lies at 12.75 and 12.83 eV for the $^2\pi_{3/2}$ and $^2\pi_{1/2}$ states, respectively. The dominant electronically excited state of HCl is the $^1\Sigma^+$ 'Ion-pair' state, the existence of which was predicted by Pauling as early as 1932 [18]. This undergoes an essentially complementary change in character to that of the ground state: covalent character prevails at small and intermediate internuclear distances while ionic character becomes dominant at large separations, for which dissociation leads diabatically to the products H^+ and Cl^-. Thus the ground and 'Ion-pair' states essentially form an avoided crossing, as can be seen by the 'non-adiabatic' matrix coupling element, $\langle X\ {}^1\Sigma^+ | \frac{\partial}{\partial R} | B\,{}^1\Sigma^+ \rangle$, between the two states [12]. Not surprisingly then the 'Ion-pair' state has some unusual properties (see Figure 4.1). The equilibrium internuclear separation is considerably longer than that

TABLE 4.1

ELECTRONIC CONFIGURATION*	STATE
... $5\sigma^2\ 2\pi^4$	X $^1\Sigma^+(0^+)$
... $(5\sigma^2 2\pi^3)6\sigma^*$	a $^3\Pi_i(2,1,0)$, A $^1\Pi(1)$
... $(5\sigma 2\pi^4)6\sigma^*$	t $^3\Sigma^+(1,0^-)$, V or B $^1\Sigma^+(0^+)$
... $(5\sigma^2 2\pi^3)4s\sigma$	b $^3\Pi_i(2,1,0\ )$, C $^1\Pi(1)$
...$(5\sigma^2 2\pi^3)4p\sigma$	d $^3\Pi_i(2,1,0\ )$, D $^1\Pi(1)$
...$(5\sigma^2 2\pi^3)4p\pi$	e $^3\Sigma^+(1,0^-)$, E $^1\Sigma^+(0^+)$
	f $^3\Delta_i(3,2,1)$, F $^1\Delta(2)$
	g $^3\Sigma^-(1,0^+)$, G $^1\Sigma^-(0^-)$

*Note: close to equilibrium internuclear separation.

of the ground state and the other Rydberg states. Obviously the attractive limb of the 'Ion-pair' state is dominated by ionic forces. The repulsive inner limb cuts through the entire Rydberg state electronic manifold possessing minima at small bond lengths and causes

FIGURE 4.1 Some ab-initio potential energy curves for HCl. (Ref. [16]).

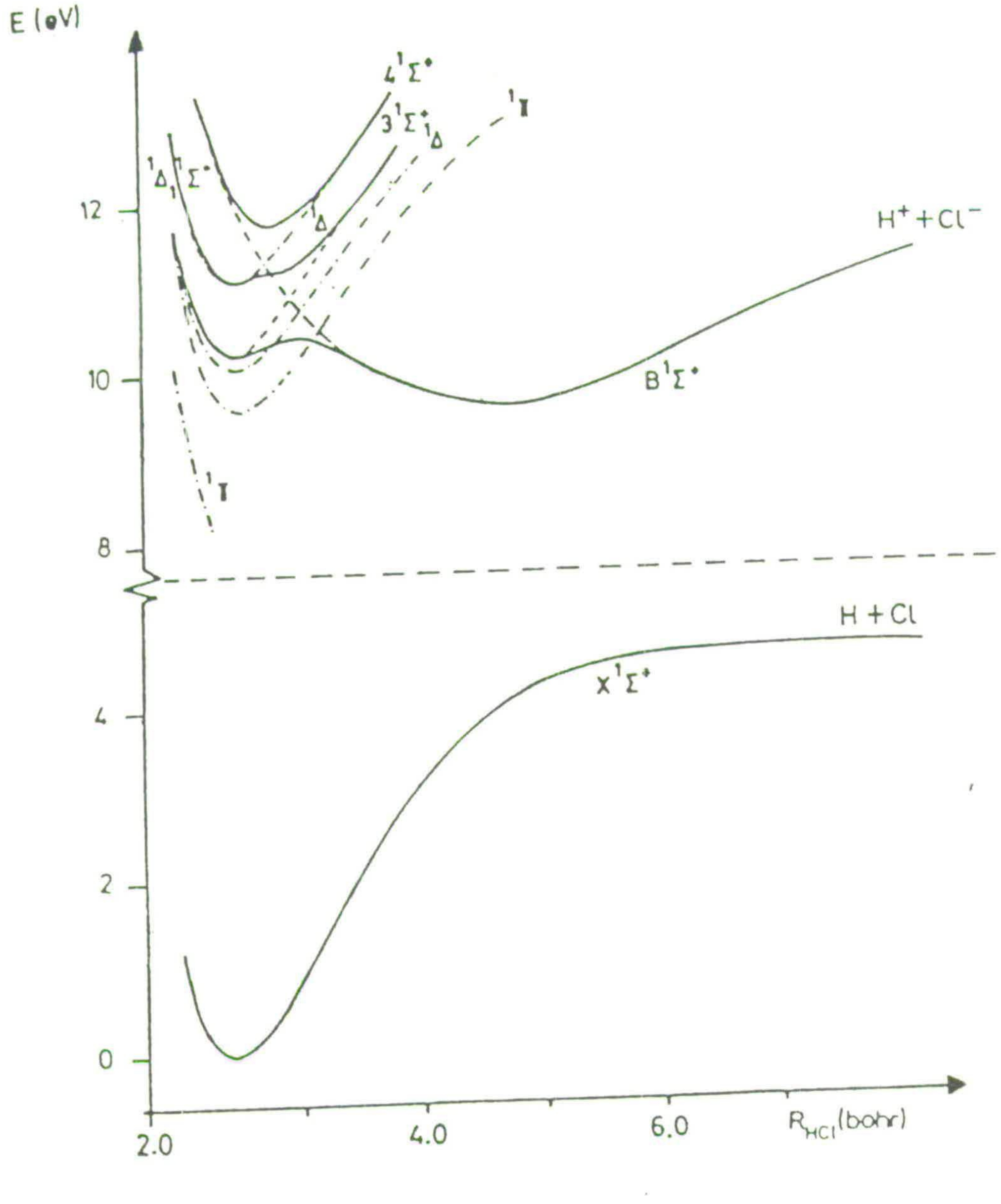

various perturbations with other members of the same electronic symmetry.

The lowest lying configurations and the corresponding electronic states derived from them are listed in Table 4.1. The 'V' notation for the 'Ion-pair' B $^1\Sigma^+$ state was that originally used by Mulliken [19] and adopted by Ginter et al [20,28,29] in their spectroscopic work. The configurations with $(\sigma^2\pi^3)$ are based on the $(\sigma^2\pi^3)X\ ^2\Pi_i$ (where $i = \frac{3}{2},\frac{1}{2}$) ground core of the molecular ion. The X, a, A and t states are correlated with the ground state atomic limit and all but the X state have repulsive energy curves. Note that the B $^1\Sigma^+$ 'Ion-pair' state might be regarded as a core ancestor of a Rydberg state associated with the $(\sigma\pi^4)$ A $^2\Sigma^+$ excited ion core. Following the spectroscopic notation of Tilford and Ginter [20], both the Λ, S and Ω,ω notations are indicated, as there are often major changes in couplings within molecules and/or configurations [21]. It is useful to retain both Λ, S and Ω,ω notations since often the former are more descriptive in discussions of state ancestry and the latter are a better representation of angular momentum coupling.

The theoretical description of the excited electronic states of HCl has proved particularly difficult, especially for those of Σ^+ symmetry. For these states heavy mixing between the $\sigma - \sigma^*$ valence (see Table 4.1) and Rydberg states is to be expected. The interaction between the 'Ion-pair' state and Rydberg states of the same symmetry is so strong that Peyerimhoff et al [12] predict various 'avoided-crossings' and the formation of at least one distinct double-minimum potential. Their results predict that the interaction with the 'Rydberg' species took place well away from the 'Rydberg' potential minimum giving rise to a 'symmetric' double minimum, similar to that of the E, F state in H_2[22]. However, the predicted vibronic level structure of this HCl double-minimum state has not been ratified by spectroscopic observation. More recently, with improved calculations, this interaction between the 'Ion-pair' and 'Rydberg' states has been shown to occur much closer to the 'Rydberg' minimum [16,23] similar to the situation in HF [24]. An 'asymmetric' double-minimum potential results with the inner 'Rydberg' minimum supporting several vibrational levels [23]. Despite the sophistication of the ab-initio calculations the resulting potentials support vibrational and rotational level structure which is still in poor agreement with known spectroscopic data.

Conventional spectroscopic studies of HCl using high resolution vacuum ultra-violet (VUV) absorption and emission spectroscopy span a period of fifty years. Romand [25] in 1949 noted the existence of an absorption continuum in the region 44,000-60,000 cm^{-1}. Some nine years later, emission from an electronically excited state was first studied by Jacques and Barrow [26]. The latter observed emission from the first four levels of the 'Ion-pair' B $^1\Sigma^+$ state to high vibrational levels associated with the ground electronic state. Subsequently, Douglas and Greening [27] by high resolution VUV absorption measurements extended observations up to $v' = 26$ of this state and established the symmetry and spectroscopic constants for other states. They also made measurements of the corresponding states in DCl. Ginter and co-workers [20,28,29] have also performed extensive spectroscopic studies of HCl and have assigned much of the VUV absorption spectrum up to ~ 94,000 cm^{-1}. Most recently, Coxon and Roychowdhury [30] have extended studies on the B - X system using discharge excited emission spectroscopy. From the measured line positions they were able to obtain Rydberg-Klein-Rees (RKR) [31-34] turning points for the 'Ion-pair' B $^1\Sigma^+$ potential over the first seven vibrational levels. Their analysis did not extend beyond vibrational level $v' = 6$ because, from the VUV absorption data, extensive perturbations of the 'Ion-pair' state, due to mixing with other $^1\Sigma^+$ or 0^+ states, were only too obvious.

In the present work [2+1] REMPI spectroscopy has been performed over selected regions between 75,000 and 90,000 cm^{-1}. The results can be compared with previous single-photon VUV absorption measurements and the recent work of Gordon et al [35,36] and Parker et al [37] both of whom have also used the REMPI technique.

4.3 MULTIPHOTON IONISATION SPECTROSCOPY

[2+1] REMPI spectroscopy at relatively low resolution can be used for assignment of the electronic state, however much higher resolution was employed over selected regions where accurate line positions were to be determined. Table 4.2 lists all of the states and the vibrational and rotational transitions observed in the energy region 75,000-90,000 cm^{-1}. In the following discussion the spectroscopic notation as used by Ginter et al [20,28,29] will be adopted.

4.3.1 π AND Δ SYMMETRY STATES

In contrast to one-photon absorption, transitions to Δ symmetry states are fully allowed by two-photon selection rules. In this study the f $^3\Delta_3$, f$^3\Delta_2$ and F$^1\Delta_2$ states were identified. The observation of the f $^3\Delta_3$ state is surprising and suggests some kind of 'intensity borrowing' from the f $^3\Delta_2$ and $^3\Delta_1$ states which are allowed by two-photon transitions from the ground state. They displayed some or all of the expected O,P,Q,R, and S branches, corresponding to a change in rotational quantum number J = -2, -1, 0, +1, +2 respectively. The states have been previously seen as weak absorptions [20] in single-photon high resolution VUV absorption spectra. Electric dipole selection rules for single-photon transitions forbid a $^1\Delta-^1\Sigma^+$ or a $^3\Delta-^1\Sigma^+$ electronic transition, but they are weakly allowed owing to spin-orbit interactions as discussed by Kovács [38]. Thus, in addition to the transitions $\Delta S = 0$, $\Delta\Lambda = 0, \pm 1$ permitted under electric dipole selection rules, the transitions $\Delta S = \pm 1$ and $\Delta\Lambda = \pm 2$ will also be possible. The two-photon induced rotational transitions identified for the f $^3\Delta_2$ and $^3\Delta_3$ states are as shown in Table 4.2. It is

TABLE 4.2

STATE OBSERVED	$H^{35}Cl$ ELECTRONIC ENERGY, T_o/cm^{-1}	ROTATIONAL TRANSITIONS
d $^3\pi_1$; v'=0	81,773.2	Q(1,2); P(2-4); S(0-4); R(0-4)
f $^3\Delta_3$; v'=0	81,825.8	Q(3-7); P(4,5); R(2-7)
f $^3\Delta_2$; v'=0	82,015.1	Q(2-8); P(3-7); S(0-6); R(1-6)
D $^1\pi$; v'=0	82,489.7	Q(1-6); P(2-5); R(1-4); S(0-3)
B $^1\Sigma^+$; v'=9	82,839.8	Q(0-5)
F $^1\Delta_2$; v'=0	82,847.1	Q(2-8); R(1-8,10); S(0-8); P(3-8); O(4-6)
g $^3\Sigma^-(0^+)$; v'=0	83,087.7	Q(0-6)
B $^1\Sigma^+$; v'=10	83,434.1	Q(0-4)
E $^1\Sigma^+$; v'=0	83,780.2	Q(0-8);O(2-6); S(0-3)
B $^1\Sigma^+$; v'=11	84,207.7	Q(0-8); S(0-3); O(2-6)
B $^1\Sigma^+$; v'=12	84,746.9	Q(0-6); S(0-3); O(2-5)
B $^1\Sigma^+$; v'=13	85,277.6	Q(0-4,7,8);O(2,3); S(0,1)
F $^1\Delta_2$;v'=1	85,363.7	Q(2-8); R(1-6); S(0-4); O(5,6); P(3,5,6,8,9)

STATE OBSERVED	H^{35}Cl ELECTRONIC ENERGY, T_o/cm^{-1}	ROTATIONAL TRANSITIONS
B $^1\Sigma^+$; v'=14	85,672.9	Q(0-3)
E $^1\Sigma^+$; v'=1	85,918.7	Q(0-5); S(0)
B $^1\Sigma^+$; v'=15	86,405.7	Q(0-8); S(0-3); O(2-5)
B $^1\Sigma^+$; v'=16	86,931.9	Q(0-9); S(0-4); O(2-5)
B $^1\Sigma^+$; v'=17	87,464.5	Q(0-6)
n $^3\Pi_1$; v'=0	87,658.5	Q(2-7); R(1-9)
D $^1\Pi$; v'=2	87,675.6	R(0-3)
B $^1\Sigma^+$; v'=18	87,967.6	Q(0-7); S(0-3) O(2-5)

interesting to note that no transitions to the f $^3\Delta_1$ state could be identified. This band, as seen in VUV absorption, was somewhat weak with diffuse rotational structure [20]. No H^{35}Cl, H^{37}Cl isotopic splitting was resolved, as expected for bands formed as a result of transitions from the v" = 0 vibrational level in the ground state to a v' = 0 level in a Rydberg state [21]. In addition no transitions to higher vibrational levels were observed consistent with previous work [20,28,29]. Figure 4.2 shows the characteristic, un-normalised (i.e. not corrected for variations in UV laser pulse energy) spectrum for the f $^3\Delta_2$ - X $^1\Sigma^+$ (0-0) transition observed by REMPI of HCl with linearly polarised light. The P,Q,R, and S rotational transitions are as indicated. Figure 4.3 shows the assigned transitions to the f $^3\Delta_3$ and d $^3\Pi_1$ states. The transitions underlined belong to the d $^3\Pi_1$ state, those not underlined belong to the f $^3\Delta_3$

FIGURE 4.2 [2 + 1] REMPI spectrum of the f $^3\Delta_2$ — X $^1\Sigma^+$ (0 — 0) transition.

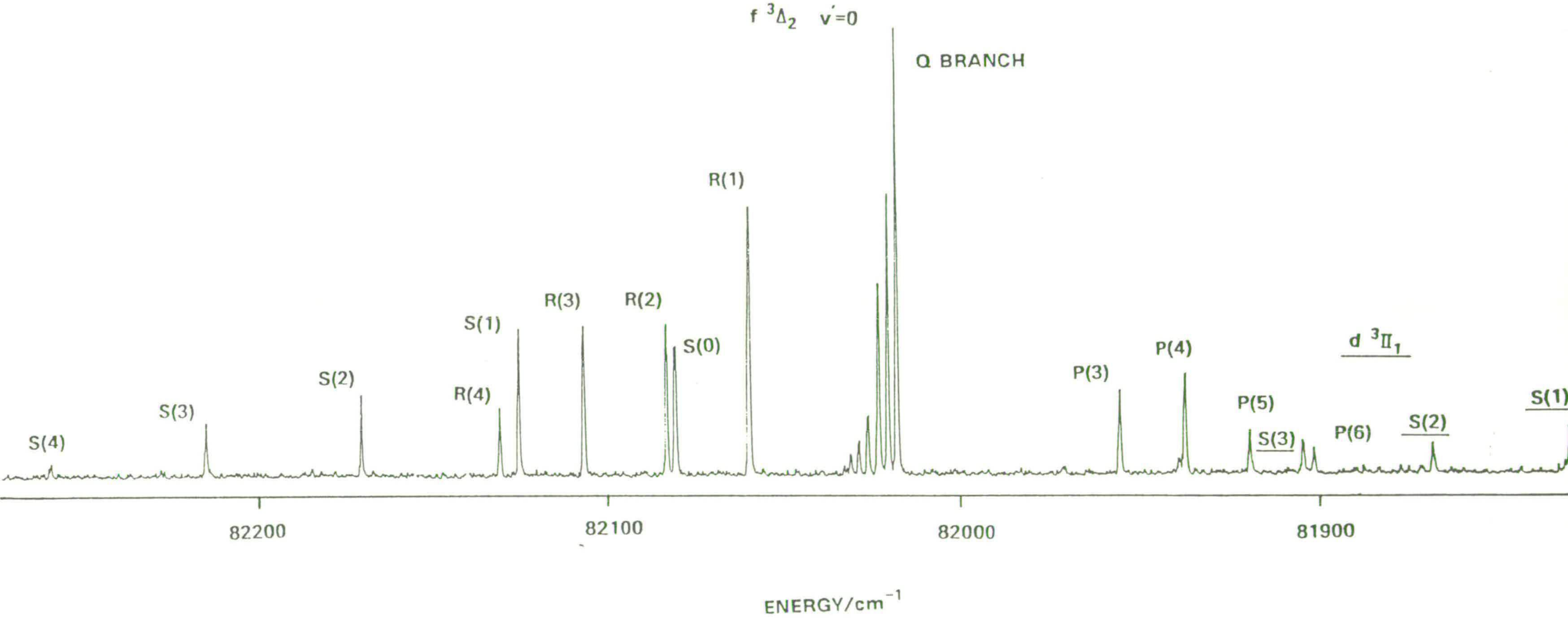

FIGURE 4.3 [2 + 1] REMPI spectrum in the region ~ 81700 cm^{-1} — ~ 82000 cm^{-1}.

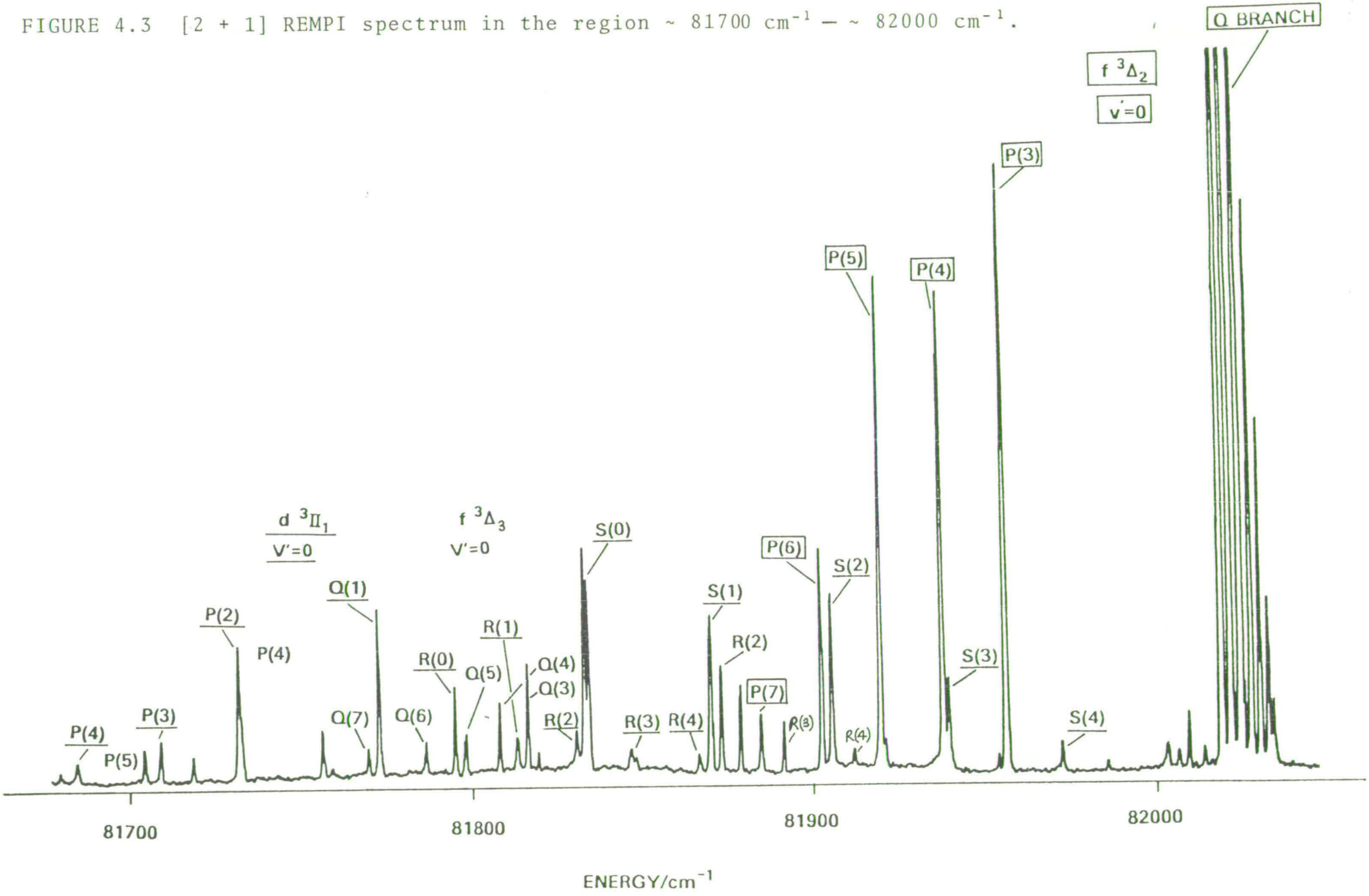

state and those enclosed in a box belong to the f $^3\Delta_2$ state.

There has been some uncertainty in the assignment of the F $^1\Delta_2$ state of HCl. Tilford and Ginter [20] having identified the $^3\Delta_1$, $^3\Delta_2$ and $^3\Delta_3$ states in the 82,000cm^{-1} region predicted that the corresponding $^1\Delta_2$ state should lie near 82,900cm^{-1}, a few hundred wavenumbers above the origin of the $^3\Delta_1$ state (~82,523 cm^{-1}). They also expected to see the g $^3\Sigma^-$ and G $^1\Sigma^-$ origins in this region. Initially they found P,Q and R branches which they were able to follow to R(0). The P branch, and to some extent the Q branch, was overlapped by the strong, diffuse C $^1\pi$(2-0) absorption (~82,725cm^{-1}). They assigned the lines near 82,900cm^{-1}, as belonging to the vibrational origin of a state with $\Omega = 1$ symmetry, in fact the g $^3\Sigma^-$ state, $\Omega = 1$ spin-orbit component. Douglas and Greening [27] recorded a spectrum at a lower temperature and found that the R(0) line disappeared indicating that it was actually a high rotational line from some other state and that the R branch ends at R(1). On this basis they assigned the lines observed to the F $^1\Delta_2$ $v' = 0$ level. This work confirms the latter assignment since the O,P,Q,R, and S branches observed clearly belong to a state of Δ symmetry. The lowest rotational transitions are O(4), P(3), Q(2), R(1) and S(0) respectively for each branch. Figure 4.4 shows the power-normalised F $^1\Delta_2$ - X $^1\Sigma^+$ (0-0) REMPI spectrum obtained with linearly polarised light. Note, there is

FIGURE 4.4 Power-normalised F $^1\Delta_2$ — X $^1\Sigma^+$ (0 — 0) REMPI spectrum.

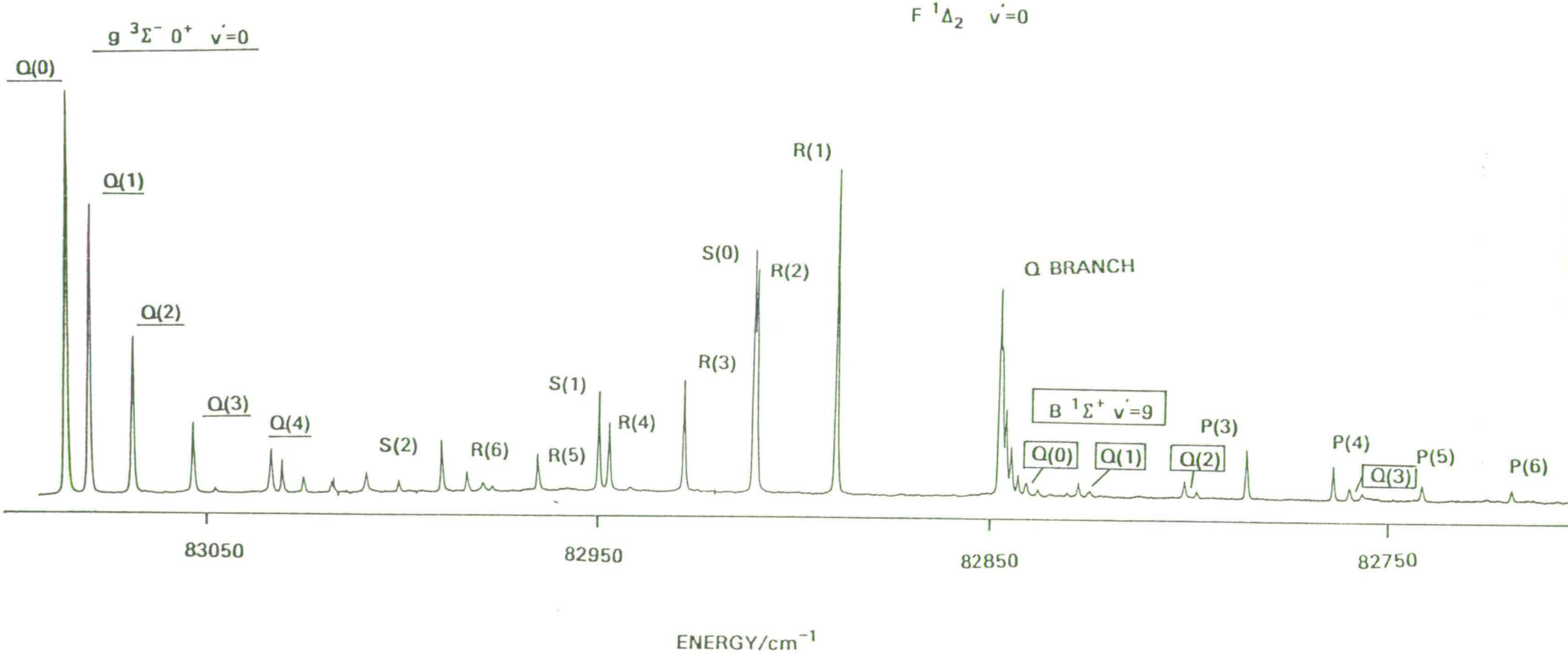

no interference from the strong, but diffuse C $^1\pi$ - X $^1\Sigma^+$ (2-0) absorption around 82,725cm^{-1} which plagued previous work [20,27]. Here, then we see a classic illustration of the complementary nature of conventional VUV absorption and REMPI studies of electronically excited states. Thus the REMPI spectra tend to be dominated by the less heavily predissociated 'Rydberg' states with little or no contribution from the inevitable short lived, highly dissociative excited states like the C $^1\Pi$ state which give rise to diffuse or broad, continuous features in one-photon spectra. Recently, Ashfold et al [39] have used a combination of both techniques to study the electronic spectra of H_2S and D_2S.

The F $^1\Delta_2$ - X $^1\Sigma^+$ (1-0) transition was also observed in the present work and the $H^{35}Cl$, $H^{37}Cl$ isotopic splitting was clearly visible (see Figure 4.5). The origin of the F-X (1-0) transition at 85,363.7cm^{-1} differs from the value 85,383.3cm^{-1} reported by Ginter and Ginter [29]. Their assignment was based on a portion of the R branch and it would be easy therefore to assign the J values incorrectly if any of the lines were missing. In addition, no other branches could be seen. In the two-photon spectrum we have a clear picture of the O,P,Q,R, and S branches making determination of J values and band origins unambiguous. These, and results for transitions to the F $^1\Delta_2$ state in DCl, will be discussed in more detail (see section 4.4).

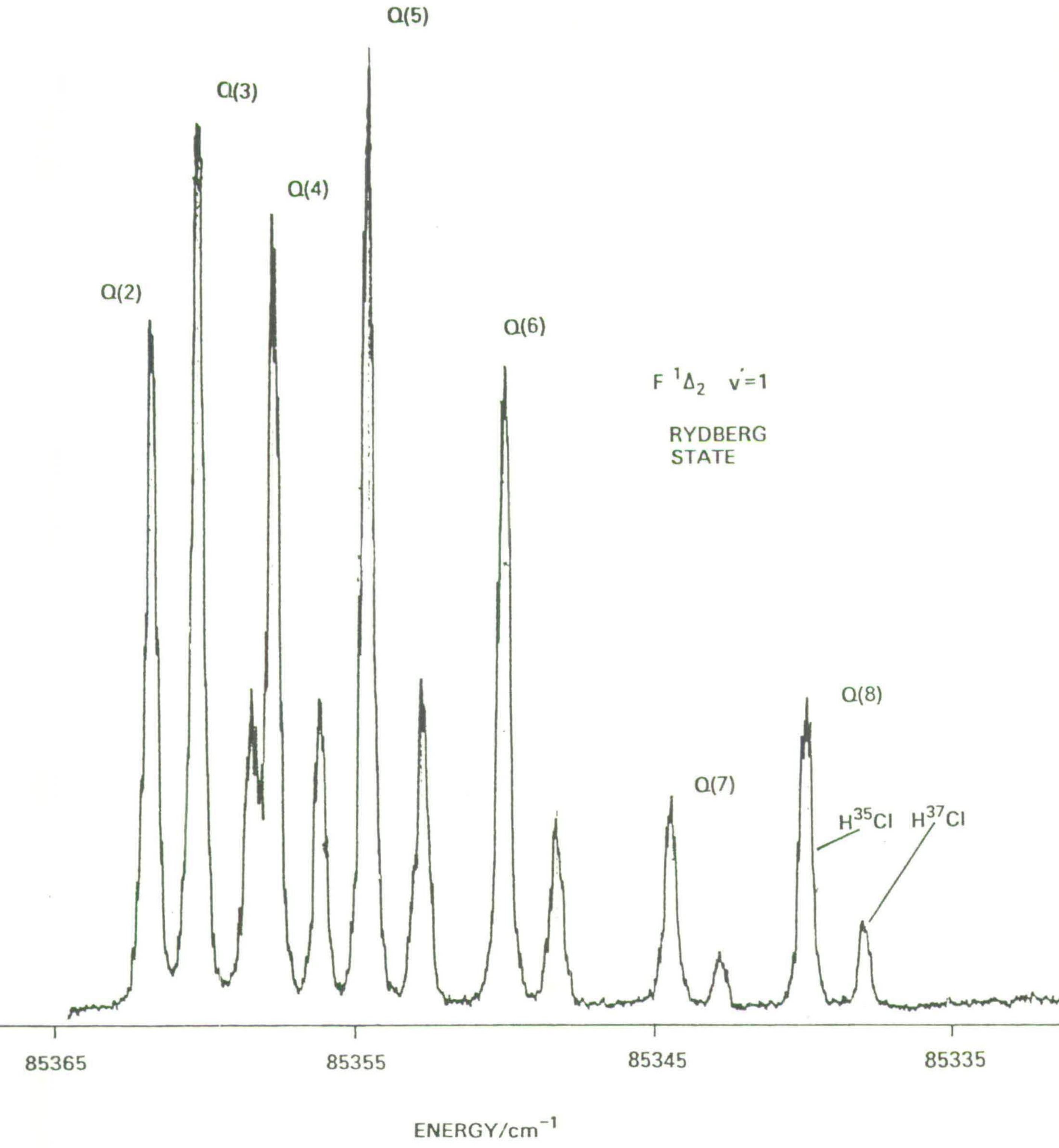

FIGURE 4.5 Q-branch of the F $^1\Delta_2$ — X $^1\Sigma^+$ (1 — 0) REMPI spectrum.

The $^1\pi$ and $^3\pi$ states of HCl have been well characterised, primarily by Tilford and Ginter [28], in the region 75,000-90,000cm^{-1}, with those dominant characterised as the b $^3\pi_i$ (i=0,1,2) and C $^1\pi$ Rydberg states. Both these states have large oscillator strengths in absorption [40,41] and have increasingly diffuse rotational structure as the vibrational quantum number is increased. Smith et al [40] measured the rotational linewidth at full-width half-maximum (f.w.h.m.) of the C $^1\pi$ - X $^1\Sigma^+$ (0-0) absorption to be typically ~3.3cm^{-1}, suggesting an excited state lifetime of ~10ps. For the (1-0) transition the rotational linewidth for the R(0) line was measured to be ~8.8cm^{-1}. These measurements were considerably greater than the instrumental resolution which was determined to be ~1 cm^{-1} (f.w.h.m.). The diffuseness in rotational structure is indicative that the b and C states are strongly predissociative. The non-observation of fluorescence from these states following single-photon excitation by synchrotron radiation [41] further confirms the rapid loss of the excited state by some non-radiative process. This predissociation also has important implications for laser multiphoton spectroscopy. Despite extensive searching no multiphoton excited fluorescence or ionisation of the b $^3\pi_i$ or the C $^1\pi$ states of HCl could be detected. This observation further confirms that predissociation is indeed the dominant loss process of the excited state and dominates any radiative losses and 'up-pumping' to the ionisation continuum. Ab-initio calculations of the potential energy surfaces [12,16] show that the C $^1\pi$ and b $^3\pi_i$ states are crossed by the repulsive $^3\Sigma^+$ continuum. As expected however, for DCl, VUV absorption spectra of the b $^3\pi_i$ and C $^1\pi$ states showed considerably more discrete rotational structure [28]. They were still sufficiently unstable to preclude observation by multiphoton techniques.

In contrast fragments of the d $^3\pi_1$, n $^3\pi_1$ and D $^1\pi$ states could be detected for HCl. Weak P,Q,R, and S branch rotational transitions are as listed in Table 4.2. The observation of these states and not the b $^3\pi_i$ and C $^1\pi$ states is not fully understood but presumably must reflect the greater stability of the excited electronic state. No transitions to the $^3\pi_2$ and $^3\pi_o$ spin-orbit components of the d state could be identified despite their observation in VUV absorption [20]. Only vibrational levels v' = 0 of the d $^3\pi_1$ and n $^3\pi_1$ states could be seen, in agreement with the observation of these states in previous work [28,29]. For the D $^1\pi$ state only the v' = 0 and v' = 2 vibrational levels were observed. The D $^1\pi$ v' = 1 level was not detected. From VUV absorption data [29] the region where it may be expected to have been found ($\sim$85,000cm^{-1}) was completely diffuse, with a major contribution coming from the C $^1\pi$ - x $^1\Sigma^+$ (3-0) absorption.

The observation of the above $^3\pi$ and $^1\pi$ states is in marked contrast to the work of Gordon et al (36) who claim not to observe any π symmetry states, apart from d $^3\pi_1$, in their REMPI study of HCl. They erroneously attribute this to $^1\pi$ - $^1\Sigma^+$ or (1-0^+) two-photon transitions being forbidden, which is not the case [42-44] and have failed to recognise the short-lived nature of most of the $^1\pi$ and $^3\pi$ states, which precludes their detection in MPI experiments. In addition their observed band origins are markedly different from those quoted in this work, which agree closely with previous observations [20,27-29].

4.3.2 $^1\Sigma^+$ STATES

The spectroscopic characteristics of the $^1\Sigma^+$ or 0^+ states are probably the most complex and interesting to study. Where the B $^1\Sigma^+$ 'Ion-pair' state cuts through the 'Rydberg' series then strong mixing with electronic states of $^1\Sigma^+$ or 0^+ symmetry can occur. The B $^1\Sigma^+$ state of HCl is the dominant excited state and a long progression in vibrational levels has been analysed [26,27,30]. The vibrational spacing and rotational constants vary erratically above vibrational level V'=8, indicative of strong perturbations. The v' = 9 - 19 vibrational levels were observed in REMPI spectroscopy in the region 82,000-89,000 cm^{-1}. The rotational transitions seen are as listed in Table 4.2. The selection rules predict that O,Q and S branches, corresponding to changes in rotational quantum number ΔJ = -2,0, and +2, respectively, should be observed, with the Q branches dominant. Figure 4.6 shows two typical electronically excited $^1\Sigma^+$ states, as observed during the REMPI of ground state HCl. Namely the 'Ion-pair' state B $^1\Sigma^+$, v' - 11 vibrational level and the v' = 0 level of the E $^1\Sigma^+$ state which is strongly vibronically coupled to the 'Ion-pair' state, hence the nomenclature 'Coupled-Rydberg' state. The spectrum was recorded with linearly polarised laser light and has not been corrected for any fluctuations in laser power. Note the dominant Q branch structure and the relatively weak 0 and S branch rotational transitions. The observed line intensities for the E $^1\Sigma^+$ - X $^1\Sigma^+$ transition will be discussed in more detail later.

No vibrational levels below v' = 9 (T_o=82, 839.8cm^{-1}) in the 'Ion-pair' state could be accessed, presumably due to poor Franck-Condon overlap with the ground electronic state. The low signal intensity of the v' = 10 vibrational level (T_o=83,434.1cm^{-1}) and the v' = 14 level (T_o=85,672.9cm^{-1}) may be due to perturbations with the E $^1\Sigma^+$ state. The anomalous low intensity of these 'Ion-pair' state vibrational levels may be due to intensity borrowing by the nearby E $^1\Sigma^+$, v' = 0 (T_o=83,780.2cm^{-1}) and v' = 1 (T_o=85918.7cm^{-1}) vibrational levels, respectively. In addition, both the B $^1\Sigma^+$ (v'=10) and (v'=14) levels lie at lower energies than expected and both have noticeably higher values of the 'rotational constant' B_v', 4.808 cm^{-1} and 5.877 cm^{-1}, respectively, than the other vibrational levels in the

FIGURE 4.6 REMPI spectrum of the B $^1\Sigma^+$ v' = 11 and the E $^1\Sigma^+$ v' = 0 levels.

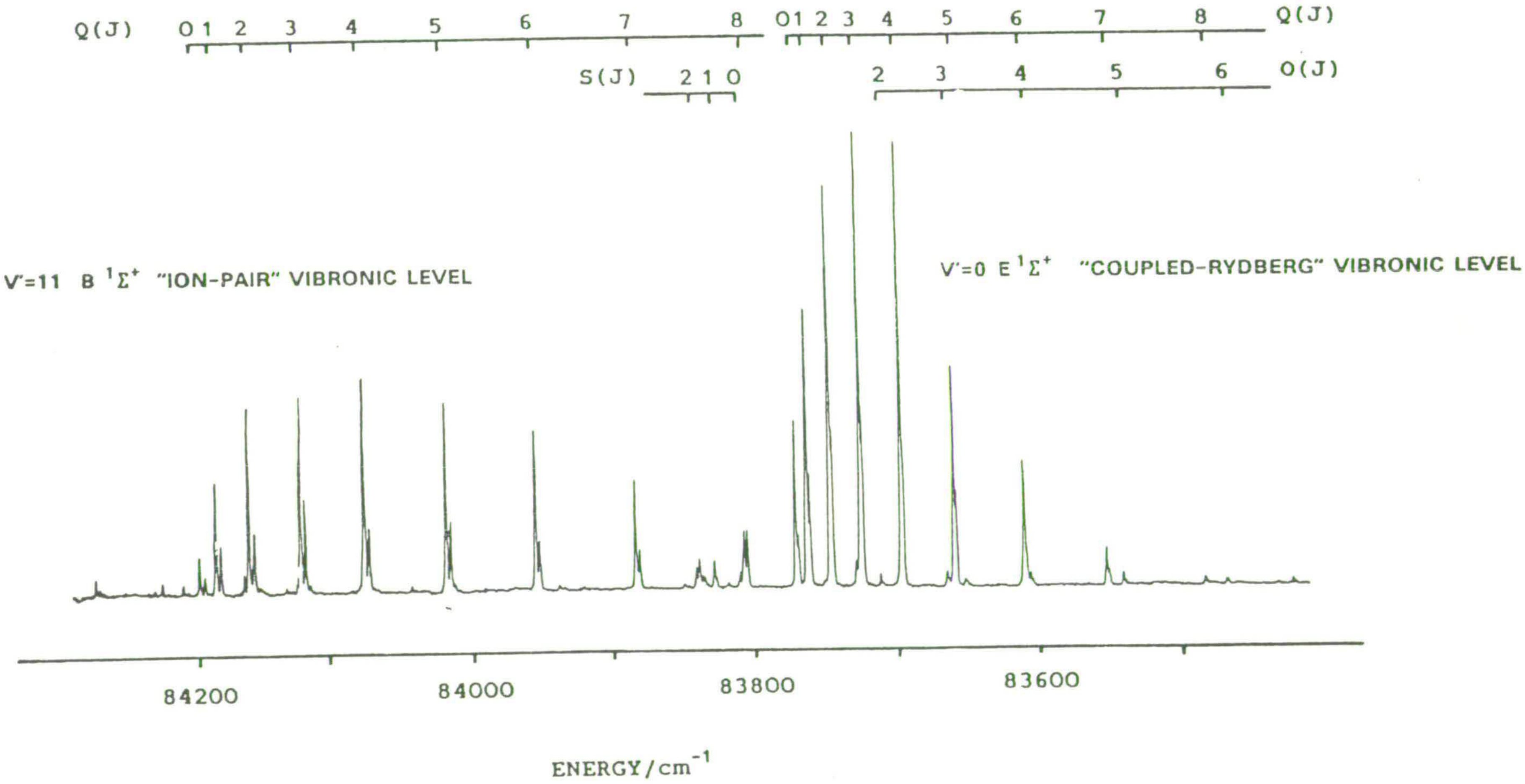

'Ion-pair' state. Hence, these data suggest a marked 'Rydberg' character of those levels. The B $^1\Sigma^+$, v'=18 level (T_o=87,967.6cm^{-1}) and the v' = 19 level (T_o=88,565.5cm^{-1}) may also be perturbed by the adjacent E $^1\Sigma^+$, v'=2 (T_o=88,145cm^{-1}) and the H $^1\Sigma^+$, v'=0 (T_o=88,684.5cm^{-1}) vibrational levels [29].

The B $^1\Sigma^+$, v' = 13 and v' = 16 vibrational levels show some interesting anomalies in their rotatinal line intensity. The lines of the B $^1\Sigma^+$ - X $^1\Sigma^+$ (13-0) band are relatively sharp for high and low J' values, but are extremely weak and diffuse for intermediate (J' 4-6) values (see Figure 4.7). From single-photon VUV studies [28,29] this spectral region also contains the completely diffuse C $^1\pi$ - X $^1\Sigma^+$ (3-0) band and fragments of other predissociated states, one being possibly the f $^3\Delta_1$ v' = 1 level. It is possible then that this very local predissociation is heterogeneous via the f $^3\Delta_1$, D $^1\pi$ or the C $^1\pi$ states. Those rotational levels that are at closest resonance with the diffuse state are the most heavily predissociated.

Perhaps even more interesting is the strange intensity distribution in the Q branch of the B $^1\Sigma^+$ - X $^1\Sigma^+$ (16-0) transition (see Figure 4.8). The Q(0) line is very weak and the Q(7) line is less intense than expected. Note also that the rotational line intensity increases between J' = 0 and J' = 5. The reason for this behaviour is not understood fully, but again it may involve predissociative loss of the excited

FIGURE 4.7 REMPI spectrum of the B $^1\Sigma^+$ — X $^1\Sigma^+$ (13 — 0) transition.

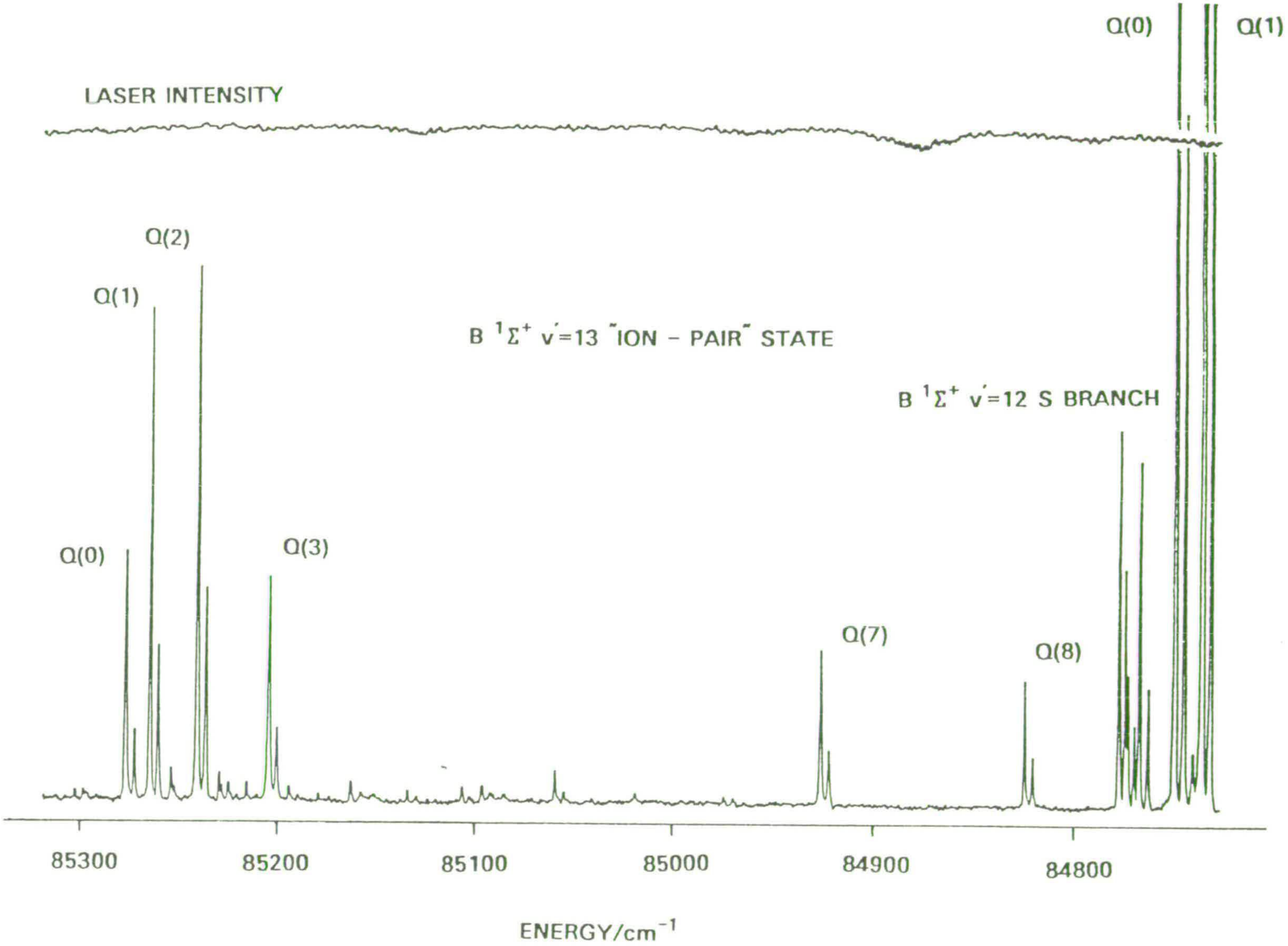

FIGURE 4.8 REMPI spectrum of the B $^1\Sigma^+$ — X $^1\Sigma^+$ (16 — 0) transition.

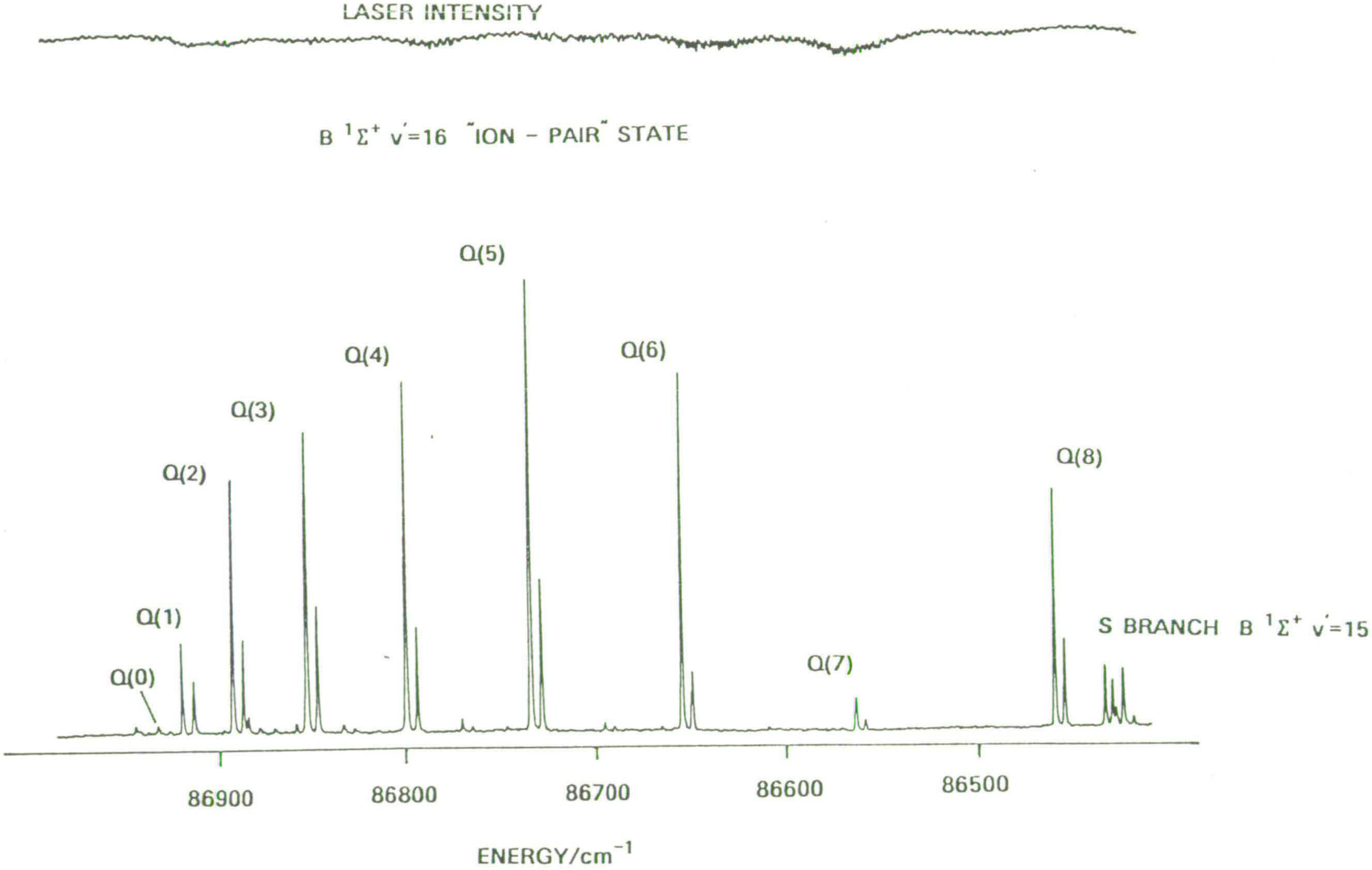

state population. In both Figures 4.7 and 4.8 the UV laser light intensity is as shown. The pulse-to-pulse fluctuation is comparatively small, being ~5% of the average pulse energy. The spectra are not power-normalised as the dependence of the ionisation signal on the laser intensity for the two bands is not known.

The E $^1\Sigma^+$ state is likely then to be the $^1\Sigma^+$ or (0^+) state arising from the $(5\sigma^2 2\pi^3)$ $4p\pi$ 'Rydberg' configuration. Unlike the other $^1\pi$ and $^3\pi_i$ 'Rydberg' states, the rotational and vibrational frequencies of the E $^1\Sigma^+$ state are much lower than those of the ground state of the ion. The v' = 0 vibrational level shows a substantial chlorine isotope effect, which is not present for transitions to the vibrational origins of other 'Rydberg' states. Qualitatively these effects can be accounted for by assuming that there is a strong interaction between the E $^1\Sigma^+$ and B $^1\Sigma^+$ states. This mixing causes the 'rotational constants' B_v' of the vibrational levels of the B $^1\Sigma^+$ state to rise as the levels approach the lowest vibrational level of the E state. This pattern tends to repeat itself at the E $^1\Sigma^+$, v' = 1 vibrational level. At the same time the mixing causes a sharp reduction in the B_v' value of the E $^1\Sigma^+$ state and transfer of some of the large isotope effect of the B state to the E state. The situation may be further complicated by the presence of other interacting states such as the g $^3\Sigma^-(0^+)$ and the H $^1\Sigma^+$ states. (Figure 4.4 shows Q branch lines of the g $^3\Sigma^-(0^+)$ – X $^1\Sigma^+$ (0-0) transition). Thus designation of the $^1\Sigma^+$ or (0^+) states by single state and level labels represents only a best estimate of what may be one major contribution to the composition of an excited state.

Figure 4.9 shows the deviations of the observed vibrational level energies T_v [27] for the B $^1\Sigma^+$ state from their extrapolated values T_{CALC} for v' = 0 to 20. The solid squares represent the v' = 0-5 vibrational level data used to determine the extrapolation equation given by Tilford and Ginter [29] as:

$$T_v(\mathrm{cm}^{-1}) = 75{,}819.3 + 878.74(v+\tfrac{1}{2}) - 17.0165(v+\tfrac{1}{2})^2 + 0.2775(v+\tfrac{1}{2})^3 \qquad 4.1$$

where v is the 'Ion-pair' state vibrational quantum number.

The energies of non-B state $^1\Sigma^+$ or (0^+) vibrational levels known to exist in this region are indicated by vertical lines. Figure 4.10 shows a plot of the B $^1\Sigma^+$ 'rotational constants' as a function of vibrational level. In addition many of the vibrational levels of the B $^1\Sigma^+$ state above v' = 9 have large negative D_v centrifugal distortion constants [27] which further indicates their perturbed nature. The rotational constant B_v can be regarded then as a measure of the rotational expectation value $\langle R^{-2}\rangle$, where R is the internuclear separation [22]. Thus the observed spectroscopic data are a manifestation of the complex

FIGURE 4.9 Deviations of the observed vibrational level energies T_v for the B $^1\Sigma^+$ state from their extrapolated values T_{CALC} for v' = 0 to 20.

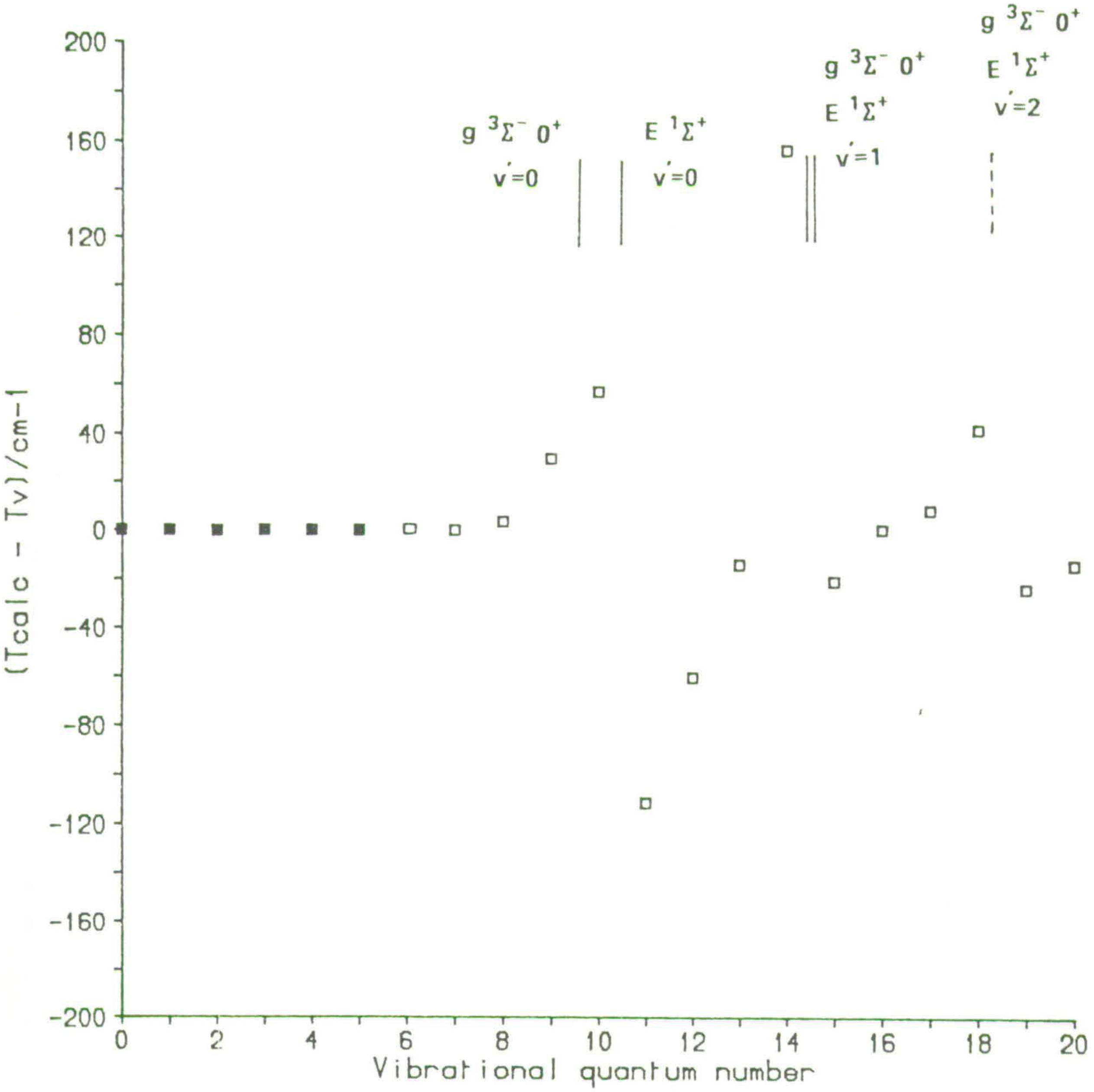

FIGURE 4.10 Plot of the B $^{1}\Sigma^{+}$ 'rotational constants' as a function of vibrational level.

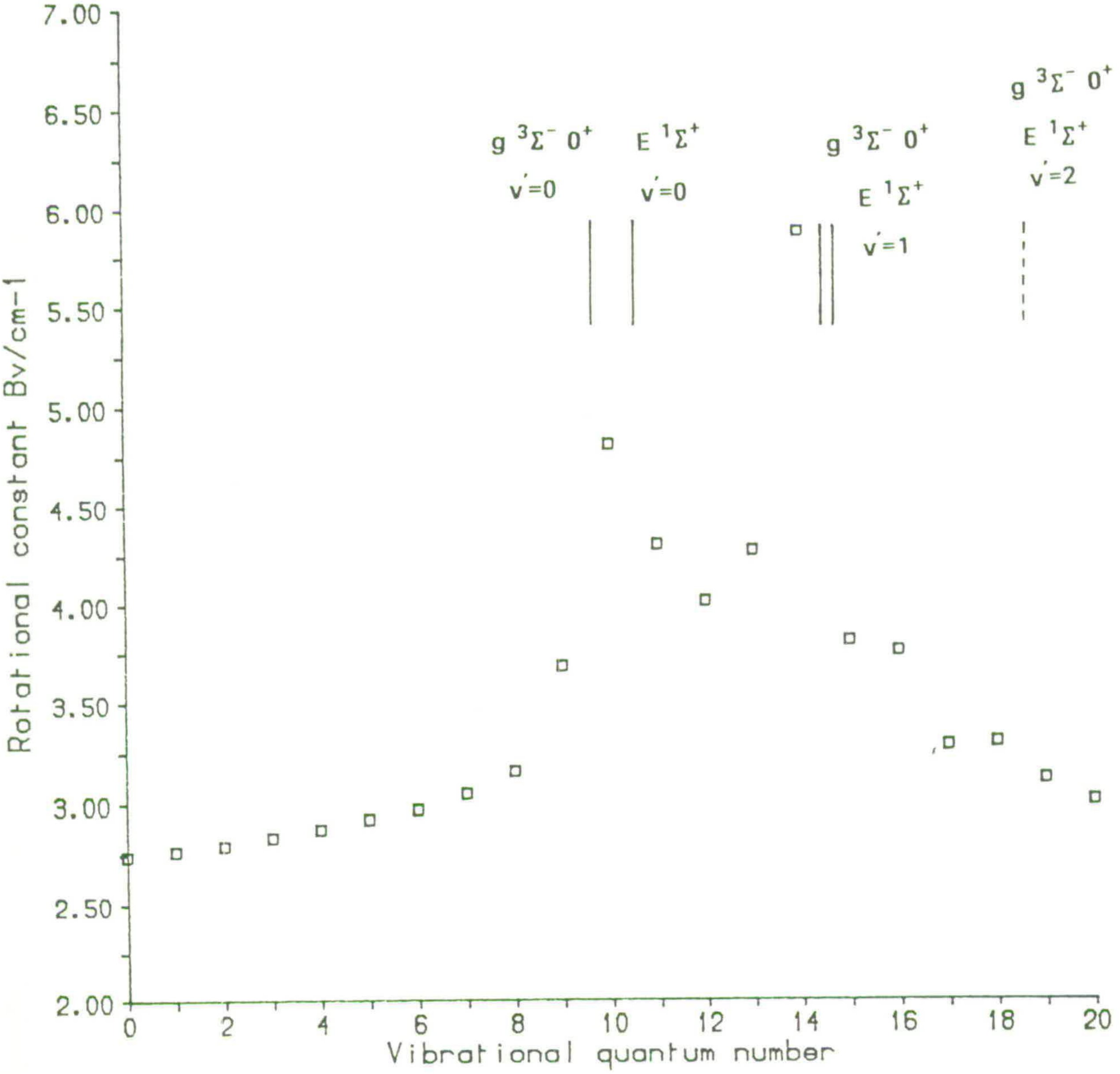

potential energy surface behaviour caused by the strong mixing between the 'Ion-pair' B $^1\Sigma^+$ state and other $^1\Sigma^+$ or (0^+) states, particularly those which have the $(5\sigma^2 2\pi^3)$ $4p\pi$ configuration close to the equilibrium internuclear separation, namely the E $^1\Sigma^+$ and g $^3\Sigma^-$ (0^+) states. Using fluorescence excitation and dispersed fluorescence spectroscopy, as will be discussed in Chapter 5, information can be derived on the nature and extent of this interstate coupling.

4.3.3 $^3\Sigma$ STATES

The effect of spin-orbit coupling [38] is most apparent in $^3\Sigma$ states. The spin-orbit coupling is sufficiently strong in HCl to cause the $^3\Sigma$ states to be approximately Hund's case (c) [21,38]. Thus the $^3\Sigma^+$ states split to 0^- and $1^\pm$ states, while the $^3\Sigma^-$ states split to 0^+ and $1^\pm$ states. In this work the Q branch rotational lines (as listed in Table 4.2) for the g $^3\Sigma^-(0^+)$ - X $^1\Sigma^+$ (0-0) transition near 83,087cm^{-1} have been observed (see Figure 4.4). There are some weak lines near 85,700cm^{-1} that may correspond to the (1-0) band but no definite transitions could be assigned. For DCl the g $^3\Sigma^-(0^+)$ - X $^1\Sigma^+$(0-0) band was also identifiable. This band was thought from VUV absorption studies to be hidden under the strong, diffuse (3-0) band of the C $^1\Pi$ - X $^1\Sigma^+$ system [28] around 83,175.8cm^{-1}. Again REMPI has only allowed detection of the longer lived excited state in this region.

Douglas and Greening [27] attribute the band in DCl at 85,131.8cm^{-1} to the v' = 1 vibrational level of the E $^1\Sigma^+$ state. However, on the basis of isotope shifts, the energy is too low by some 400cm^{-1} and it is more likely to be the v' = 1 level of the g $^3\Sigma^-(0^+)$ state. A reinvestigation of the DCl spectrum in this region is currently underway, as it is important to establish the vibrational level structure in the E $^1\Sigma^+$ state for both HCl and DCl.

The mixed 'Rydberg' - 'Ion-pair' nature of the g $^3\Sigma^-(0^+)$ state of HCl is evidenced by the rotational constants, as determined by Ginter and Ginter [29]. Vibrational levels v' = 0 and v' = 1 have B_v' values somewhat smaller than would be expected for a pure 'Rydberg' state. However, the hierarchy of perturbation is such that the E - B state interaction appears to be greater than that of the g - B state interaction.

The remainder of this chapter will be devoted to a more detailed discussion of the REMPI spectroscopy of the F $^1\Delta_2$ and the E $^1\Sigma^+$ states. Of particular interest is the comparison of the recorded line intensities with those predicted by two-photon line strength theory. The concluding section discusses the application of REMPI to the detection of HCl in a supersonic free-jet expansion.

4.4 SPECTROSCOPY OF THE F$^1\Delta_2$ RYDBERG STATE OF HCl AND DCl

In view of the extensive mixing that occurs between the B $^1\Sigma^+$ state and other $^1\Sigma^+$ or 0^+ electronic states, an understanding of the multiphoton spectroscopy of a likely unperturbed 'Rydberg' state is clearly worthwhile. A good candidate for such a study would be the F $^1\Delta_2$ state. Hence a detailed spectroscopic study of the F $^1\Delta_2$ state v' = 0, v' = 1 vibrational levels in HCl and DCl has been carried out and spectroscopic constants derived using [2+1] REMPI spectroscopy. In addition, by comparing the recorded intensities with those predicted by two-photon line strength theory then some indication of the dynamic evolution of the excited state is possible, particularly if there are significant non-radiative loss processes to compete with the final ionisation step. This is obviously also of importance if the excited state is to be used in [2+1] REMPI as a means of detecting ground state rotational distributions.

Figure 4.4 shows the 'power-normalised' [2+1] REMPI spectrum of the F $^1\Delta_2$ - X $^1\Sigma^+$ (0-0) transition, with the observed rotational transitions as indicated. The ionisation signal was normalised (as described in Chapter 3) to the square of the laser light intensity so as to account for the observed two-photon dependence, see section 4.5. As mentioned previously no isotopic splitting was resolvable indicating that it was indeed a 0-0 transition [21]. In order to make accurate spectroscopic measurement of the line positions the spectrum was recorded at high resolution, simultaneously with a wavelength calibration consisting of optogalvanic signals and etalon fringes, as described in Chapter 3.

The rotational transitions were assigned and the line positions measured in air, these were then accurately corrected to vacuum energies [45]. All this work was performed with the excimer-pumped dye laser system which had a narrower bandwidth ~0.3cm^{-1} in the UV compared to 1-1.5cm^{-1} for the Nd:YAG-pumped dye laser system.

The rotational assignments and measured positions are as tabulated in Table 1.1 in Appendix III. Their measured accuracy is ~0.20-0.25cm^{-1} depending on the 'sharpness' of the transition. In order to extract spectroscopic constants such as: T_o, the rotationless electronic transition energy, B_v, the rotational constant, D_v, the centrifugal distortion constant etc. a global least squares fit of the line position data to a fixed functional form, equation 4.2 below, for up to six unknowns was performed:

$$T_o + B_V J(J+1) - D_V J^2(J+1)^2 + \dots \qquad 4.2$$

where J is the rotational quantum number. Λ-doubling in the Δ state is assumed to be negligibly small [21,38]. The least squares fit was performed using the matrix methods discussed by P.R Bevington [47]. Inclusion of terms higher than D_v did not significantly improve the fit as the least squares analysis is limited by the accuracy of line position measurement. The ground state rotational constants for $H^{35}Cl$, $H^{37}Cl$, $D^{35}Cl$ and $D^{37}Cl$ required to use the program can be found in Bernage et al

[46]. Thus, for the F-X (0-0) transitions in HCl and DCl, the ground state $H^{35}Cl$ and $D^{35}Cl$ constants were used. In addition to the measured line positions, the calculated line positions, residuals, fitted constants T_o, B_V and D_V (cm^{-1}) with the associated standard errors and the reduced χ^2 for the fit are as shown in Table 1.1 of Appendix III. The reduced χ^2 [47], i.e. χ^2 divided by the number of degrees of freedom, effectively defines the quality of the fit to the data set (which includes measuring errors). The closer reduced χ^2 is to unity the better the fit. If the reduced χ^2 value is less than unity this implies that the measuring errors are too large.

Transitions to the F $^1\Delta_2$ v' = 0 vibrational level in DCl were treated in a similar manner and the experimental data and derived constants are tabulated in Table 1.2 of Appendix III.

The F $^1\Delta_2$ - X $^1\Sigma^+$ (1-0) transition in HCl and DCl were also studied and the results obtained are as tabulated in Tables 1.3 - 1.6 of Appendix III. The derived spectroscopic constants for all the transitions studied are shown in Table 4.3.

In the case of HCl the calculated electronic origin for the F-X (1-0) transition does not agree with that of Ginter and Ginter [29] in that they have in fact misassigned the R branch, as mentioned previously. The R(2) transition is assigned as R(1), R(3) as R(2) and so on through the branch. Analysis of the rotational

TABLE 4.3

STATE	SPECTROSCOPIC CONSTANTS/cm^{-1}
$F^1\Delta_2$ HCl v' = 0	T_o = 82,847.13 ± 0.08 B_v = 10.328 ± 0.003 D_v = 1.147 ± 0.029 x 10^{-3}
$H^{35}Cl$ v' = 1	T_o = 85,363.68 ± 0.17 B_v = 10.18 ± 0.01 D_v = 2.06 ± 0.16 x 10^{-3}
$H^{37}Cl$ v' = 1	T_o = 85,362.25 ± 0.19 B_v = 10.14 ± 0.01 D_v = 1.76 ± 0.19 x 10^{-3}
DCl v' = 0	T_o = 82,909.54 ± 0.08 B_v = 5.171 ± 0.004 D_v = 1.67 ± 0.35 x 10^{-4}
$D^{35}Cl$ v' = 1	T_o = 84,737.62 ± 0.09 B_v = 5.068 ± 0.004 D_v = 2.27 ± 0.32 x 10^{-4}
$D^{37}Cl$ v' = 1	T_o = 84,735.38 ± 0.20 B_v = 5.047 ± 0.012 D_v = 1.67 ± 1.38 x 10^{-4}

structure of the (1-0) transition in HCl revealed some interesting features. The J' = 8 level is obviously perturbed in position and intensity (see Figure 4.5) and thus was not included in the analysis. In addition transitions to rotational levels with J' > 8 could not be observed. These higher rotational levels may possibly be strongly predissociated. Spectra of the corresponding band in DCl failed to show any of the same perturbations.

An extensive search around 87,800cm^{-1} in HCl and 86,500cm^{-1} in DCl failed to reveal any conclusive evidence for a (2-0) electronic transition. The reason for this is not fully understood. The v' = 2 vibrational levels may be predissociated in both cases, or there may be poor Franck-Condon overlap with the ground state [21]. Model calculations performed with a standard Franck-Condon calculation program show that there is in fact quite a dramatic decrease in Franck-Condon overlap with the ground state on going up the vibrational levels in the F $^1\Delta_2$ state. The input data for the program were simply potential curves for the ground and excited electronic states. The ground state of HCl was modelled by a harmonic oscillator, whereas the F $^1\Delta_2$ excited state could be either a harmonic oscillator or a Morse potential [21], the choice of which had little effect on the numerical result. A constant transition dipole moment function equal to 2.00 was used, therefore a transition probability of 1.00 has a Franck-Condon factor of 4.00. Typical Franck-Condon factors are as shown below in Table 4.4.

TABLE 4.4

VIBRATIONAL LEVEL V'	FRANCK-CONDON FACTOR (V':0)
0	3.848
1	0.1134
2	0.03364
3	0.003724

The rapid decrease is obvious and this may explain why no v' = 2 level of the F $^1\Delta_2$ state could be observed.

4.5 POWER DEPENDENCE AND DETECTION SENSITIVITY MEASUREMENTS.

The dependence of the ionisation signal as a function of laser intensity (power) was determined for several rotational lines in the F $^1\Delta_2$ - X $^1\Sigma^+$ (0-0) transition. Figure 4.11 shows the two-photon dependence of the ionisation signal resulting from excitation of the R(1) rotational line. Laser pulse energies were in the range ~30 - 400μJ which corresponded to, knowing a focussed beam radius of ~90μ and pulse width of ~10ns, photon fluences in the range 1.4 x 10^{25} - 1.9 x 10^{26}

FIGURE 4.11 Ionisation signal power dependence.

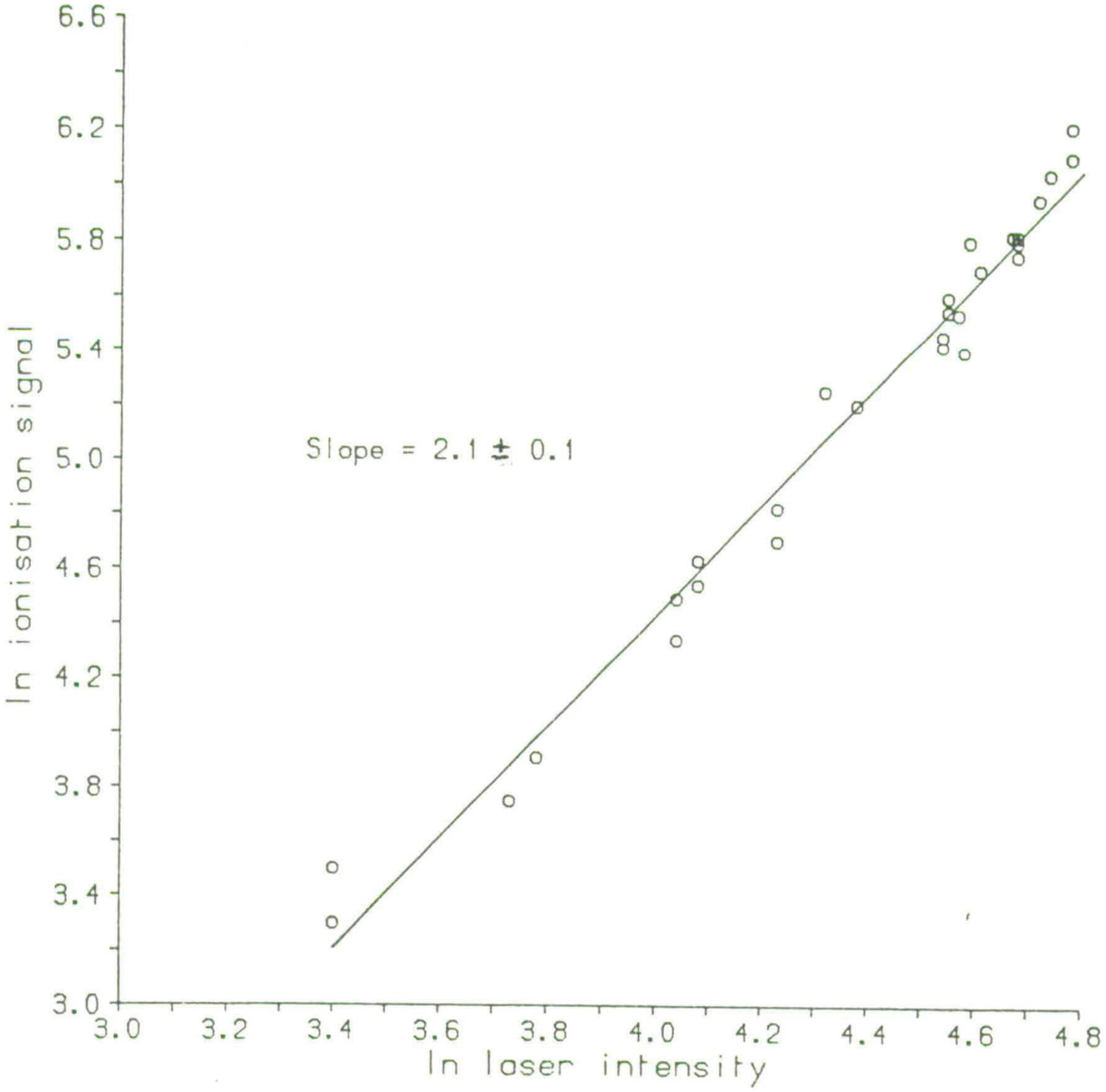

photons $cm^{-2}s^{-1}$. Other rotational lines showed slightly different dependencies, though all were about 2. Thus at the power levels used, the ionisation step was likely to be close to or at 'kinetic saturation', with two-photon excitation of the resonant step being the rate determining process. Using the kinetic model of multiphoton ionisation suggested by Zakheim and Johnson [48] the ion yields can be crudely predicted under a variety of conditions, as has been discussed in Chapter 2. Figure 4.12 shows the calculated ion yield as a function of laser pulse energy, using equation 2.10 in Chapter 2, with the following parameters:

Laser pulse intensity, $I = 1.5 \times 10^{25} - 1.5 \times 10^{27}$ photons $cm^{-2}s^{-1}$.
Excited state radiationless transition rate, $\delta = 1s^{-1}$.
Excited state radiative decay rate, $\gamma = 2 \times 10^{8}s^{-1}$.
Laser pulse width = 10ns.
Single-photon ionisation cross-section $\sigma_{II} = 10^{-18}cm^{2}$.
Different two-photon cross-sections $\sigma_{I} = 10^{-45}, 10^{-48}$ and $10^{-50}cm^{4}s$.
Gas concentration (pressure) $X_{o} = 10^{16}$ molecules cm^{-3}.

It would seem that over the energy range of the power dependence measurement a two-photon power dependence of the ionisation signal is not an unreasonable assumption, with saturation of the ionisation step present except at very low powers. Note

FIGURE 4.12 Calculated ion yield as a function of laser pulse energy at different two-photon cross-sections.

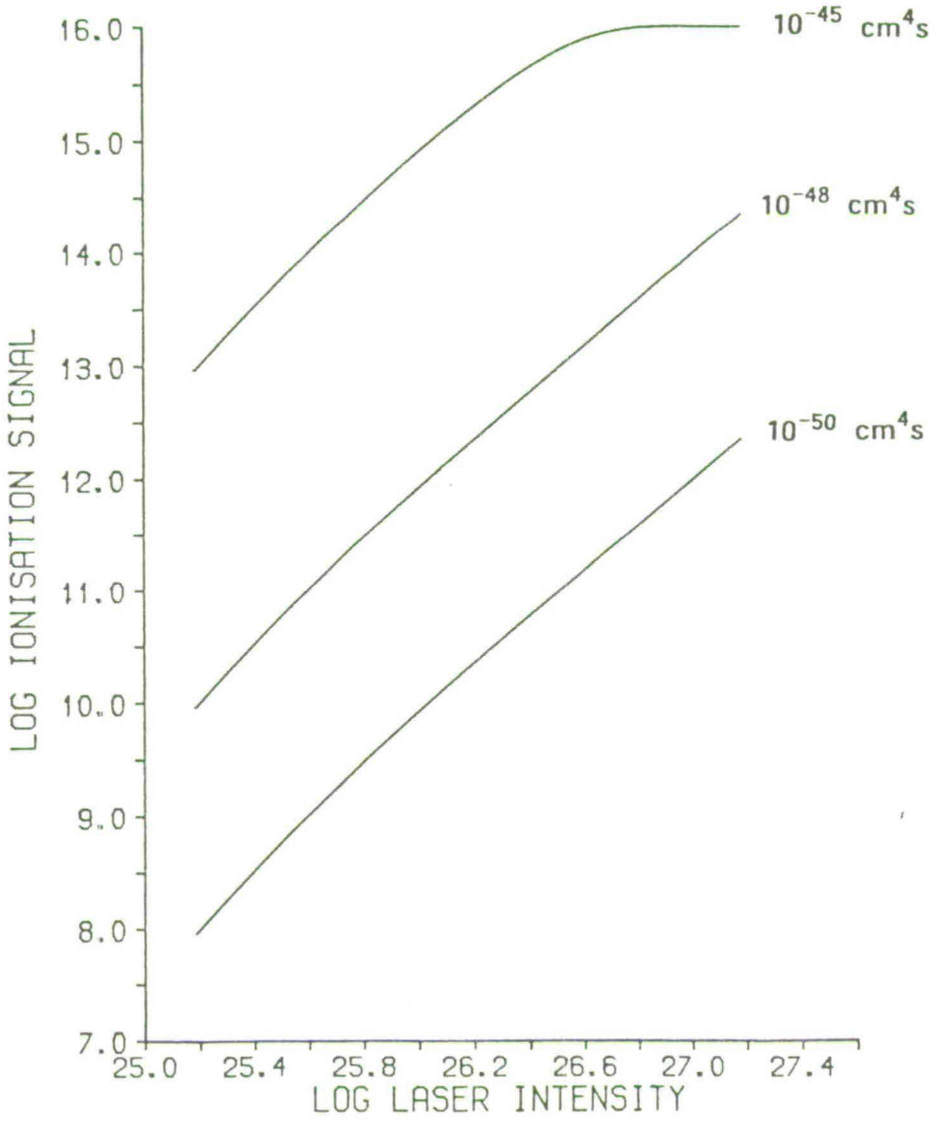

that the model predicts at highest pulse energies and highest two-photon cross-section, 10^{-45} $cm^4 s$, every molecule is effectively ionised. Figure 4.13 shows the predicted variation of the ion signal as a function of the radiationless transition rate, at a constant two-photon cross-section ($10^{-48} cm^4 s$). Even fast radiationless decay rates, by this model, give significant ion yields, when experimentally little or no REMPI current might be expected. As Zakheim and Johnson [48] point out their model may not predict excited state ionisation behaviour very well when there are very rapid $>10^{12} s^{-1}$ non-radiative decay rates. As a cautionary note recent work by Zare et al [42,49,50] and Dixit and McKoy [51] suggest that ion yields in REMPI experiments depend critically on saturation and intermediate state alignment effects. Alignment of the resonant intermediate excited state arises from the polarised nature of the exciting laser light. This causes preferential excitation of those molecules having larger projections of the transition dipole moment on the electric field vector of the linearly polarised light beam. Zare et al [49] point out that the degree of saturation of a REMPI current can vary from line to line and, remarkably, even across a line profile!

Using 300 μJ laser pulse energies the sensitivity for HCl detection, using REMPI via the $F^1\Delta_2 - X\ ^1\Sigma^+$ (0-0) transition, for a signal-to-noise ratio of 10:1 was 10^{13} molecules cm^{-3} per single rotational quantum state.

FIGURE 4.13 Predicted variation of the ion signal as a function of the radiationless transition rate, at a constant two-photon cross-section (10^{-48} cm^{4}s).

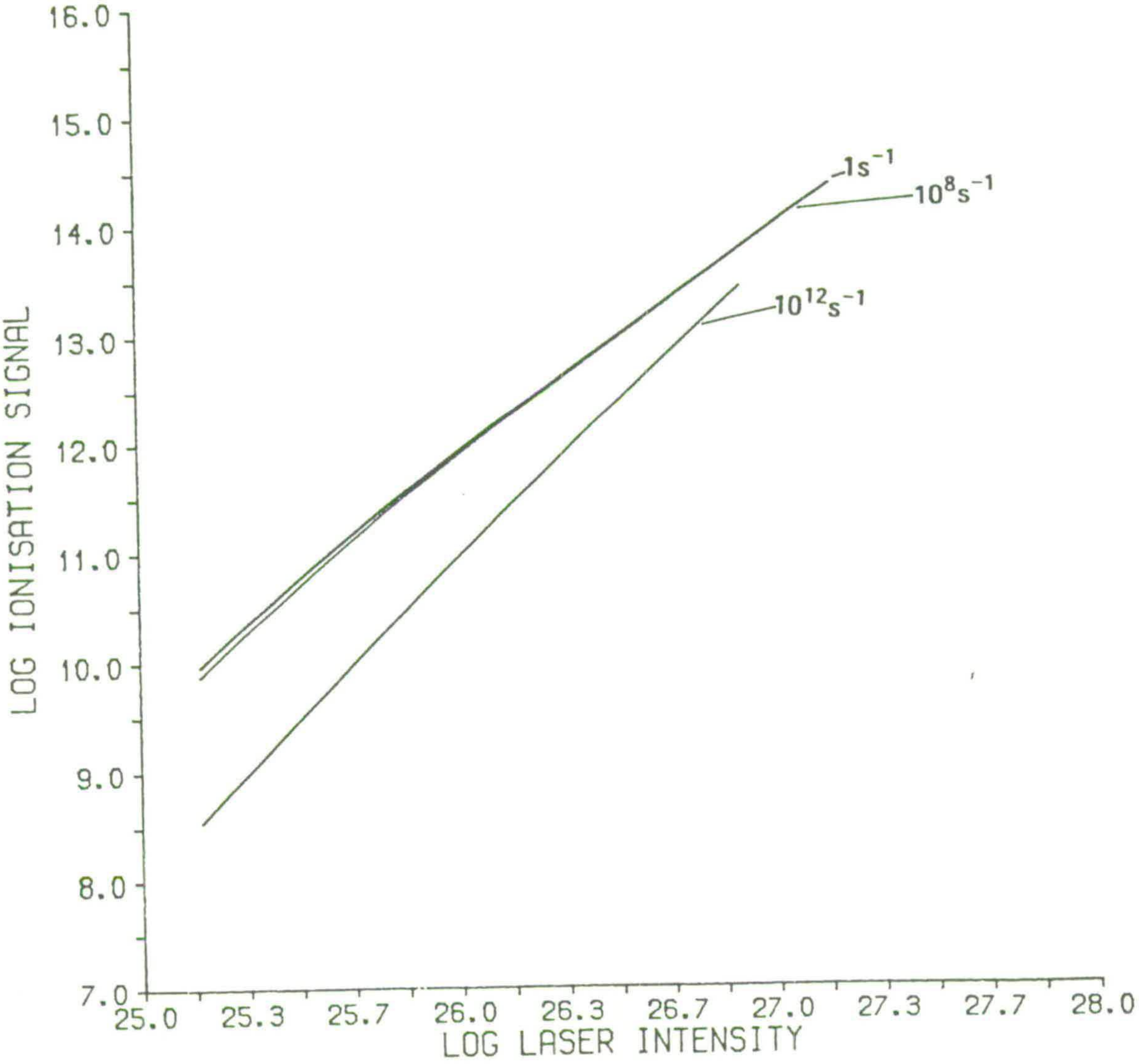

The REMPI signal increased linearly with pressure over the range 10^{-3} - 1.00 Torr (0.133-133.3Nm^{-2}). Thus for a signal-to-noise ratio of 1:1 a detection sensitivity per single rotational quantum state of $\sim 10^{12}$ molecules cm^{-3} might be expected. Sensitivities of this magnitude are about the same as those recently determined for other diatomic molecules, i.e. H_2 [52] and N_2 [53,54] using REMPI spectroscopy with parallel-plate ion collection. With an electron multiplier instead of parallel plates as ion detectors, one could safely predict a detection sensitivity of 10^8-10^9 molecules cm^{-3}.

4.6 SIMULATION OF THE F $^1\Delta_2$ - X $^1\Sigma^+$ TWO-PHOTON TRANSITION.

The structure displayed in a [2+1] REMPI spectrum is generally controlled by the initial, rate limiting, two-photon excitation step and thus can be understood in terms of the appropriate two-photon rotational line strength theory. Bray and Hochstrasser [43] and Zare et al [42] from a more general perspective have both derived 'easy-to-use' formulae for two-photon transition line strengths with linearly or circularly polarised laser light in terms of ground electronic state orbital angular momentum Λ and rotational angular momentum J values. Using their formalism [42,43] the structure of a Δ - Σ two-photon transition is as shown in Figure 4.14. The π state is the virtual intermediate state and $\mu_\perp$, $\mu_\perp'$ are the one-photon transition moments. Assuming that the

FIGURE 4.14 The structure of $^1\Delta - {}^1\Sigma^+$ two-photon transition.

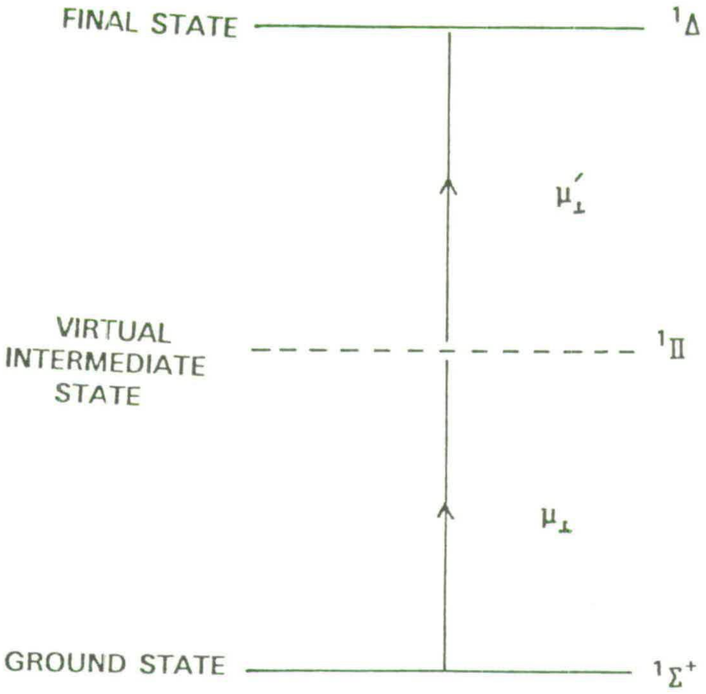

distribution of ground state angular momenta is isotropic (i.e. there is no alignment or preferential directionality of J) and the cross-section for the absorption of the third (ionising) photon is independent of wavelength then the relative strength of individual rotational lines for two-photon absorption transitions can be calculated from equation 2.8 (Chapter 2) ie:

$$I = CS_{J'J''}\exp(-E_{ROT}/kT) \qquad 4.3$$

where $\exp(-E_{ROT}/kT)$ is the Boltzmann factor, k is Boltzmann's constant and T the temperature in Kelvin. $S_{J'J''}$ is the two-photon rotational line strength for linearly polarised light and C is the transition dipole factor $|\mu_{\pm}\mu'_{\pm}|^2$ which is a constant independent of the rotational transition. The subscripts on μ refer to the change in Λ for the single-photon transition and the primes refer to the different pathways, see Figure 4.14.

Using the two-photon line strengths, a temperature of 293 K, a Gaussian laser band-width of 0.30 cm^{-1} and the relevant lower and upper state rotational constants the F $^1\Delta_2$ - X $^1\Sigma^+$ (0-0) spectrum can be simulated, as shown in Figure 4.15 (b). The Fortran program written for this and simulation of $^1\Sigma^+$ - $^1\Sigma^+$ two-photon transitions is to be found in Appendix IV.

The simulated spectrum does not compare well with that obtained experimentally with the intensity at high J being less than that theoretically predicted (see Figure

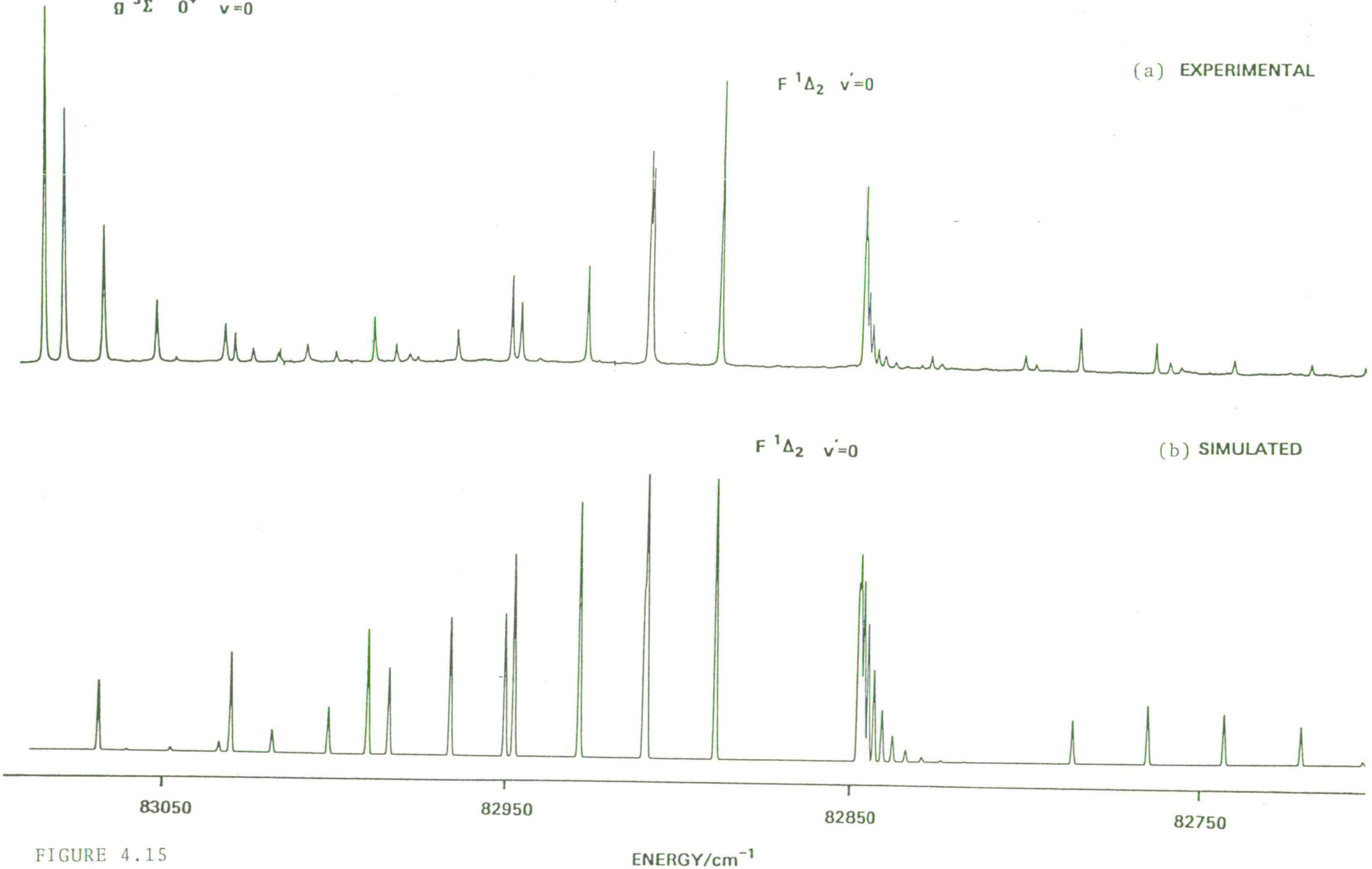
$g\ ^3\Sigma^-\ 0^+\ v=0$
(a) EXPERIMENTAL
$F\ ^1\Delta_2\ \ v'=0$
$F\ ^1\Delta_2\ \ v'=0$
(b) SIMULATED
83050
82950
82850
82750
ENERGY/cm^{-1}

FIGURE 4.15

4.15 (a)). Ionisation as a means of detection in the REMPI experiment is essentially an immediate probe of the dynamics of the prepared resonant excited state since it operates in the same time domain as predissociation and even fluorescence. Thus, predissociation of the intermediate state represents [55,56] one potentially competitive process likely to reduce the observed ion yield (ϕ) from that (ϕ_o) expected in the absence of predissociation. The observed spectral line heights (h) will be reduced from their values (h_o) predicted by two-photon rotational line strength theory, while the line-widths (w) ought to show a proportional increase as a consequence of the decreased excited state lifetime. Predissociation can be regarded as occurring by two mechanisms. One homogeneous, which affects all excited state rotational levels equally. There will however be some oscillatory dependence of the predissociation rate on the vibrational quantum levels. The second, heterogeneous predissociation ($\Delta\Omega = \pm 1$), is presumed to possess a rate proportional to some varying content of the excited state rotational energy (angular momentum). The strength of the ionisation signal detected on resonance depends on the quantum yield for ionisation ϕ for each level as well as the line strength factor and the initial state population. The rate constant for ionisation k_I is deemed to be independent of laser wavelength. ϕ is therefore the ratio of k_I to the total rate constant k_T for decay of the resonant intermediate level:

$$\phi = k_I/k_T \qquad 4.4$$

where

$$k_T = k_I + k_F + k_D \qquad 4.5$$

here k_F is the fluorescence decay rate constant and k_D is the predissociation rate constant.

If the F $^1\Delta_2$ state is predissociated in a heterogenous manner ($\Delta\Omega=\pm1$) then the predissociative decay rate [57] can be expressed as:

$$k_D = k'J(J+1) \qquad 4.6$$

hence, $\phi = k_I/\{k_I+k_F+k'J(J+1)\}$ 4.7

when $J = 0$ then,

$$\phi_o = k_I/k_I+k_F \qquad 4.8$$

Hence,

$$\phi = \phi_o/\{1+cJ(J+1)\} \qquad 4.9$$

where $c = k'/k_I+k_F)$

or $\phi = \phi_o/F$, where F is a damping function

$$F = (1+cJ(J+1)) \qquad 4.10$$

Now the spectral line height h is given by $\phi h_o/F = \phi_o h_o/F^2$, therefore the peak heights scale proportionally to $^1/F^2$. The line-width of any transition determined by the population loss from the excited state will have contributions from 'up-pumping' to the ionisation continuum, homogeneous predissociation, rotational level dependent predissociation, and fluorescence. The power dependences of the transition profiles were checked to ensure that power broadening effects discussed in Chapter 2 made minimal contribution to the line-widths in the MPI spectrum. Thus any line-width contributions due to this or to fluorescence are likely to be negligible. Any significant line broadening will be due to the effects of predissociation. These must then be combined with a Gaussian line-shape function, typically of 0.30cm^{-1} f.w.h.m., to allow for those factors limiting the ultimate experimental resolution. In this work the line-widths appeared to be determined by the laser bandwidth.

Figure 4.16(b) shows the spectrum obtained by including the damping function F with c set to 0.05. Although the fit with experiment, Figure 4.16(a), is still not perfect it does illustrate the likely existence of some heterogenous rotational level dependent predissociation mechanism. Figure 4.17(a) shows the Q branch of the $F\ ^1\Delta_2 - X\ ^1\Sigma^+$ transition as determined experimentally. The simulated spectrum is shown in Figure 4.17(b), it uses the damping function mentioned above. Note that the Q(7) and Q(8) transitions are obscured by the Q(0) line for $H^{35}Cl$ and $H^{37}Cl$, respectively, of the $B\ ^1\Sigma^+ - X\ ^1\Sigma^+$ (9-0) transition.

It is likely that the predissociation is occurring heterogeneously via the diffuse $C\ ^1\pi$ state. Vibrational level v' = 2 of this state is known to lie near-by at

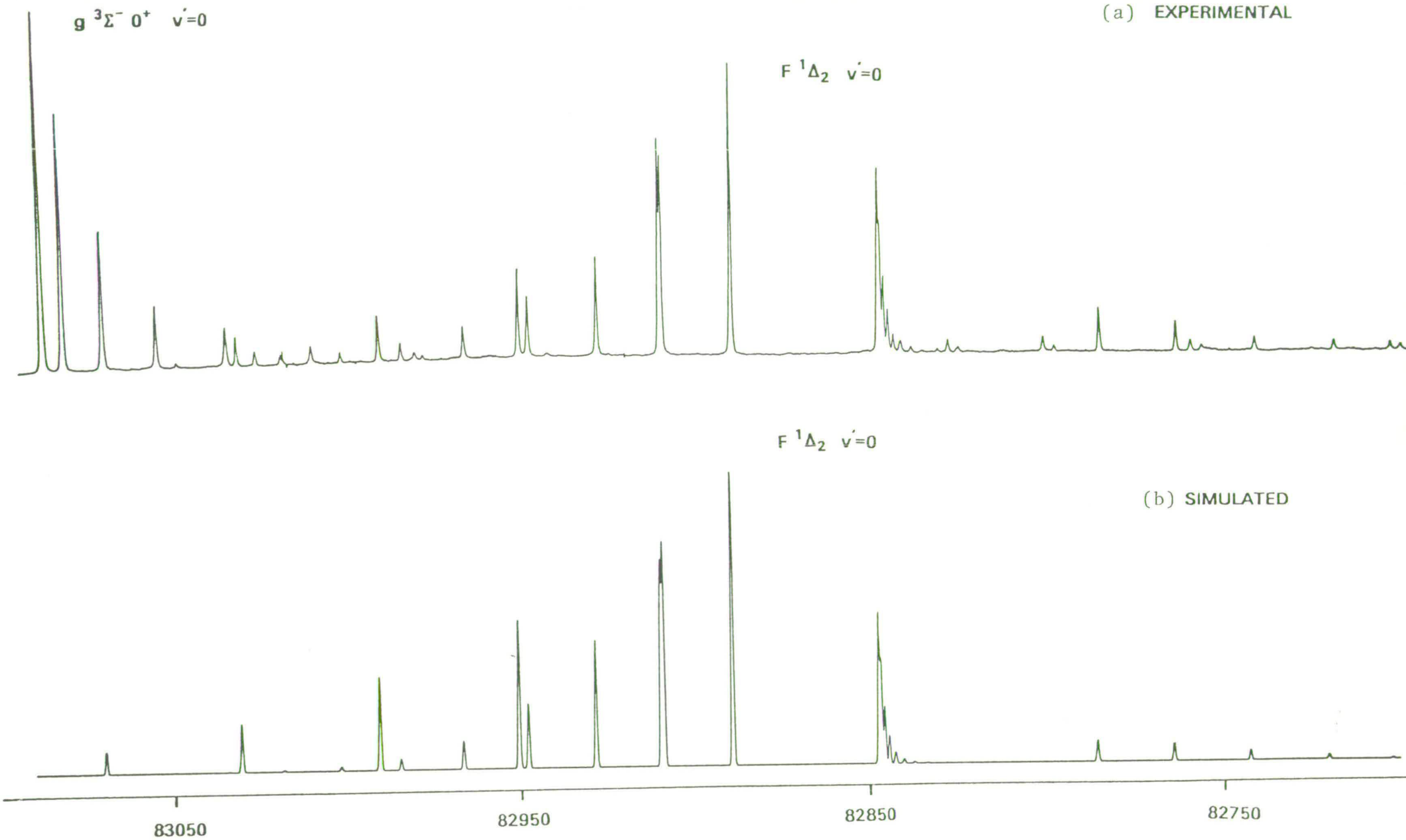
g $^3\Sigma^-$ 0^+ v′=0
(a) EXPERIMENTAL
F $^1\Delta_2$ v′=0
F $^1\Delta_2$ v′=0
(b) SIMULATED
83050
82950
82850
82750

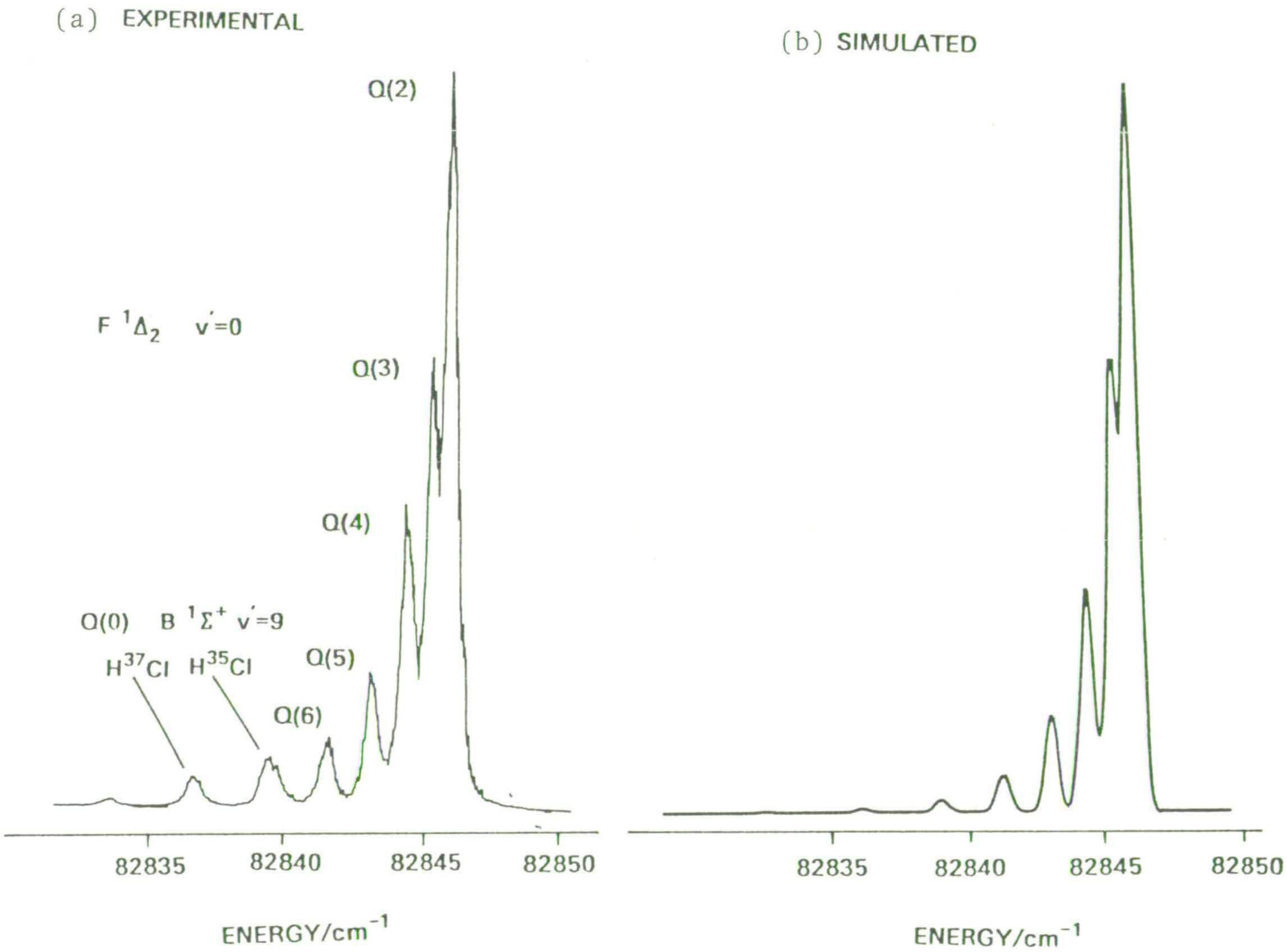

FIGURE 4.17 Q branch of the F $^1\Delta_2$ — X $^1\Sigma^+$ (0 — 0) REMPI spectrum.

82,725cm^{-1} and this may provide a doorway to the $^3\Sigma^+$ continuum state.

In conclusion, it would appear that the F $^1\Delta_2$ state is not as unperturbed as the spectroscopic data might suggest initially and its use as a resonant state in REMPI detection of ground state rotational distributions must be questioned, because the intensities predicted theoretically are not as observed experimentally.

4.6.1 SIMULATION OF THE E $^1\Sigma^+$ - X $^1\Sigma^+$ TWO-PHOTON TRANSITION.

Figure 4.18(a) shows the power-normalised [2+1] REMPI spectrum of HCl via the E $^1\Sigma^+$ v' = 0 state. The spectrum was normalised to a two-photon power dependence, which had been checked for several rotational lines of the transition. The line strength formulae required to simulate the $^1\Sigma^+$ - $^1\Sigma^+$ transition include terms of two independent transition dipole moments μ_S and μ_I, which are as defined in references [42] and [43]. The absolute values of μ_I^2 and μ_S^2 are not required for the simulation, only their ratio. Hence, an estimate of μ_I^2/μ_S^2 can be determined by measuring the intensities of the Q and S branch lines from the same ground state J level. A typical value is ~1.5, however the calculated intensities do not depend strongly on μ_I^2/μ_S^2. Alternatively, the relative values of μ_I^2 and μ_S^2 can be estimated by comparing the intensities of a Q branch line excited alternatively by linearly and circularly polarised

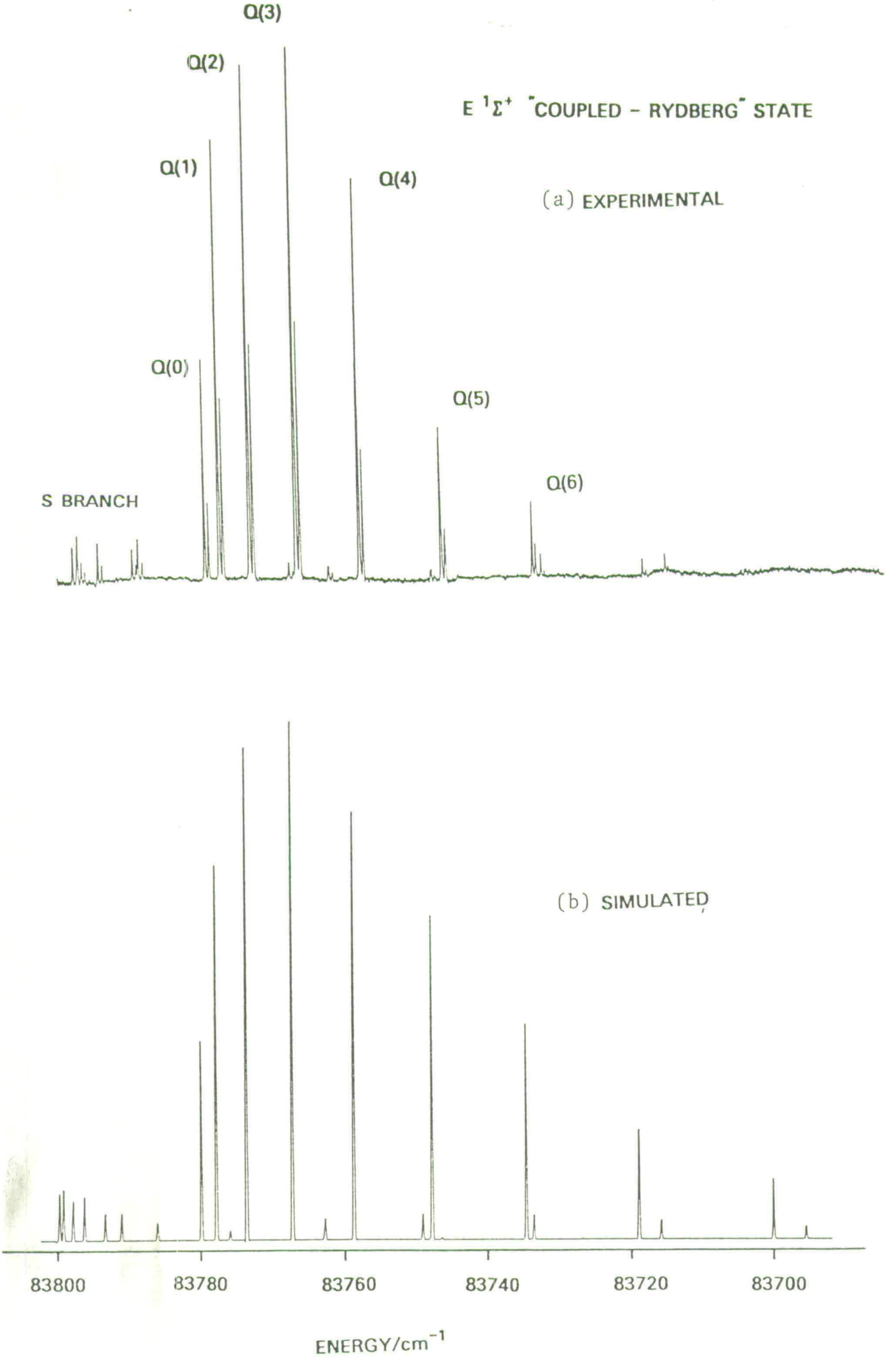
Q(3)
Q(2)
E $^1\Sigma^+$ "COUPLED - RYDBERG" STATE
Q(1)
Q(4)
(a) EXPERIMENTAL
Q(0)
Q(5)
Q(6)
S BRANCH
(b) SIMULATED
83800
83780
83760
83740
83720
83700
ENERGY/cm^{-1}

FIGURE 4.18

radiation. However, this requires the use of a Fresnel rhomb for transforming from linear to circular polarisation. The simulated spectrum of the E $^1\Sigma^+$ - X $^1\Sigma^+$ (0-0) transition for $H^{35}Cl$ is as shown in Figure 4.18(b). A temperature of 293K and a laser bandwidth of $0.30cm^{-1}$ is assumed. Comparison with the experimental spectrum shows that the intensity predicted for high J' levels is not matched experimentally. This may not be that surprising in view of the 'mixed' nature of this excited state. An attempted modelling by a rotational level dependent predissociation could not account for the observed phenomena. The rapid decline of the experimental intensities with increasing J' is even more dramatic in the E $^1\Sigma^+$ - X $^1\Sigma^+$ (1-0) transition where the rotational lines end abruptly at Q(5). This behaviour is quite anomalous and not well understood. Recent work performed by Parker et al [37] on the same state using REMPI techniques have shown exactly similar behaviour.

This reduction in line intensity at high J could again be due to a predissociative loss. If this predissociation is indirect through a diffuse 'doorway' state then the energy mismatch between each v, J level of the two states is crucial. This will change with J, with levels coming into and then going-off resonance. In this case high J levels of the E state may be at closer resonance with diffuse levels of a 'doorway' state than the lower J levels.

4.7 [2+1] REMPI SPECTROSCOPY OF HCl IN A SUPERSONIC FREE JET EXPANSION.

4.7.1 INTRODUCTION

Supersonic molecular beams or supersonic free jet expansions have been used for some time now to prepare gas phase samples for spectroscopic study under conditions where the internal degrees of freedom, the molecular vibration and rotation have been cooled to very low temperatures [58]. In molecules such as HCl which have a large number of excited electronic states, spectral congestion can be relieved using cooling during a supersonic expansion. In a supersonic expansion the molecule of interest, either neat or in a carrier gas is expanded through a small orifice or nozzle. The expansion cools the translational degrees of freedom and in the post-nozzle region of the expansion the cold translational bath acts as a refrigerant for the other degrees of freedom. As the expansion proceeds, the density of gas drops and eventually becomes too low to provide the collisions necessary to connect the translational bath with the internal degrees of freedom. Those degrees of freedom that equilibrate most rapidly with the translational bath are coldest at the point where the expansion runs out of collisions. The term 'supersonic' derives from the marked decline in the local speed of sound ($\alpha T^{\frac{1}{2}}$) due to the expansion cooling. Hence a typical molecular velocity of 1000ms^{-1} can correspond to Mach numbers of greater than 100 by the time the molecules reach the collision-free region.

One of the most important applications of supersonic jet spectroscopy has been to probe the properties of van der Waals molecules. A supersonic expansion allows the preparation of a low temperature environment where the most probable relative kinetic energy in a binary collision is very much less than van der Waals binding energies. Once formed the van der Waals molecules are stable with respect to collisions with the surrounding gas as well as having spectral simplification by de-population of excited rotational and vibrational states.

The Ar...HCl van der Waals molecule has been extensively studied in its ground electronic state and its potential energy surface is well understood [59]. REMPI is now an established technique for studying electronically excited van der Waals molecules [60]. To date no data exists on the electronically excited Ar...HCl van der Waals molecule. Its detection and characterisation would be a very exciting development.

4.7.2 RESULTS

Some preliminary experiments have been performed on [2+1] REMPI of HCl in a supersonic free jet expansion of Ar/HCl mixtures, using the apparatus described in Chapter 3. The HCl concentration in Ar varied between 0.5 and 5% and a total backing pressure of 0.5-2 atm

($5.066x10^4$-$2.0265x10^5 Nm^{-2}$) was used. Most experiments were performed with the Quantel Datachrom-5000 laser system because of its higher pulse energy in the UV (see Chapter 3).

Figure 4.19(a) shows the spectrum of the F $^1\Delta_2$, v' = 0 and B $^1\Sigma^+$, v' = 9 levels under jet-cooled conditions, 0.5 atm ($5.066x10^4 Nm^{-2}$) backing pressure and 5% HCl in Ar were used. The rotational cooling is obvious as the rotational population has relaxed effectively into low rotational levels. Note the weak Q branch of the F $^1\Delta_2$ state in comparison with the room temperature spectrum. Simulation of the spectrum, assuming a Boltzmann distribution, suggests a typical rotational temperature of ~20K. Rotational temperatures of less than 5K could easily be obtained by increasing the backing pressure to 1 atm or by reducing the concentration of HCl in the expansion mixture (see Figure 4.19(b)). These experiments show conclusively that HCl can be detected with high sensitivity in supersonic expansions of Ar/HCl mixtures. Extensive searches for excited Ar...HCl van der Waals satellite bands close to the B $^1\Sigma^+$ v' = 9,10,11 levels, the g $^3\Sigma^-(0^+)$ v' = 0 level, the E $^1\Sigma^+$ v' = 0 level and the F $^1\Delta_2$ v' = 0 level proved unsuccessful. However, with the comparatively simple free jet apparatus used, it was difficult to be conclusive about this result. With mass resolved detection, i.e. in a time-of- flight mass spectrometer it ought to be possible to prove whether or not electronically excited Ar...HCl complexes are sufficiently stable to be studied using REMPI techniques.

FIGURE 4.19 REMPI spectra of HCl under supersonic jet-cooled conditions.

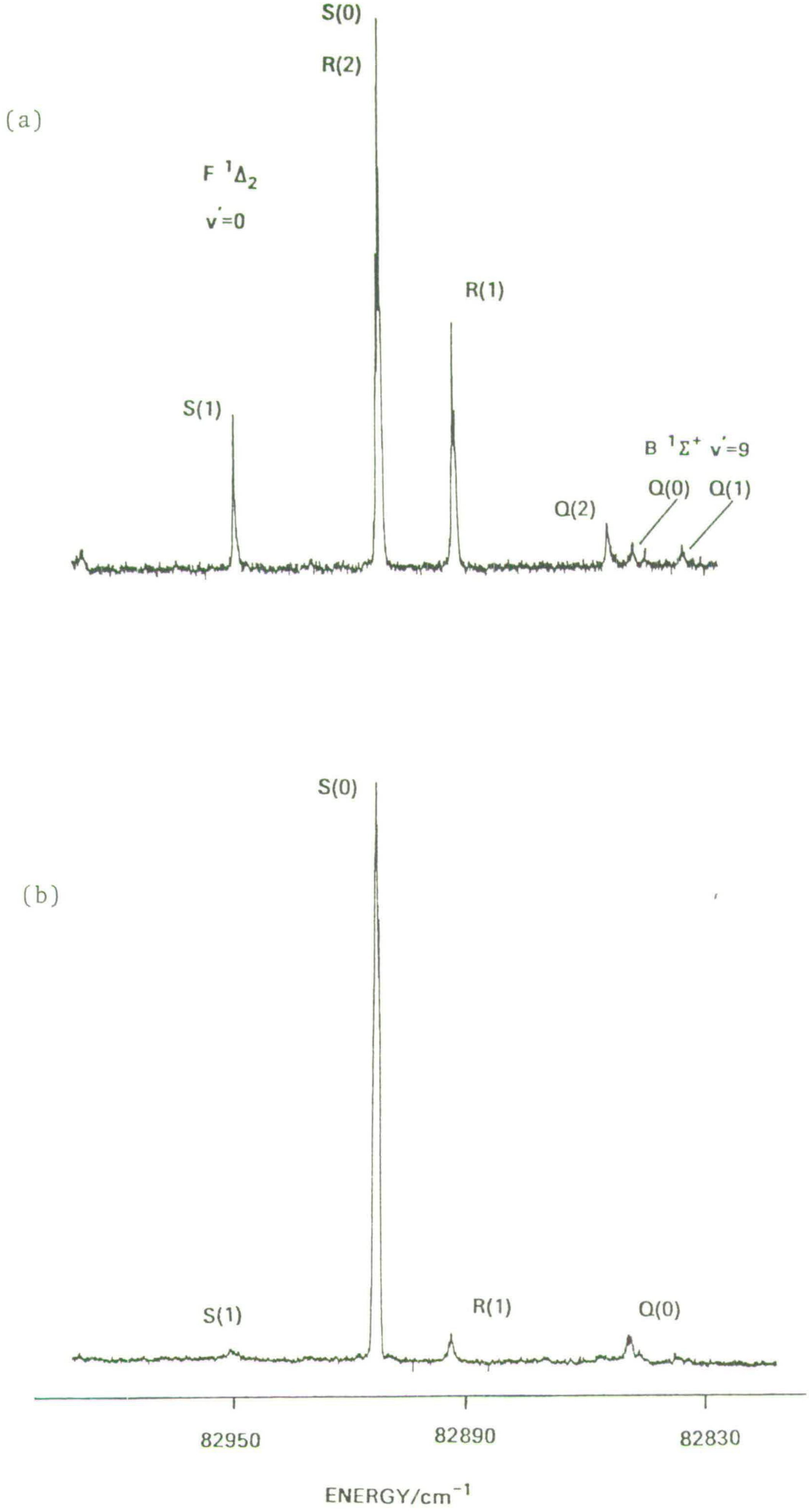

4.8 REFERENCES

1. Y.L. Yung and W.B. DeMore, ICARUS 51, 199 (1982).
2. M. Jura, Astrophys. J. Lett., 190, L33 (1974).
3. A. Dalgarno, T. deLong, M. Oppenheimer and J.H. Black, Astrophys. J. Lett., 192, L37 (1974).
4. M.R. Levy, Progr. Reaction Kinetics., 10, 1 (1979).
5. M.C. Lin, M.E. Unstead and N. Djeu, Ann. Rev. Phys. Chem., 34, 557 (1983).
6. K.G. Anlauf, P.J. Kuntz, D.H. Maylotte, P.D. Pacey and J.C. Polanyi, Discuss. Faraday, Soc., 44, 183 (1967).
7. E.E. Marinero, C.T. Rettner and R.N. Zare, J. Chem. Phys., 80, 4142 (1984).
8. C.T. Rettner, F. Fabre, J. Kimman and D.J. Auerbach, Phys. Rev. Lett., 55, 1904 (1985).
9. G.D. Kubiak, G.O. Sitz and R.N. Zare, J. Chem. Phys., 83, 2538 (1985).
10. D.W. Chandler and R.L. Farrow, J. Chem. Phys., 85, 810 (1986).
11. K. Kimura, Adv. Chem. Phys., 60, 161 (1985).
12. M. Bettendorf, S.D. Peyerimhoff and R.J. Buenker, Chem. Phys., 66, 261 (1982).
13. W.J. Stevens and M. Krauss, J. Chem. Phys., 77, 1368 (1982).
14. D.M. Hirst and M.F. Guest, Mol. Phys. 41, 1483

(1980).

15. E.F. van Dishoeck, M.C. van Hemert and A. Dalgarno, J. Chem. Phys., 77, 3693 (1982).
16. P.J. Bruna and S.D. Peyerimhoff in 'Ab-initio Quantum Chemistry, Vol. 1', edited by K.P. Lawley (Wiley, New York, 1986).
17. H. Lefebvre-Brion and R.W. Field in 'Perturbations in the Spectra of Diatomic Molecules', (Academic Press, 1986).
18. L. Pauling, J. Amer. Chem. soc., 54, 988 (1932).
19. R.S. Mulliken, Phys. Rev., 50, 1017 (1936).
20. S.G. Tilford and M.L. Ginter, J. Mol. Spectrosc., 40, 568 (1971).
21. G. Herzberg in 'Molecular Spectra and Molecular Structure, Vol. I - Spectra of Diatomic Molecules', 2nd Edition, (D. Van Nostrand Company, Princeton, 1950).
22. K. Dressler, R. Gallusser, P. Quadrelli and L. Wolneiwicz, J. Mol. Spectrosc., 75, 205 (1979).
23. S.D. Peyerimhoff, private communication, 1986.
24. M. Bettendorff, R.J. Buenker, S.D. Peyerimhoff and J. Römelt, Z. Phys., A., 304, 125 (1982).
25. J. Romand, Ann. Phys., 4, 528 (1949).
26. J.K. Jacques and R.F. Barrow, Proc. Phys. Soc. London, 73, 538 (1958).
27. A.E. Douglas and F.R. Greening, Can. J. Phys., 57, 1650 (1979).
28. S.G. Tilford, M.L. Ginter and J.T. Vanderslice, J.

Mol. Spectrosc., 33, 505 (1970).

29. D.S. Ginter and M.L. Ginter, J. Mol. Spectrosc., 90, 177 (1981).

30. J.A. Coxon and U.K. Roychowdhury, Can. J. Phys., 63, 1485 (1985).

31. R. Rydberg, Z. Phys., 73, 376 (1931).

32. O. Klein, Z. Phys., 76, 226 (1932).

33. A.L.G. Rees, Proc. Phys. Soc., 59, 998 (1947).

34. J. Tellinghuisen, Adv. Chem. Phys., 60, 299 (1985).

35. S. Arepalli, N. Presser, D. Robie and R.J. Gordon, Chem. Phys. Lett., 118, 88 (1985).

36. R. Callaghan, S. Arepalli and R.J. Gordon, J. Chem. Phys., 86, 5273 (1987).

37. T.A. Spiglanin, D.W. Chandler and D.H. Parker, Chem. Phys. Lett., 137, 414 (1987).

38. I. Kovács in 'Rotational Structure in the Spectra of Diatomic Molecules', (the Institute of Physics, Bristol, 1969).

39. C.A. Mayhew, J.P. Connerade, M.A. Baig, M.N.R. Ashfold, J.M. Bayley, R.N. Dixon and J.D. Prince, J. Chem. Soc. Faraday Trans. 2, 83, 417 (1987).

40. P.L. Smith, K. Yoshino, J.H. Black and W.H. Parkinson, Astrophys. J., 238, 874 (1980).

41. J.B. Nee, M. Suto and L.C. Lee, J. Chem. Phys., 85, 719 (1986).

42. A.C. Kummel, G.O. Sitz and R.N. Zare, J. Chem. Phys., 85, 6874 (1986).

43. R.G. Bray and R.M. Hochstrasser, Mol. Phys., 31,

1199 (1976).

44. S.V. Filseth, R. Wallenstein and H. Zacharias, Opt. Commun., 23, 231 (1977).

45. CRC 'Handbook of Chemistry and Physics', 55th Edition, (1974-75), edited by R.C. Weast (CRC Press, Ohio U.S.A.).

46. G. Guelachvili, P. Niay and P. Bernage, J. Mol. Spectrosc., 85, 271 (1981).

47. P.R. Bevington in 'Data reduction and Error Analysis for the Physical Sciences', (New York, 1969).

48. D.S. Zakheim and P.M. Johnson, Chem. Phys., 46, 263 (1980).

49. D.C. Jacobs and R.N. Zare, J. Chem. Phys., 85, 5457 (1986).

50. D.C. Jacobs, R.J. Madix and R.N. Zare, J. Chem. Phys., 85 5469 (1986).

51. S.N. Dixit and V. McKoy, J. Chem. Phys., 82, 3546 (1985).

52. E.E. Marinero, C.T. Rettner and R.N. Zare, Phys. Rev. Lett., 48, 1323 (1982).

53. A.E. Bruno, U. Schubert, H.J. Neusser and E.W. Schlag, Chem. Phys. Lett., 131, 31 (1986).

54. K.L. Carleton, K.H. Welge and S.R. Leone, Chem. Phys. Lett., 115, 492 (1985).

55. M.N.R. Ashfold, J.M. Bayley and R.N. Dixon, Can. J. Phys., 62, 1806 (1984).

56. M.N.R. Ashfold, R.N. Dixon, K.N. Rosser, R.J. Stickland and C.M. Western, Chem. Phys., 101, 467

(1986).

57. J. Tellinghuisen, J. Chem. Phys., 57, 2397 (1972).

58. D.H. Levy, Ann. Rev. Phys. Chem., 31, 197 (1980).

59. J.M. Hutson and B.J. Howard, Mol. Phys., 45, 769 (1982).

60. K. Sato, Y. Achiba and K. Kimura, J. Chem. Phys., 81, 57 (1984).

CHAPTER 5

FLUORESCENCE SPECTROSCOPY OF ELECTRONICALLY EXCITED HCl

5.1 INTRODUCTION

Fluorescence spectroscopy of excited electronic states lying in the vacuum ultra-violet (VUV) energy region can be performed by a variety of techniques. Using tunable synchrotron radiation (typical bandwidth ~ 0.1nm) several diatomic molecules including HCl and HBr have been made to fluoresce [1-3]. Tunable, coherent laser radiation in the VUV, produced by frequency up-conversion techniques, can also be used to excite molecular fluorescence. Progress in the production of tunable VUV laser sources in the wavelength region 130nm down to 70nm makes efficient single-photon excitation of molecules such as H_2 possible [4]. Generally tunable radiation of this wavelength can be produced by frequency tripling in rare gases the output of a frequency-doubled dye laser pumped by a Nd:YAG laser. Electronic states lying in the wavelength region 130-180nm can be conveniently accessed using coherent radiation generated by four-wave sum-frequency mixing techniques [5]. For wavelengths between 180nm and 200nm Raman shifting by H_2 of the radiation from a frequency doubled dye laser is the most commonly used technique [6].

An alternative approach to studying high lying electronic states is to use laser multiphoton techniques. Direct two-photon fluorescence excitation spectra of various diatomic molecules with excited electronic states at VUV energies have been recorded [7-9]. The requisite wavelengths in the 190-300nm region can be produced by three main techniques:

1. Frequency doubling the output of a tunable dye laser.
2. Frequency doubling the output of a Nd:YAG-pumped dye laser and then mixing this radiation in a second KDP crystal with the Nd:YAG laser fundamental at 1064nm to produce the required UV at shorter wavelengths.
3. Raman shifting, using an appropriate gas (normally H_2) the output of a frequency doubled or near-UV dye laser.

The first two techniques have been described in detail in the experimental details section (Chapter 3) of this work. Raman shifting down to about 180nm can produce laser light pulses intense enough for two-photon excitation.

The experiments of Rhodes et al [10,11] on the two-photon fluorescence excitation of the $H_2(E,F)\ {}^1\Sigma_g^+$ state using fixed frequency and line-tunable ArF (193nm) radiation are of interest to this work. The H_2 $(E,F)\ {}^1\Sigma^+g$ state is a distinct symmetric 'double-minimum' potential [12] formed from the avoided crossing of the potential energy curves of the E $1S\sigma g\ 2S\sigma g\ {}^1\Sigma_g^+$ and the F $1\sigma_u^2\ {}^1\Sigma_g^+$ states. The inner E-well has considerable 'Rydberg' character and the outer F-well has considerable $H^+ \ldots H^-$

'Ion-pair' character.

Early studies of discharge excited emission from this double minimum state by Dieke [13,14] suggested that the observed transitions could be assigned to two separate band systems, E $^1\Sigma_g^+$ - B $^1\Sigma_u^+$ and the F $^1\Sigma_g^+$ - B $^1\Sigma_u^+$ transitions. Further investigations have shown that these two states are strongly coupled and form a double-minimum potential. The vibronic wavefunctions of this state will have both inner 'Rydberg'-well and outer 'Ion-pair'-well character. The observation of two-photon excited fluorescence from this E,F state offers the intriguing possibility of studying the coupling between the two minima by observing the relative fluorescence yields from each. This will be a theme central to the discussion of the fluorescence spectroscopy of HCl in this work.

[2+1] REMPI of the E,F state of H_2 is now also an established technique for studying this state [15-20]. Time-of-flight mass analysis shows that H^+ and H_2^+ are both produced in varying relative yields at the ionisation step. Recently, Chandler and Thorne [20] have suggested that the amount of H^+ production is a measure of the degree of 'F-well' character of the vibrational wavefunction. This then represents another possible means of monitoring the relative 'Rydberg' - 'Ion-pair' contribution to the given vibronic wavefunction.

5.2 SOME THEORETICAL CONSIDERATIONS

As discussed in Chapter 4 mixing of all the $^1\Sigma^+$ or 0^+ states of HCl with the B $^1\Sigma^+$ 'Ion-pair' state dominates their spectroscopy. It seems that the 'Ion-pair' state is strongly vibronically coupled with the E $^1\Sigma^+$ state. Twenty four vibrational levels in the B $^1\Sigma^+$ state, up to v' = 26 have been observed in VUV absorption spectra [21]. Above v' = 6 gross anomalies in the vibrational and rotational energy levels are observed. It is likely that this behaviour is a manifestation of the coupling between the B $^1\Sigma^+$ and the E $^1\Sigma^+$ states. From Figure 4.9 in Chapter 4 it can be seen that the biggest vibrational perturbations occur where the E state vibrational levels intrude into the 'Ion-pair' state manifold, i.e. where the interaction with the E state is strongest.

Perturbations occurring between states of identical symmetry, i.e. those with identical values of Λ, Σ and S can be caused by two possible types of off-diagonal matrix elements connecting these states [22], those of the electronic H^{el} and nuclear motion T^N operators.

$$\langle 1,\Lambda,\Sigma,S|H|2,\Lambda,\Sigma,S\rangle = \langle \phi_1|H^{el}|\phi_2\rangle + \langle \phi_1|T^N|\phi_2\rangle \qquad 5.1$$

The ideal starting point would be a basis set, ϕ_1 and ϕ_2 that minimises the values of the off-diagonal matrix elements. It is not possible to find solutions of the electronic Hamiltonian for which both terms of equation 5.1 are zero. Two possible types of electronic functions may be defined:

1. Diabatic functions where

$$\langle\phi_1^d|T^N|\phi_2^d\rangle_r = 0 \qquad 5.2$$

and hence

$$\langle\phi_1^d|H^{el}|\phi_2^d\rangle_r = H_{12}(R) \neq 0 \qquad 5.3$$

(R is the internuclear separation, r is the electronic coordinate.)

This means that the diabatic potential curves associated with these ϕ_i^d functions can cross. The well known non-crossing between electronic states of identical symmetry applies only for exact solutions of the electronic Hamiltonian.

2. Adiabatic functions are precisely those that diagonalise the electronic Hamiltonian at every value of R.

$$\langle\phi_1^{ad}|H^{el}|\phi_2^{ad}\rangle_r = 0 \qquad 5.4$$

with

$$\langle\phi_1^{ad}|T^N|\phi_2^{ad}\rangle_r \neq 0 \qquad 5.5$$

In principle, whatever the initial model, after introducing the vibronic coupling terms corresponding to the chosen type of deperturbed potential curves the experimental energy levels are obtained by diagonalising one or other interaction matrix. Thus, if the deperturbed curves intersect and are characterised by very different molecular constants, then they are diabatic curves, see Figure 5.1. If the crossing is avoided, adiabatic curves are involved and one of the curves can have a double minimum.

Ab-initio calculations [23-25] of the electronic structure of the excited states of HCl, which are necessarily conducted in an adiabatic representation, suggest that the 'Ion-pair' potential is a double-minimum formed by the 'avoided-crossing' of it with a Rydberg state of the same electronic symmetry. Recent results [25] suggest that the inner 'Rydberg' minimum is shallow supporting a few vibrational levels. However, these have not been observed in previous VUV absorption studies [21] nor in this work and we believe that the 'Ion-pair' potential has a shoulder rather than an inner minimum, see Figure 5.2. The E $^1\Sigma^+$ state then may be formed as the residual state as a result of the avoided-crossing.

Energy level calculations in the diabatic representation of the coupling between suitable approximations to an 'Ion-pair' state and a 'Rydberg' state of the same symmetry in HCl were performed by my colleagues G. McFadyen and Dr. K.P. Lawley. The results from the diabatic coupling programs were in very poor agreement with experimentally determined vibronic level structure. This is due in part to the lack of reliable potential energy curves and also the use of the diabatic representation which is a poor zeroth-order approximation for this particular case where a constant coupling parameter is used. With the use of a variable coupling

FIGURE 5.1 Diabatic and adiabatic potential curves. The diabatic curves (solid lines) 1 and 2 cross at R_c and are defined by neglecting the part of H^{el} that causes the adiabatic curves (dotted lines) to avoid crossing by $2H_{12}$ at R_c.

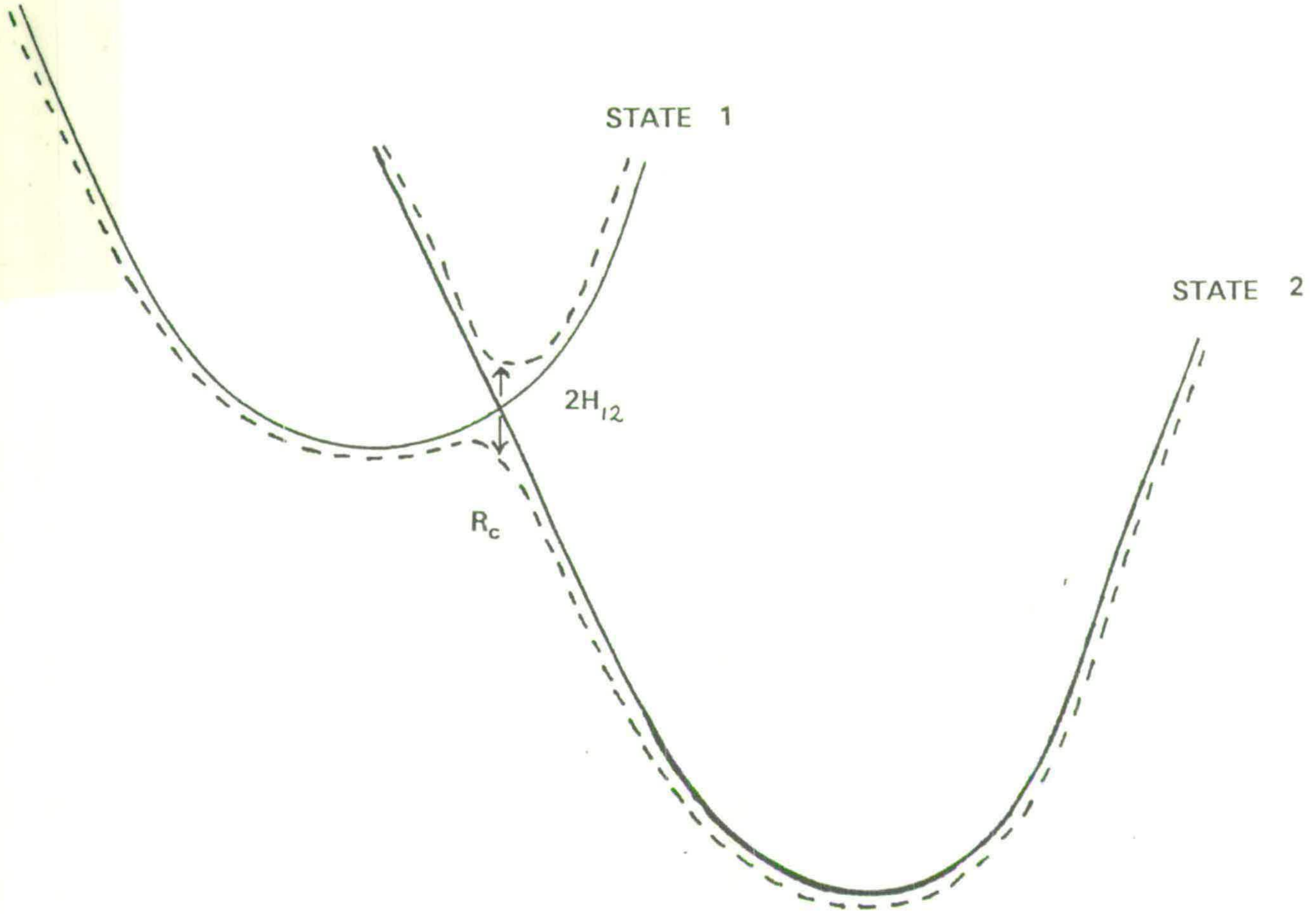

FIGURE 5.2 Potential Energy Curves for HCl

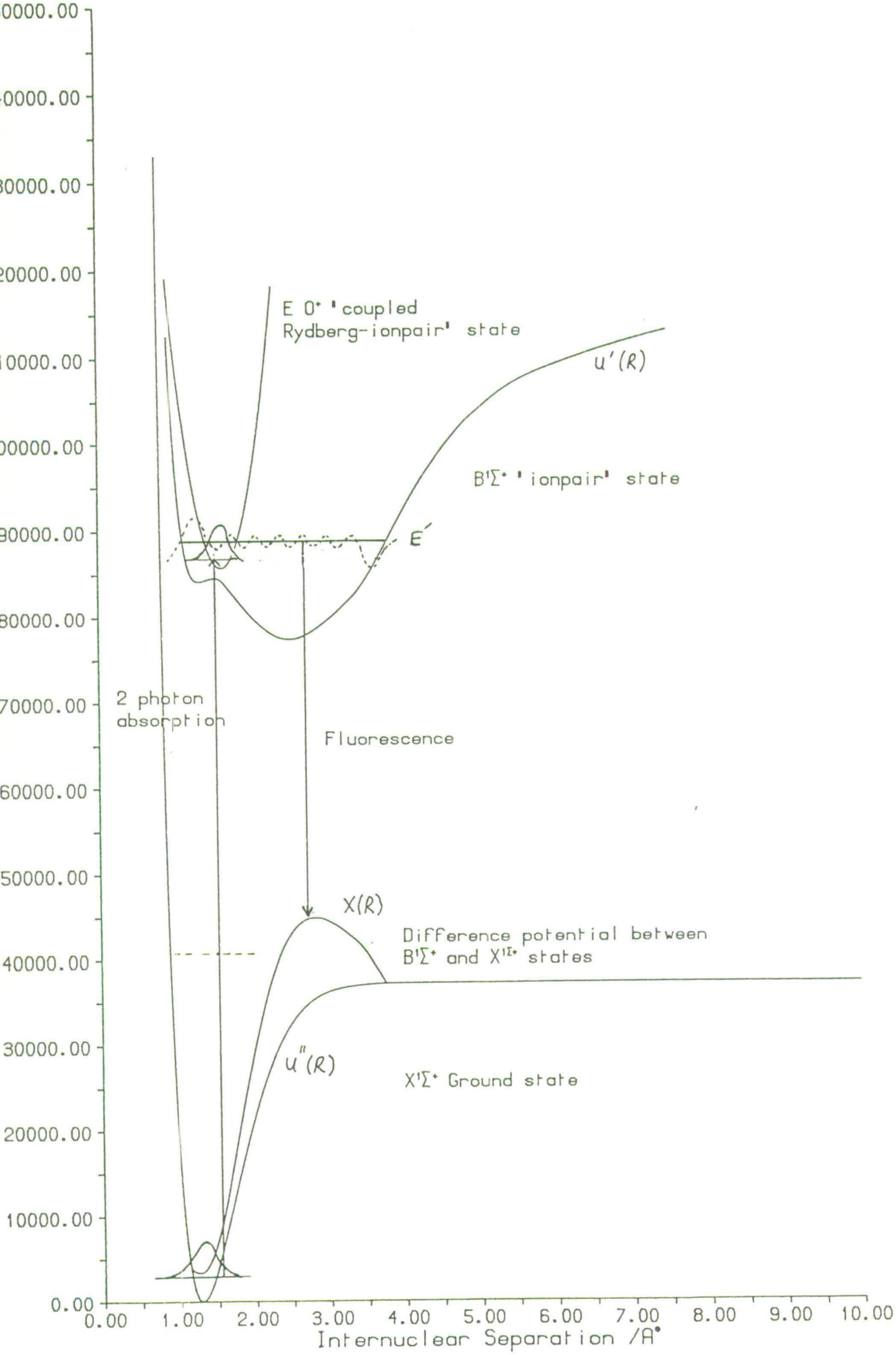

parameter, more coupling elements and improved potentials this approach could yield better results. In view of the gross mixing an adiabatic coupling representation would be a better starting point. This requires better potential energy curves beyond those obtainable at present from the ab-initio calculations.

The B $^1\Sigma^+$ 'Ion-pair' potential was modelled as follows. The bottom of the potential from v' = 0 to v' = 6 can be described accurately by the RKR analysis of Coxon and Roychowdhury [26]. This extends only for about 5,100 cm^{-1}, which is approximately 10% of the potential well. The attractive limb potential energy can be described by the terms of a Rittner function:

$$V_{(R)} = \frac{-e^2}{R} - \frac{\alpha e^2}{2R^4} + \ldots \qquad 5.6$$

where e is the electronic charge, R is the internuclear separation and α is the Cl^- ion polarisability. The free anion polarisability is not known but it can be estimated by extrapolation from measurements made in ionic crystals [27] or by calculation [28]. A value of 4.4 $Å^3$ was taken. The resulting potential energy function was combined with the RKR potential by a smooth extrapolation. The repulsive limb was modelled with the guidance of the ab-initio potential surface [25], suitably modified to produce a shoulder rather than a shallow inner minimum. The resulting potential is as shown in Figure 5.2. The E $^1\Sigma^+$ 'Coupled-Rydberg' state can be modelled initially with a parabola or a Morse potential curve with an equilibrium bond length r_e = 1.6 Å. The ground electronic state potential surface is also shown. It is taken from the results of Coxon [29]. Our most recent calculations of the 'Ion-pair' state potential suggest that the T_e of the E $^1\Sigma^+$ state is such that it brings it too close to the 'Ion-pair' state for it to be the 'residual' state formed during an 'avoided crossing' of the 'Ion-pair' state. The ultimate aim then of the adiabatic coupling calculation is to reproduce the known vibronic level structure in HCl and the isotopic analogue DCl of the coupled $^1\Sigma^+$ (0^+) states concerned. Unfortunately, this two state coupling may be a simplification as other 0^+ symmetry states are known to have 'Ion-pair' character, evidenced by their rotational constants and also by fluorescence spectroscopy as will be shown.

5.3 RESULTS

Emission in the 230 nm region from the 'Ion-pair' B $^1\Sigma^+$ state has been known for some time [30]. The fluorescence occurred from low vibrational levels in the 'Ion-pair' state to high vibrational levels of the ground electronic state. Fluorescence can also be excited from higher vibrational levels in the 'Ion-pair' manifold using two-photon excitation. Figure 5.3 shows the two-photon excitation of the B $^1\Sigma^+$ v' = 11 'Ion-pair' level and the E $^1\Sigma^+$ 'Coupled-Rydberg' state, v' = 0 level

FIGURE 5.3 Emission collected around 226 nm.

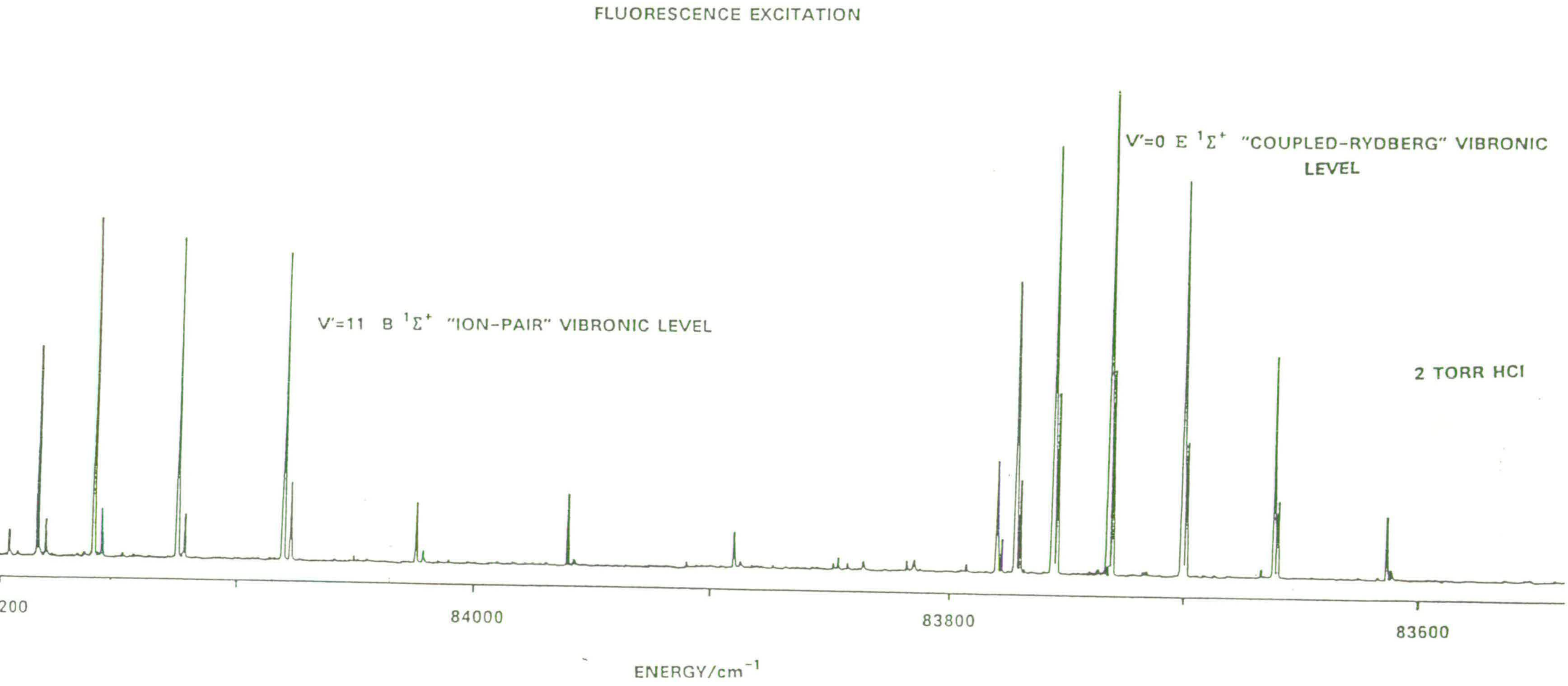

collecting fluorescence around 226nm with a bandpass of ~ 2nm. Fluorescence excitation spectra are recorded as described in Chapter 3. The observation of fluorescence from the E $^1\Sigma^+$ state is indicative of the considerable 'Ion-pair' character of the state. The vibronic coupling between it and the 'Ion-pair' state is such that the E $^1\Sigma^+$ wavefunctions are coupled with the vibrations of the 'Ion-pair' well that have amplitudes characteristic of that potential. This then allows fluorescence to the ground state in the same wavelength region as the 'Ion-pair' state. Collisional transfer of population from the E $^1\Sigma^+$ state to the B $^1\Sigma^+$ state can be eliminated as the E $^1\Sigma^+$ state is seen to fluoresce in the 230nm region even at pressures as low as 50 mTorr (6.66Nm^{-2}). Much weaker fluorescence is also seen from the v' = 1 level of the E $^1\Sigma^+$ state. The g $^3\Sigma^-(0^+)$ state v' = 0 vibrational level is also observed to fluoresce weakly in the 230 nm region indicating the 'Ion-pair' character even of this state, see Figure 5.4. The system fluorescing at lower energy is due to emission from the B $^1\Sigma^+$ v' = 9 'Ion-pair' level, as shown. Fluorescence is observed between 260-400nm for both the E $^1\Sigma^+$ and 'Ion-pair' vibrational levels. Figure 5.5 shows the fluorescence excitation spectrum of the B $^1\Sigma^+$, v' = 11 and E $^1\Sigma^+$, v' = 0 levels collecting fluorescence around 330nm. This emission most probably results from transitions to the unbound A $^1\pi$ state. The g $^3\Sigma^-(0^+)$ and F $^1\Delta_2$ states also fluoresced weakly in this region, see

FIGURE 5.4 Emission collected around 226 nm.

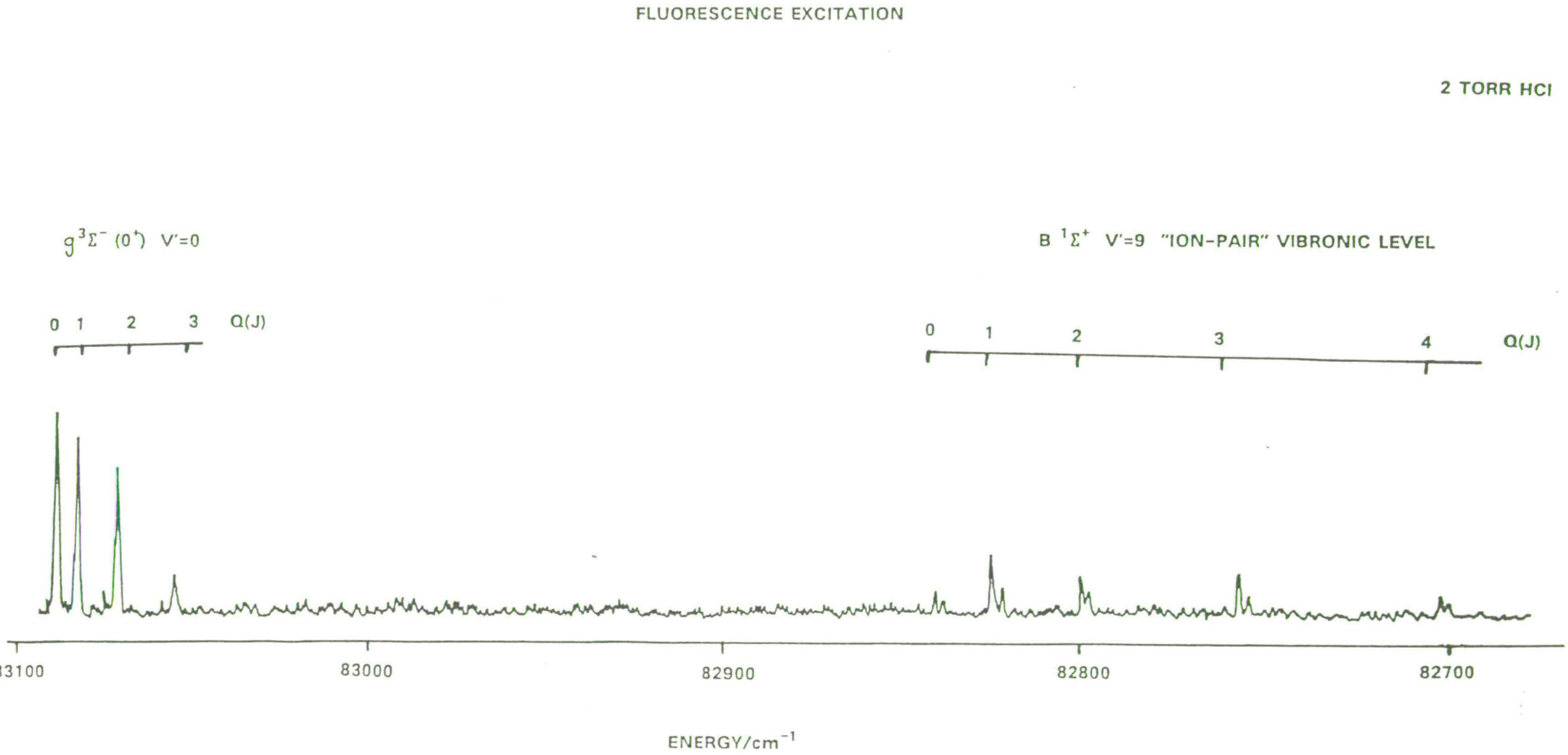

FIGURE 5.5 Emission collected around 330 nm.

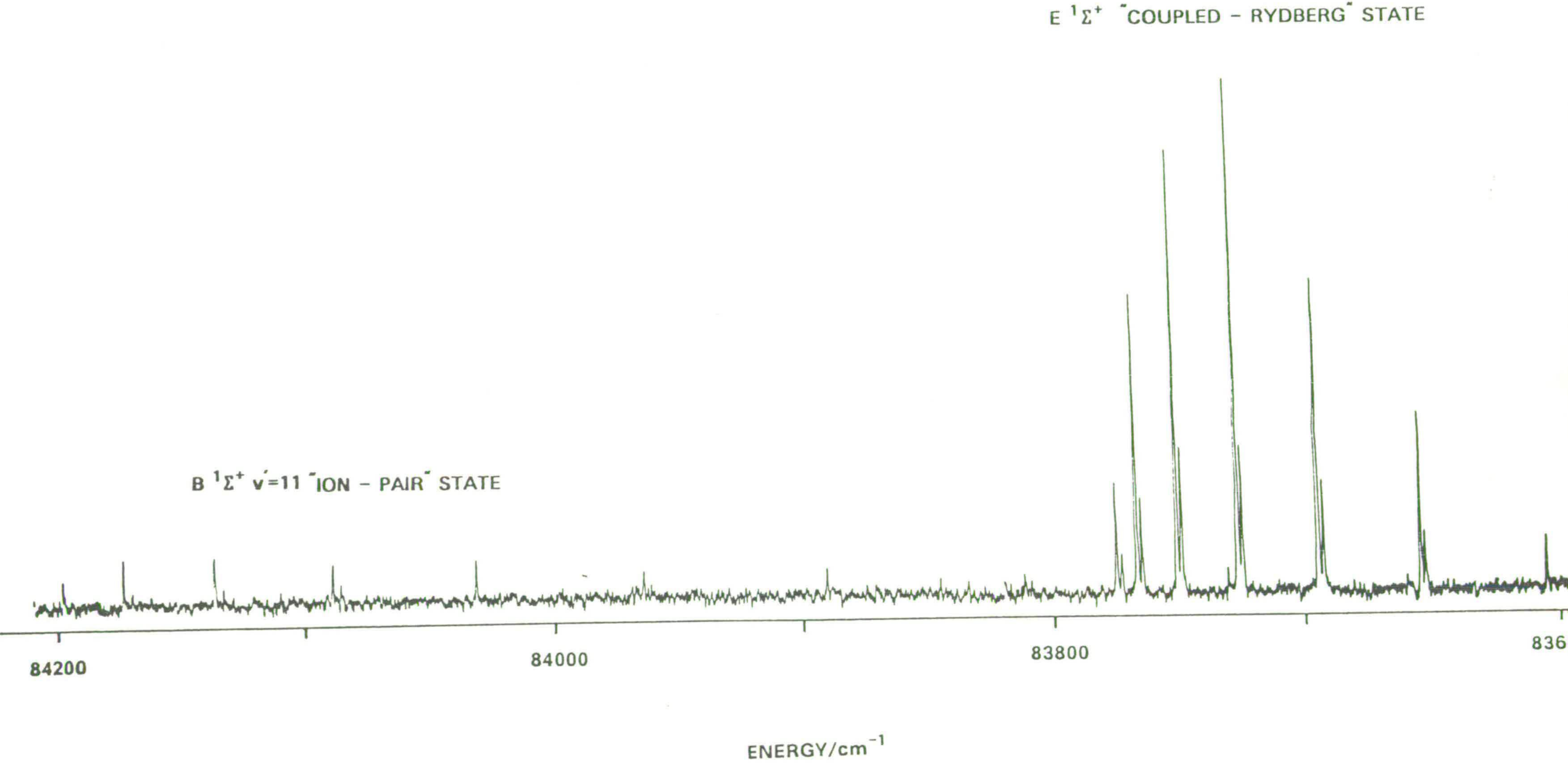

Figure 5.6. Thus it appears that those electronic states of strong 'Rydberg' character, i.e. F $^1\Delta_2$, f $^3\Delta_2$ only fluoresce in the 260-400nm region. Those electronic states which are coupled with the 'Ion-pair' state or the 'Ion-pair' state itself give rise to emission around 230 nm. Thus the observation of fluorescence around 230 nm is a means at least on a qualitative level of assessing the 'Ion-pair' or 'Rydberg' character of the excited electronic state.

Using laser ionisation time-of-flight mass spectrometry to study Cl^+ yields following REMPI of HCl has recently been shown as an indirect means of studying the very same phenomena [31]. 'Rydberg' states like the F $^1\Delta_2$ state ionise to give predominantly HCl^+ molecular ions in their ionisation spectrum, whereas 'Ion-pair' and mixed 'Rydberg' - 'Ion-pair' states tend to give significant yields of Cl^+ ions. The yield apparently depends on the degree of 'Ion-pair' character of the state.

Figure 5.7 shows dispersed fluorescence spectra of the B $^1\Sigma^+$ $v' = 11$ - X $^1\Sigma^+$ and the E $^1\Sigma^+$ $v' = 0$ - X $^1\Sigma^+$ transitions. The spectra were recorded at an HCl pressure of 3 Torr ($399.96Nm^{-2}$) using the Jobin-Yvon HRS2 spectrometer at a resolution of ~0.3nm f.w.h.m. The spectrum has not been corrected for the response of the spectrometer and photomultiplier over the wavelength range scanned. The long wavelength end of each spectrum exhibits characteristic 'bound-free' emission

FIGURE 5.6 Emission collected around 330 nm.

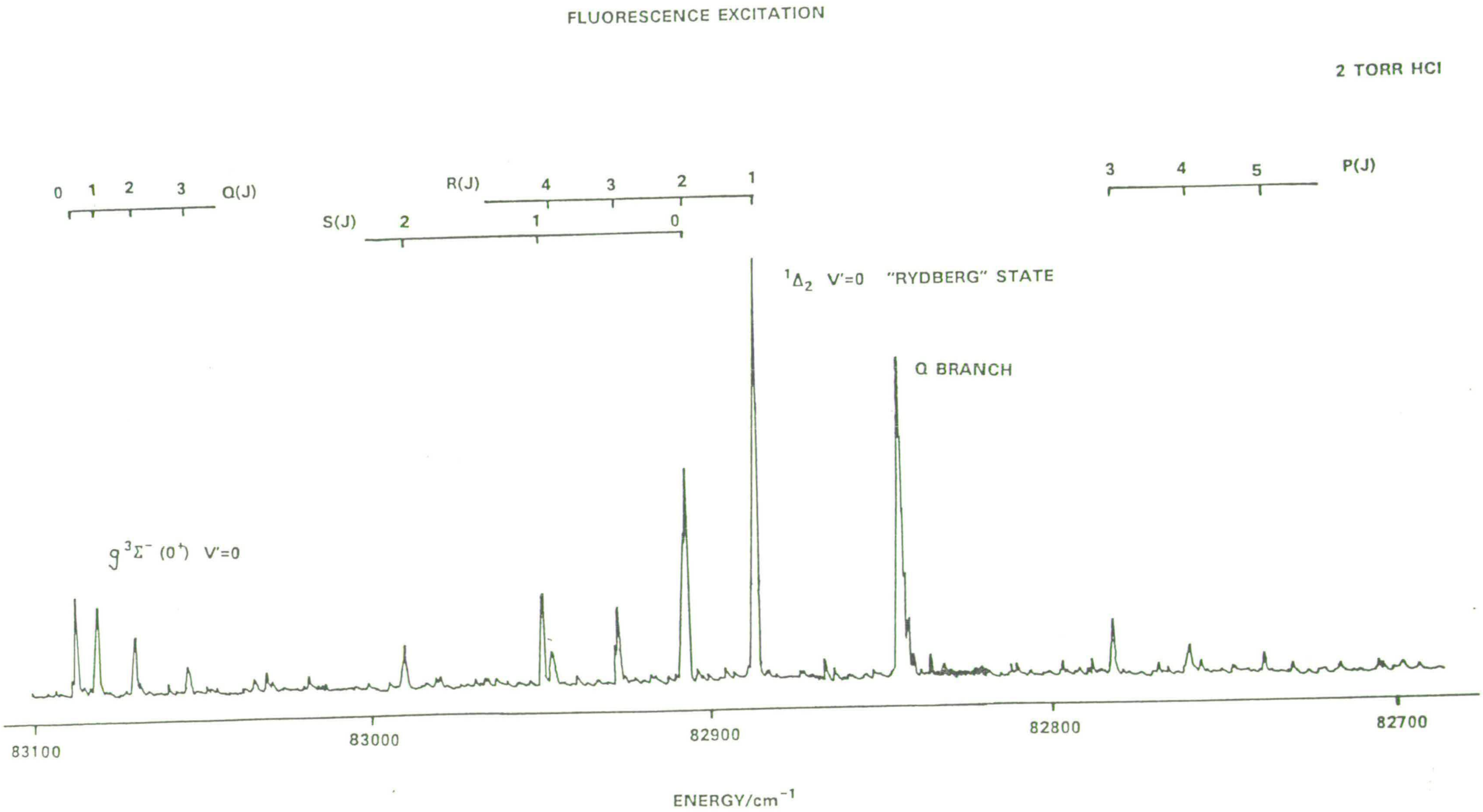

DISPERSED FLUORESCENCE ($B\ \Sigma \rightarrow X\ \Sigma$)

FROM THE $V'=11$ $B\ ^1\Sigma^+$ "ION-PAIR" VIBRONIC LEVEL

$V'=0$ $E\ ^1\Sigma^+$ "COUPLED-RYDBERG" VIBRONIC LEVEL

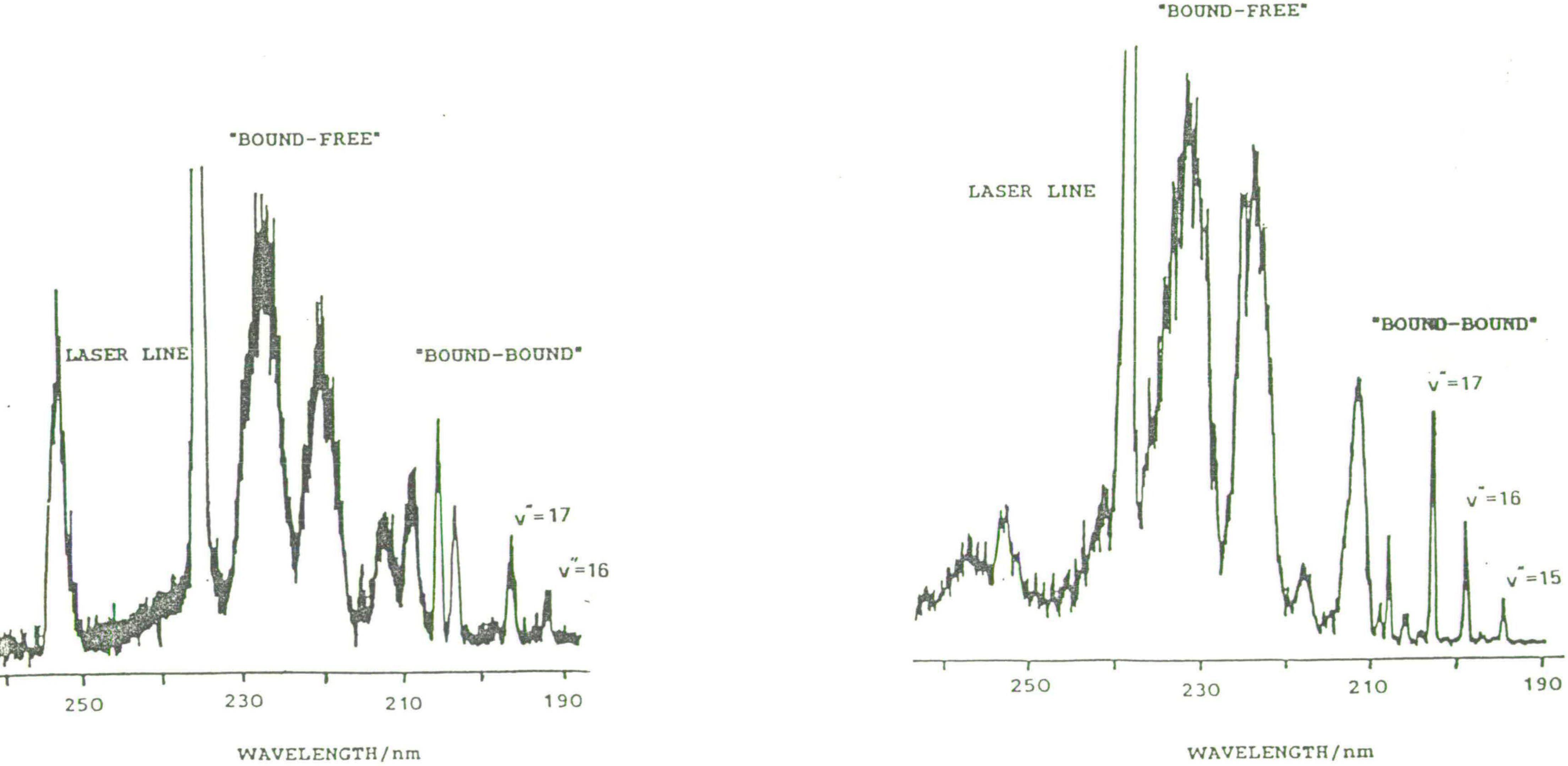

FIGURE 5.7

corresponding to emission essentially to the vibrational continuum of the ground state. At shorter wavelengths, transitions to discrete vibrational levels associated with the ground state manifold can be observed. Obtaining sufficient fluorescence intensity to record dispersed emission spectra is difficult and generally requires the lasers operating at full power. In order to extend the wavelength region into the vacuum ultra-violet, the Acton VUV monochromator was used, as described in Chapter 3. Fluorescence down to about 170 nm was studied. The resolution of the monochromator at 80 μ slitwidths was ~1.75nm f.w.h.m. For selected vibronic levels of the 'Ion-pair' state, namely v' = 11, 12 and 15 dispersed fluorescence spectra were obtained.

The spectra are as shown in Figures 5.8 (a-c) respectively and are not corrected for the response of the photomultiplier and monochromator.

Certain features of the spectrum can reveal information on the potential energy curves between which the transitions occur [32]. Generally the 'bound-free' oscillatory continuum emission consists of a low frequency envelope of higher frequency structure. Inherent in the discussion of bound-free spectra is the concept of the 'difference potential'. As dictated by the Franck-Condon principle for electronic transitions, to a very good approximation the nuclear positions and momenta are conserved during the transition. Thus for diatomics, such transitions can be represented on

FIGURE 5.8 Dispersed fluorescence spectra.

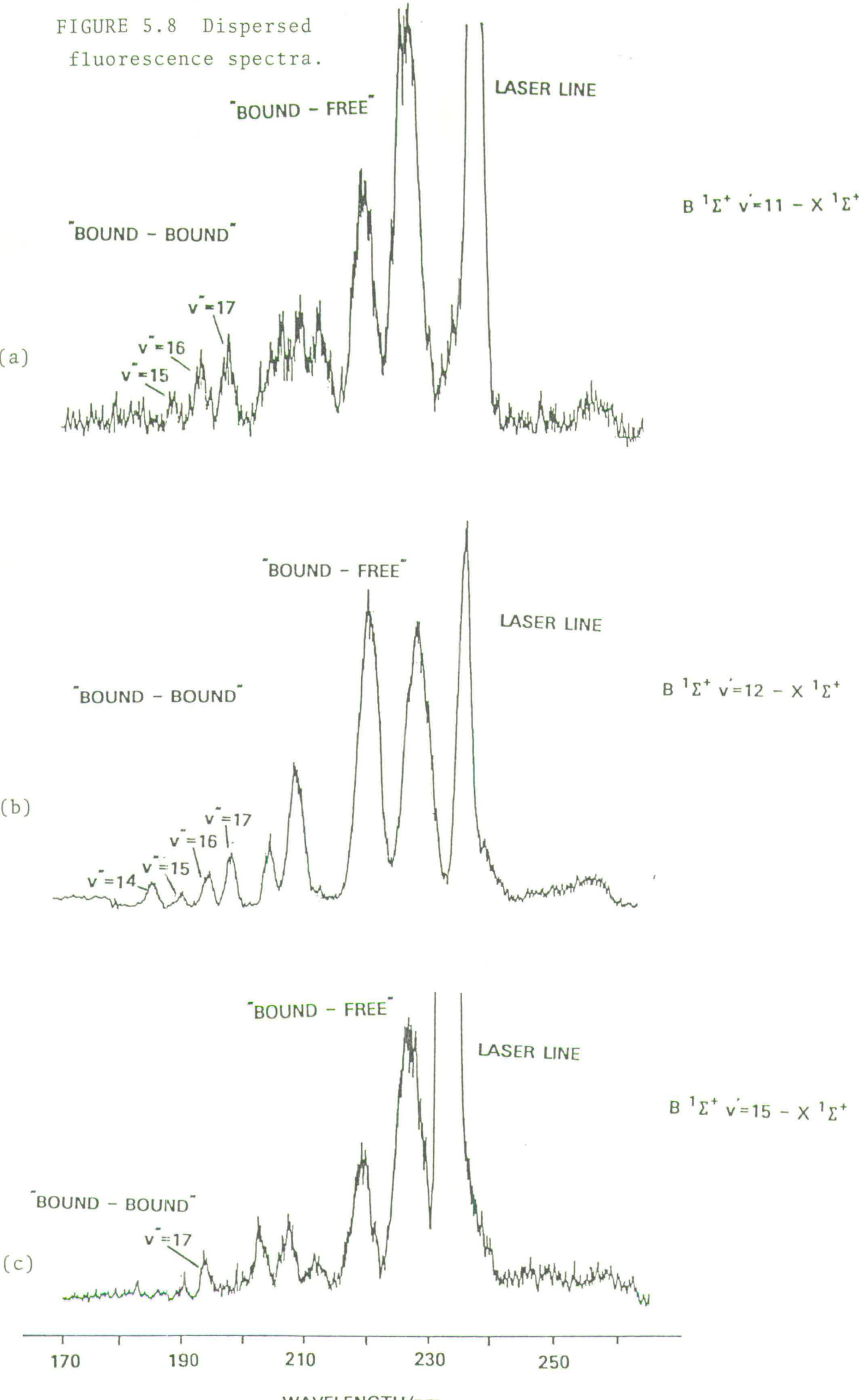

potential diagrams as vertical lines from the initial energy E_i and position R to an energy E_f in the final state for which the kinetic energy, $E_f - U_f(R)$($U_f(R)$ is the potential energy) is the same as in the initial state, $E_i - U_i(R)$. Thus the difference potential curve X(R) represents the locus of points which classically conserve nuclear position and momentum for the indicated E' level, see Figure 5.2

$$X(R) = U''(R) + E' - U'(R) \qquad 5.7$$

Where the difference frequency exhibits an extremum as shown, the observed spectrum is then a product of the interference between transitions to the same energy level but which end on different limbs of the difference potential. The spectrum has the appearance of a modulated sinusoidal function oscillating under a lower frequency envelope. In a crude sense the coarse structure depends only on the shape of the difference potential, whereas the fine structure depends on the location of the difference potential relative to the repulsive branches of the two potentials. Thus the simulation of dispersed fluorescence, given one or other of the potential curves, is a valuable way of obtaining information on the functional form of the other potential. In the case of HCl the ground state potential is known with reasonable accuracy and thus by assuming a functional form for the 'Ion-pair' state potential simulations of the spectrum between the two states can be obtained.

Figure 5.9 shows the experimental and simulated spectra of the emission from the B $^1\Sigma^+$ v' = 12 vibrational level. The simulation was performed by G. McFadyen. The 'Ion-pair' potential used and the calculated difference potential are as shown in Figure 5.2. No vibronic coupling of the B $^1\Sigma^+$ 'Ion-pair' state with the E $^1\Sigma^+$ state is included and thus the simulated spectrum represents a best first approximation.

The simulated spectrum was developed in a fully quantum calculation which utilised tabulated internuclear potential energy curves to determine the wavefunctions of the bound initial states and the bound and continuum final states. Franck-Condon factors and densities between these states were then evaluated and a simulated spectrum (which incorporated the resolution of the experimental apparatus being used) was produced. The transition dipole moment function used in the calculation of Franck-Condon factors and densities may be altered to fit the intensities of the simulated spectrum to the experimental one. Generally, a Gaussian centred at ~2.8 Å was used, because at this bond length the ground state electronic configuration changed from being essentially ionic to predominantly covalent.

Thus it is possible by systematically altering the 'Ion-pair' state potential and simulating the experimental spectra to obtain a better functional form

FIGURE 5.9 Dispersed fluorescence spectra.

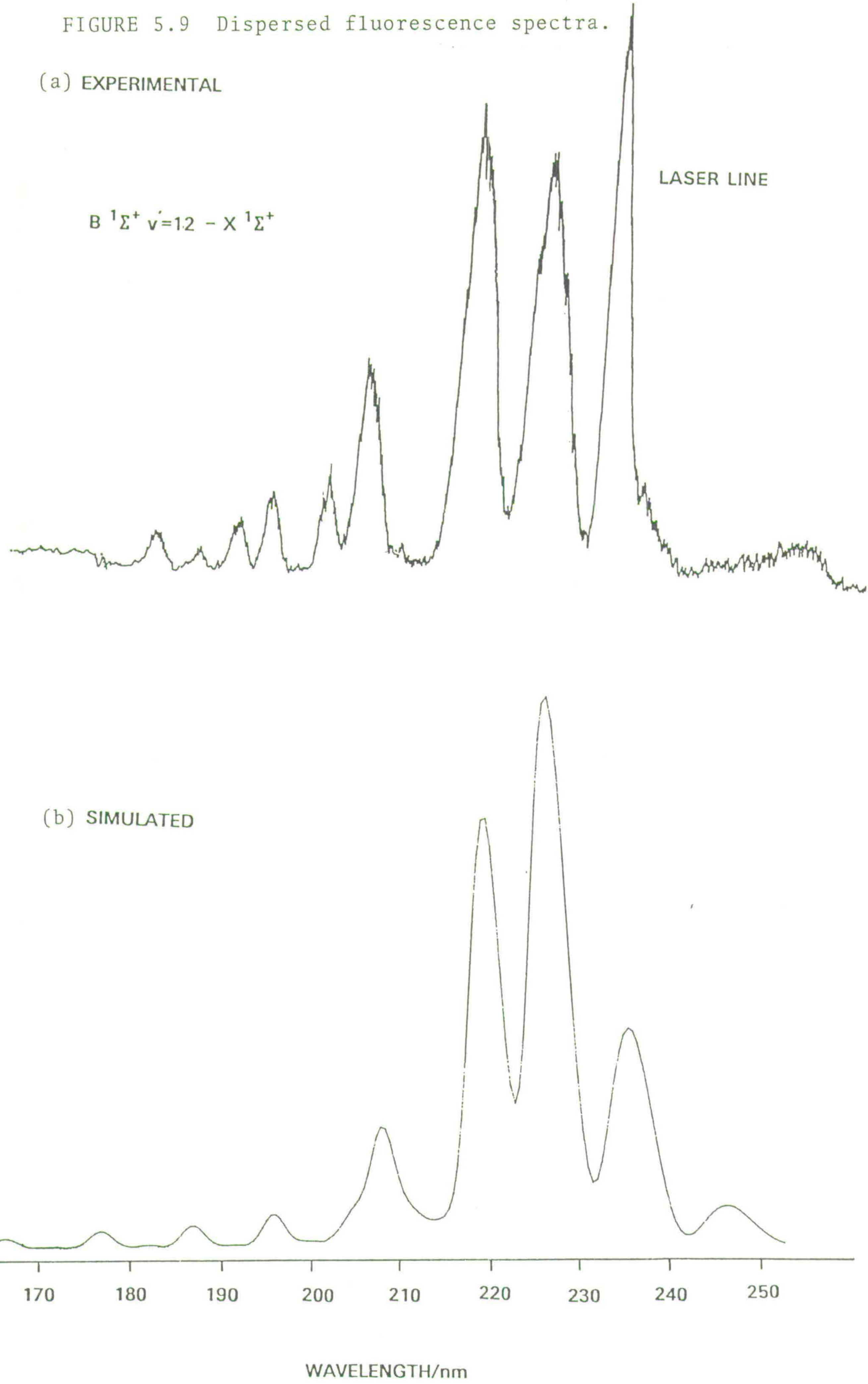

for the potential.

Obviously the next stage is to include the vibronic coupling with the E $^1\Sigma^+$ state and to simulate its fluorescence spectrum to the X $^1\Sigma^+$ state. This work is at present being extended to include a similar study on DCl and ultimately it is hoped using a combination of the above experimental and theoretical techniques to provide a satisfactory explanation to the observed vibronic level structure in the states concerned.

5.4 REFERENCES

1. J.B. Nee, M. Suto and L.C. Lee, J. Chem. Phys., 85, 719 (1986).
2. J.B. Nee, M. Suto and L.C. Lee, J. Chem. Phys., 85, 5027 (1986).
3. G. Zimmerer p.357 in 'Photophysics and Photochemistry above 6 eV', edited by F. Lahmani (Elsevier Science Publishers, Amsterdam 1985).
4. W. Meier, H. Rottke, H. Zacharias and K.H. Welge, J. Chem. Phys., 83, 4360 (1985).
5. J.W. Hepburn, D. Klimek, K. Liu, R.G. Mcdonald, F.J. Northup and J.C. Polayni, J. Chem. Phys., 74, 6226 (1981).
6. H. Rottke and H. Zacharias, J. Chem. Phys. 83, 4831 (1985).
7. S.V. Filseth, R. Wallenstein and H. Zacharias, Opt. Commun., 23, 231 (1977).
8. C. Kittrell, S. Cameron, L. Butler, R.W. Field and R.F. Barrow, J. Chem. Phys., 78, 3623 (1983).
9. N. van Veen, P. Brewer, P. Das and R. Bersohn, J. Chem. Phys., 77, 4326 (1982).
10. D.J. Kligler and C.K. Rhodes, Phys. Rev. Lett., 10, 309 (1978).
11. D.J. Kligler, J. Bokor and C.K. Rhodes, Phys. Rev. A, 21, 607 (1980).
12. L. Wolniewicz and K. Dressler, J. Mol. Spectrosc., 67, 416 (1977).
13. G.H. Dieke, Phys. Rev., 50, 797 (1936).

14. G.H. Dieke, Phys. Rev., 76, 50 (1949).

15. E.E. Marinero, C.T. Rettner and R.N. Zare, Phys. Rev. Lett., 48, 1323 (1982).

16. E.E. Marinero, R. Vasudev and R.N. Zare, J. Chem. Phys., 78, 692 (1983).

17. S.L. Anderson, G.D. Kubiak and R.N. Zare, Chem. Phys. Lett., 105, 22 (1984).

18. D.H. Parker, J.D. Buck and D.W. Chandler, J. Phys. Chem., 91, 2035 (1987).

19. D.W. Chandler and R.L. Farrow, J. Chem. Phys., 85, 810 (1986).

20. D.W. Chandler and L.R. Thorne, J. Chem. Phys., 85, 1733 (1986).

21. A.E. Douglas and F.R. Greening, Can. J. Phys., 57, 1650 (1979).

22. H. Lefebvre-Brion and R.W. Field in 'Perturbations in the Spectra of Diatomic Molecules', (Academic Press, 1986).

23. M. Bettendorf, S.D. Peyerimhoff and R.J. Buenker, Chem. Phys., 66, 261 (1982).

24. P.J. Bruna and S.D. Peyerimhoff in 'Ab-initio Quantum Chemistry Vol. 1, edited by K.P. Lawley (Wiley, New York, 1986).

25. S.D. Peyerimhoff, private communication 1986.

26. J.A. Coxon and U.K. Roychowdhury, Can. J. Phys., 63. 1485 (1985).

27. J.N. Wilson and R.M. Curtis, J. Phys. Chem., 74, 187 (1970).

28. P.W. Fowler and P.A. Madden, Phys. Rev. B., 29, 1035 (1984).

29. J.A. Coxon, J. Mol. Spectrosc., 117, 361 (1986).

30. J.K. Jacques and R.F. Barrow, Proc. Roy. Soc. London, 73, 538 (1958).

31. T.A. Spiglanin, D.W. Chandler and D.H. Parker, Chem. Phys. Lett., 137, 414 (1987).

32. J. Tellinghuisen in 'Advances in Chemical Physics', Vol. 60, p.299 (John Wiley, 1985).

CHAPTER 6

REACTIONS OF ELECTRONICALLY EXCITED HCl WITH THE RARE GASES KRYPTON AND XENON

6.1 INTRODUCTION

The importance of rare gas halide exciplex (excimer) lasers is now such that understanding the reactions that may be occurring inside the discharge plasmas of these lasers is of considerable interest. Thus, any reactive process involving hydrogen chloride (the primary Cl-containing fuel in commercial XeCl and KrCl excimer lasers) leading to rare gas halide exciplex formation may be important.

The reactions of electronically excited Xe and Kr with hydrogen chloride have been studied both in the bulk gas and under molecular beam-gas collision conditions. The type of reactive process undergone depends very much on the state selection of the noble gas. In particular the reactions of excited noble gas atoms with Cl-containing molecules leading to rare gas halide exciplex formation have been well studied [1-7]. Golde et al [8] have shown that for electronically excited, metastable Xe(6s $^3P_2$), the major reactive channel was dissociative excitation of HCl, leading to near unity yields of H and Cl atoms. Under these thermal conditions, very little or no exciplex halide emission was observed when Xe($^3P_2$) was reacted with HCl. The energy threshold for this reactive channel, 8.46eV, was somewhat greater than the 8.32eV of energy available from the Xe($^3P_2$) atom. However, Simons et al [1] showed that using an accelerated beam of Xe($^3P_2$) atoms, to overcome the energy barrier, on collision with HCl, xenon chloride exciplex XeCl* (B $^2\Sigma^+$) was formed. The exciplex was detected by the associated characteristic emission to the ground state (X $^2\Sigma^+$) around 308 nm. Spin-orbit excitation [1] of the Xe to $^3P_1$ or vibrational excitation [9] of the HCl also led to enhancement in the yield of exciplex product. Ku and Setser [2] have shown that two-photon UV laser excitation of the Xe(6p) J = 0 and J = 2 states [10] in the presence of HCl led to large branching ratios for exciplex formation, i.e. the ratio of the rate of XeCl* formation to the total removal rate of the excited Xe atoms.

This behaviour became more marked with increasing electronic excitation of the Xe atom, i.e. the branching ratio for Xe(6p[$\frac{1}{2}$]$_o$) > Xe(6p[$\frac{3}{2}$]$_2$) > Xe(6p[$\frac{5}{2}$]$_2$) with the atomic energy levels at 80, 119cm^{-1}, 79,212cm^{-1} and 78,120cm^{-1}, respectively [10].

The reactions of electronically excited krypton have been less extensively studied. Golde et al [8] have observed unity yields of H and Cl atoms, that were formed via dissociative excitation during the reaction of Kr($^3P_2$) atoms at 9.92eV with ground state HCl. As for Xe($^3P_2$) atoms, near resonant energy transfer to dissociative excited states of HCl was held likely to be occurring. The formation of the KrCl* exciplex (B $^2\Sigma^+$) has an energy threshold of 10.02eV and was thus barely accessible at thermal energy collisions between Kr($^3P_2$) and HCl. Formation of the KrCl* exciplex can be readily shown by its characteristic B $^2\Sigma^+$ - X $^2\Sigma^+$ emission around 222 nm. Setser et al [11] have shown, as expected, that the branching ratio for KrCl* exciplex formation from the Kr($^3P_2$) and HCl reaction was very low, ~0.06.

Exciplex monohalides, particularly XeCl*, can be formed efficiently in a variety of other processes. For example, the laser-assisted photo-association reaction of Xe and Cl atoms has been shown to lead to exciplex formation [12,13]. In addition, excitation of a Xe...Cl$_2$ free pair in a laser-assisted collision at room temperature, with a statistical distribution of mutual orientations, leads to the exciplex product [14,15]. Most recently, excitation of a bound Xe...Cl$_2$ collision pair, with a well defined geometry, frozen in a Van der Waals complex has yielded the XeCl* exciplex [16,17].

These latter results are of great interest since they display the possibility of controlling the geometry of the entrance channel to a chemical reaction. It comes as no great surprise then that direct excitation of electronically excited Cl$_2$ by laser radiation in the presence of Xe [18] or using tunable synchrotron radiation in the presence of Kr [19] can yield the respective exciplex. Optical excitation of ICl in the presence of Xe has recently been shown to lead to XeCl* (B $^2\Sigma^+$) exciplex formation [20]. The role of 'Ion-pair' excited states of the Cl$_2$ and ICl molecules appears to be important in these reactions.

It would be of interest then to study the interaction of optically pumped, electronically excited HCl in the presence of Xe or Kr. This would complement the present data available on the interaction of excited Xe or Kr with ground state HCl.

6.2 RESULTS

The reaction:

$$HCl + Xe \longrightarrow XeCl^{*}\ (B\ ^{2}\Sigma^{+}) + H \qquad 6.1$$

has an energy threshold of 8.46eV. This means that for any of the bound excited electronic states of HCl, which all lie above 9.3eV, if populated, the reaction should proceed with a large amount of the exoergicity deposited in the internal energy of the $XeCl^{*}$ exciplex product. Thus, for example, two-photon excitation of HCl at the v' = 11 B $^{1}\Sigma^{+}$ 'Ion-pair' vibronic level or the E $^{1}\Sigma^{+}$ state, v' = 0 level in the presence of Xe leads to strong $XeCl^{*}$ B $^{2}\Sigma^{+}$ - X $^{2}\Sigma^{+}$ exciplex emission. Figure 6.1 shows the dispersed emission spectrum (in the range 190-320nm) following excitation of 1 Torr (133.3Nm^{-2}) HCl at the E $^{1}\Sigma^{+}$ state v' = 0, J' = 3 level in the presence of 10 Torr (1.33kNm^{-2}) of Xe. The spectrum was recorded using the Jobin-Yvon HRS2 spectrometer at a slit width of 400μ (~0.3nm f.w.h.m. resolution). The exciplex emission extends from 310nm to ~220nm suggesting considerable vibrational excitation in the product. The structured emission below 240nm is of course that due to

FIGURE 6.1 Dispersed fluorescence spectrum following excitation of HCl at the E $^1\Sigma^+$ state in the presence of Xe.

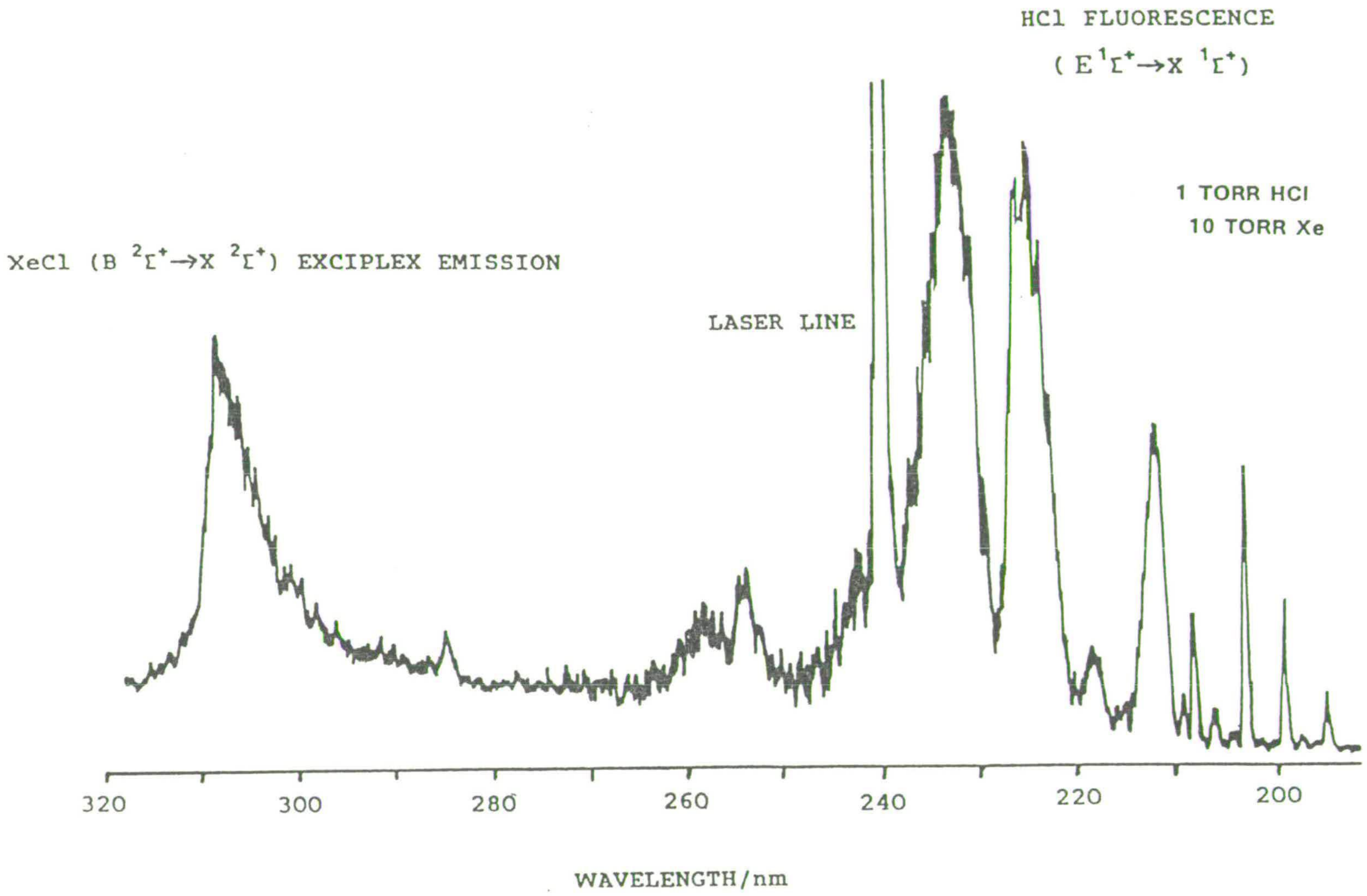

electronically excited HCl, as has been described in Chapter 5. Very weak emission around 345nm could also be observed. This was presumed to be $XeCl^*$ C-A emission [12], though there may also be a contribution due to emission from electronically excited HCl (see Chapter 5). Dispersed fluorescence spectra could not be obtained at sufficiently low total pressure (<1 Torr,<133.32Nm^{-2}) so as to maintain the nascent vibrational distribution of the exciplex product. Thus the characteristic oscillatory continuum fluorescence expected of a 'bound-free' transition was not seen, due to vibrational relaxation [7].

The $XeCl^*$ excitation spectrum closely resembles the two-photon fluorescence excitation spectrum of any of the respective HCl band systems, suggesting that the excited state is indeed directly responsible for the reactive process. Figure 6.2 shows the $XeCl^*$ excitation spectrum following excitation of the B $^1\Sigma^+$ state v' = 11 level and the E $^1\Sigma^+$ state v' = 0 level in HCl, in the presence of Xe. Accurate measurement of quantitative yields for $XeCl^*$ (B $^2\Sigma^+$) production is difficult, particularly with the lack of data on radiative lifetimes of electronically excited states in HCl. This, and to a lesser extent the restricted observation of the HCl emission bands to the spectral region above 170nm, makes quenching rate measurements difficult. Time-resolved measurements of the HCl^* fluorescence around 230nm at low pressure (100 mTorr, 13.33Nm^{-2}) show that the emission follows the

FIGURE 6.2 XeCl* exciplex excitation (action) spectrum.

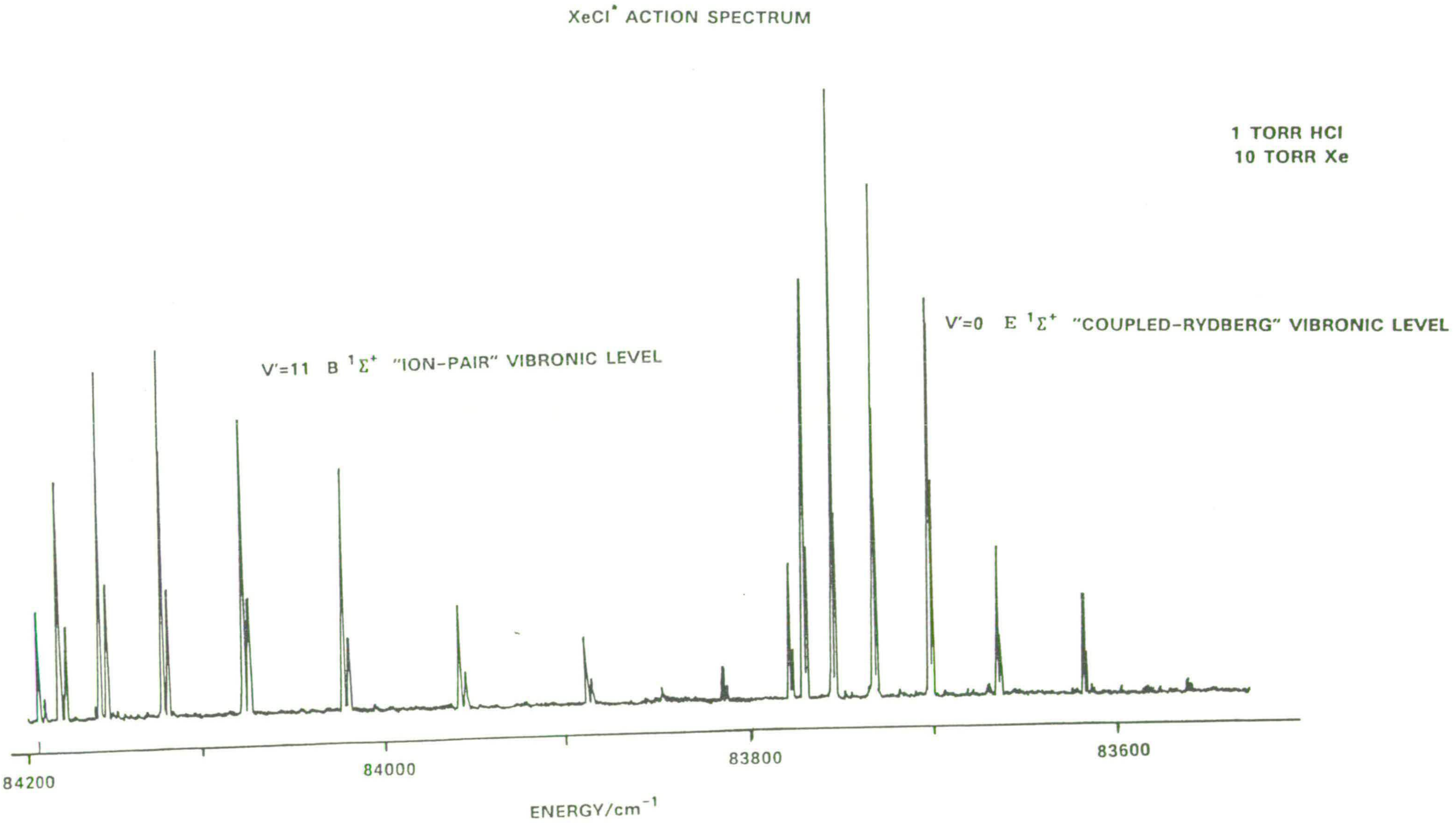

time profile of the laser pulse, thus suggesting a lifetime on the order of a few nanoseconds. Recent calculations [22] predict the B $^1\Sigma^+$ state fluorescence lifetime to be $\sim$2-4 ns, which confirms the above experimental observation. The quenching of the HCl* emission is obvious however, as shown by Figure 6.3. At 60 Torr (7.999kNm^{-2}) Xe pressure the HCl* emission around 230nm is effectively quenched. Figure 6.4 illustrates the behaviour of the integrated XeCl* B $^2\Sigma^+$ emission intensity as a function of Xe pressure. Above $\sim$75 Torr (10kNm^{-2}), quenching of the XeCl* exciplex by Xe becomes important, resulting in a decrease in the exciplex emission intensity. Knowing the XeCl* (B) state fluorescence lifetime (11.7±0.5ns) [12], and estimating the lifetime of the B $^1\Sigma^+$ 'Ion-pair' state of HCl to be 5ns, by following the dependence of the XeCl* and HCl* emission intensity as a function of Xe pressure, then crudely, it can be estimated that the yield for the exciplex formation might approach unity.

The lowest excited state of HCl* seen to react is the 'Rydberg' f $^3\Delta_2$ state, v' = 0 level (T_o=82015.1cm^{-1}). Figure 6.5 shows the XeCl* excitation spectrum obtained from this state. Although the electronic origins of the b $^3\pi_i$ (i=0,1,2) and the C $^1\pi$ states lie at lower energy, they appear to be too heavily predissociated for collisional processes to be important. The reaction of the 'Rydberg' states f $^3\Delta_2$ and F $^1\Delta_2$ at slightly higher energy (T_o=82847.1cm^{-1}) raises the question of the

FIGURE 6.3 Dispersed emission following excitation of the E $^1\Sigma^+$ state of HCl in the presence of 60 Torr of Xe.

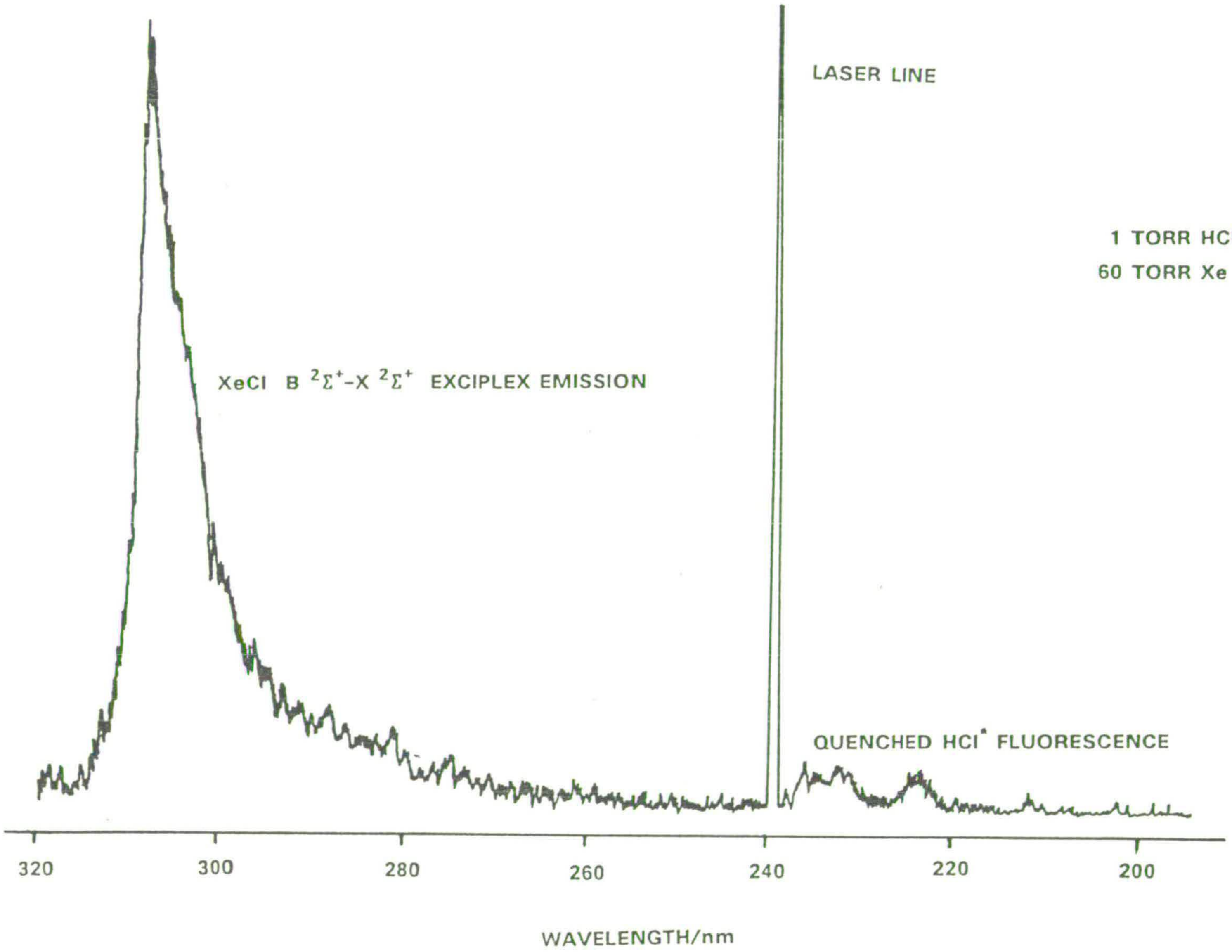

FIGURE 6.4 XeCl (B→X) Emission Intensity as a Function of Xenon Pressure

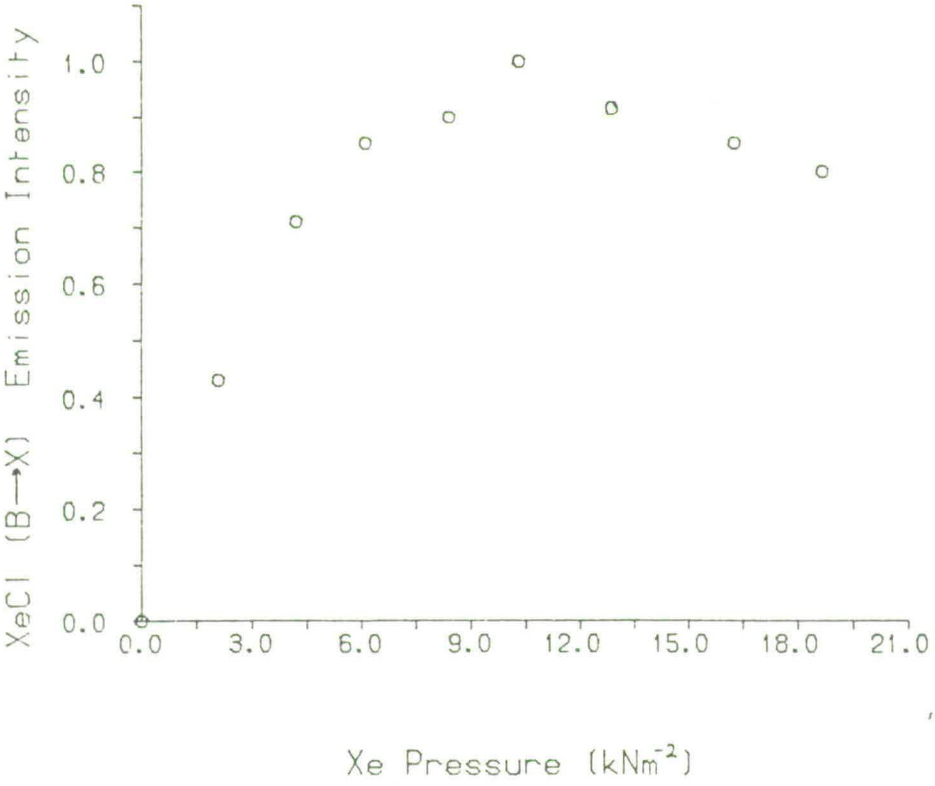

FIGURE 6.5 XeCl* exciplex excitation (action) spectrum.

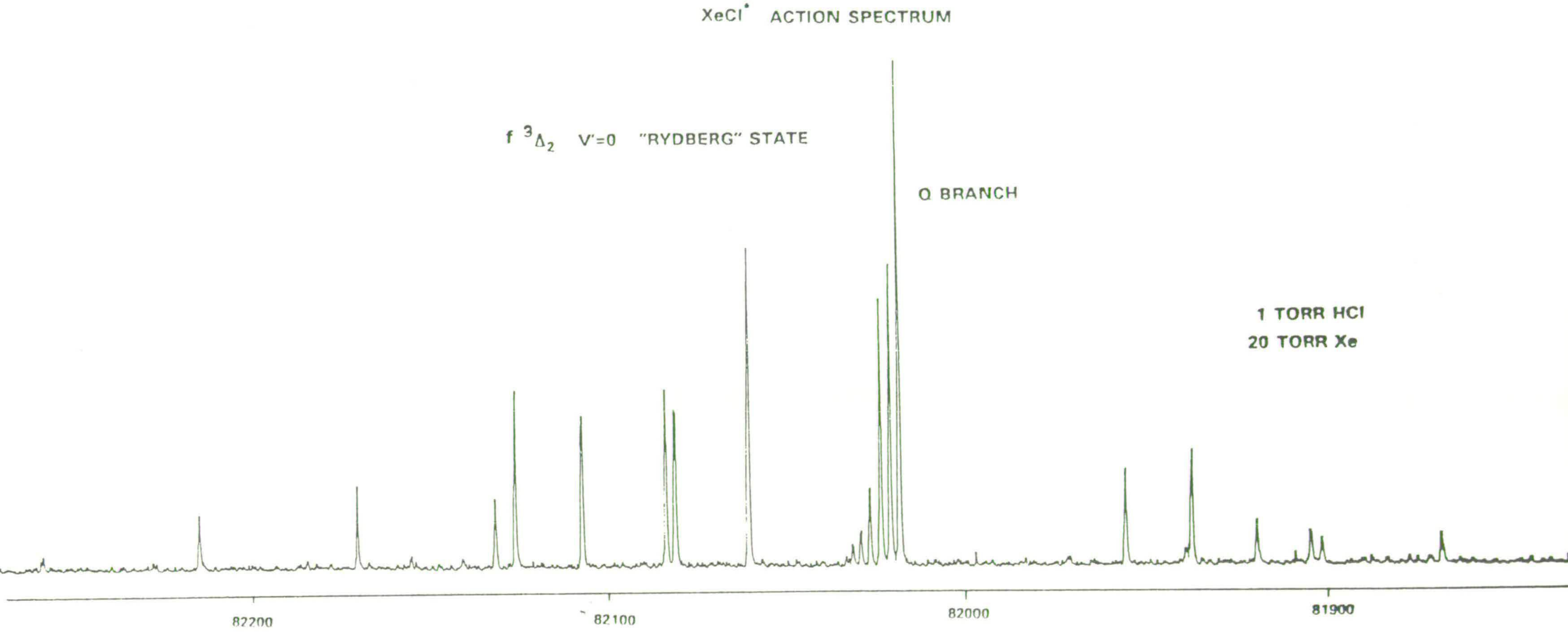

relative efficiency of exciplex formation due to 'Rydberg' or 'Ion-pair' state reaction. One might intuitively expect the 'Ion-pair' state to be more efficient. Note that collisional transfer from the 'Rydberg' states into the 'Ion-pair' manifold appears to be minimal because no characteristic 230nm emission is seen when either the f $^3\Delta_2$ or the F $^1\Delta_2$ state is excited in the presence of He, Ne, Ar, or CH_4 at a variety of pressures. Electronic quenching of the 'Rydberg' state appears to dominate over any other excited state loss process.

The reaction:

$$HCl + Kr \longrightarrow KrCl^*(B\,^2\Sigma^+) + H \qquad 6.2$$

has an energy threshold of 10.02eV. Two-photon excitation of HCl above this threshold in the presence of Kr leads to $KrCl^*$ ($B\,^2\Sigma^+$) exciplex formation. A high pressure of Kr is required to quench out the HCl^* emission around 220nm. The characteristic $KrCl^*$ exciplex emission profile is however clear. Figure 6.6 shows the dispersed emission obtained in the 220-240nm region upon excitation of 2 Torr ($266.6Nm^{-2}$) HCl at the E $^1\Sigma^+$ state v' = 0, J' = 3 level in the presence of 60 Torr ($7.999kNm^{-2}$)Kr.

Once again the lowest excited HCl state observed to react is the f $^3\Delta_2$ state. It is unfortunate that the b $^3\pi_i$ (i=0,1,2) and C $^1\pi$ states are so heavily predissociated and also that the Franck-Condon factors between the ground state and vibrational levels below v' = 9 of the 'Ion-pair' state are so low. It would have been

FIGURE 6.6 Dispersed emission spectrum following excitation of the E $^1\Sigma^+$ state of HCl in the presence of 60 Torr of Kr.

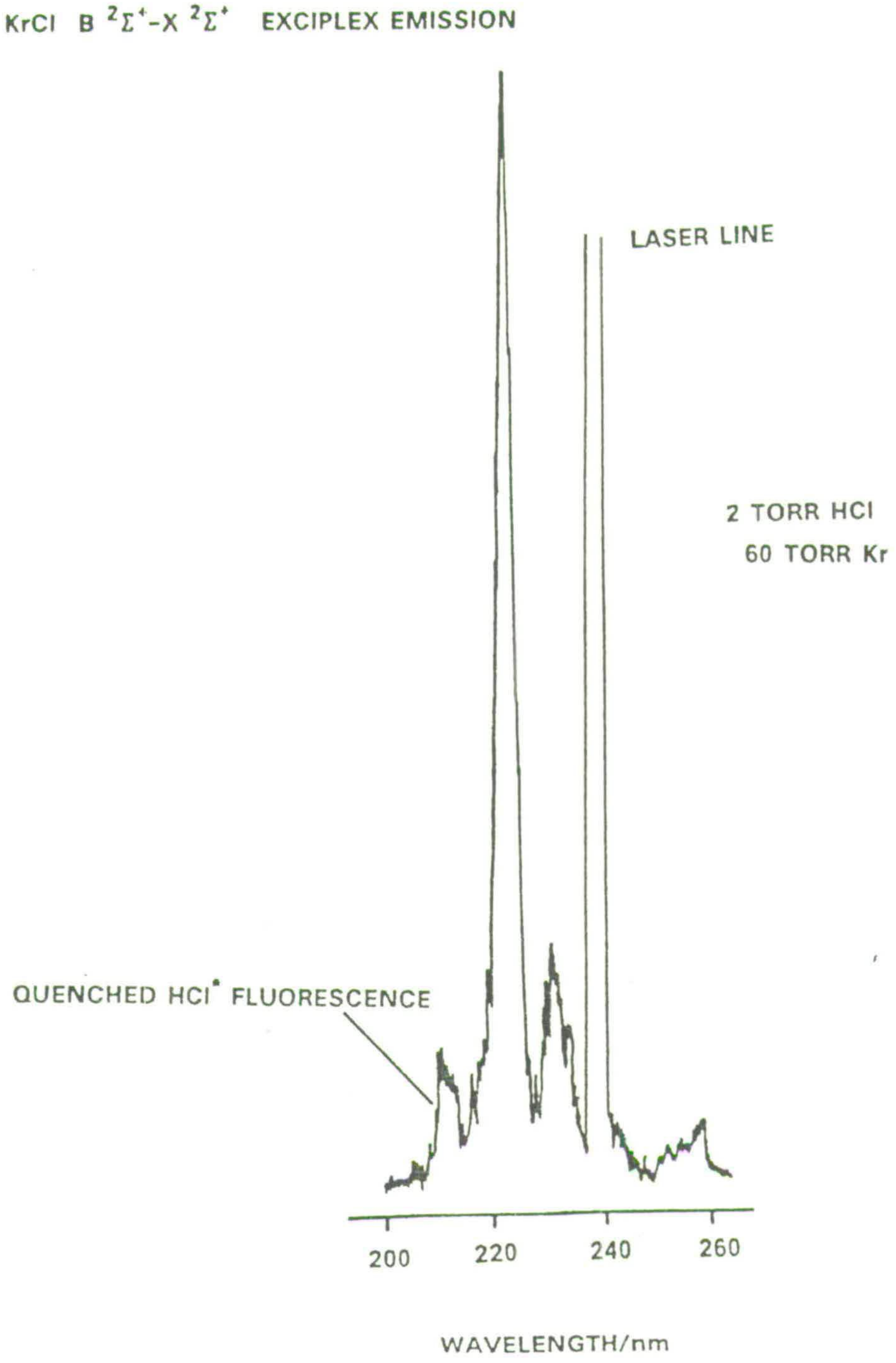

otherwise possible to prepare single ro-vibronic levels of electronic states above and below the $KrCl^*$ exciplex formation-reaction threshold.

6.3 DISCUSSION

It is clear from the results of this work and those of others that irrespective of the initial entrance channel, if the reactants are above the exciplex formation threshold then efficient exciplex formation is likely to result. The reaction model described below is essentially the same whether the initial reactants be electronically excited rare gas atoms (Rg^*) and ground state HCl or electronically excited HCl^* and ground state rare gas atoms (Rg).

In a simple view, the collision pair initially follows the lowest diabatic potential surface, in this case (HCl^*, Rg). This surface crosses the diabatic ionic potential surface (HCl^-,Rg^+) and at this point an electron is transferred from the rare atom Rg to the electronically excited HCl^* (so-called harpooning).

Consider the electronic configurations of excited HCl^*, in the B $^1\Sigma^+$ 'Ion-pair' state and the ground state negative ion (HCl^-) $^2\Sigma^+$ state. The dominant B $^1\Sigma^+$ 'Ion-pair' state configuration is $(5\sigma 2\pi^4)\,6\sigma^*$ (see Chapter 4). On harpooning, the electron from the rare gas atom enters the vacant 5σ orbital on the HCl to produce HCl^- with configuration $(5\sigma^2 2\pi^4)6\sigma^*$. In the presence of the rare gas positive ion, Rg^+, the HCl^- rapidly dissociates and the product exciplex Rg^+Cl^- is formed. In this model the electron is transferred to the chlorine atom which results in a repulsive interaction breaking the molecular bond with the H and Cl^- separating rapidly to a distance beyond which no further force acts between the Cl^- and the H atom. The H atom, thus, acts as a spectator and the Rg^+Cl^- exciplex should have a large fraction of the total energy available deposited into its internal energy.

Consider then the B $^1\Sigma^+$ 'Ion-pair' state. From the calculated potential surfaces for HCl^- [21] the vertical electron affinity of the B $^1\Sigma^+$ state, v' = 0 vibrational level, at the equilibrium bond length of 2.5 Å is $\sim$8.5 eV. With the xenon ionisation potential at 12.127 eV ($Xe^+\ ^2P_{\frac{3}{2}}$) [10] this places the (HCl^*,Xe) covalent surface $\sim$3.5 eV below the ionic ($Xe^+(^2P_{\frac{3}{2}})$, $HCl^-(^2\Sigma^+)$) potential surface.

According to Zare et al [23] an estimate of the electron jump crossing radius (S) may be calculated from the well known formula:

$$S \text{ (in Å)} = 14.35/[\text{I.P.}(Rg) - \text{E.A.}(HCl^*;r)] \qquad 6.3$$

Where I.P. (Rg) is the ionisation potential in eV of the rare gas atom and E.A. (HCl^*;r) is the vertical electron affinity in eV of the electronically excited HCl^* at the internuclear separation r. The vertical electron affinity of the electronically excited HCl^* will generally vary with its bond length, r. Therefore, the magnitude of the crossing radius for an individual reactive trajectory will be a function of r. From equation 6.3, an estimated crossing radius S_e at the equilibrium bond length, of 4.1 Å is obtained. The crossing radius for the equilibrium bond length can be used to estimate the total reaction cross section $\sigma = \pi (S_e)^2$, which in this case is $\sim$50 Å^2. Comparison of this with an empirically determined value can serve as a useful gauge of the applicability of the electron-jump mechanism.

From the model of Zare et al [23], the repulsive energy release in HCl^- on the electron jump is dependent on the nature of the electronically excited HCl^* and HCl^- potential energy surfaces. Note that the calculated HCl^- $(^2\Sigma^+)$ ground state surface shows a nearly flat limb extending from about 1.6 Å towards the dissociation limit, ground state H and Cl^-. Therefore due to the large internuclear separation of the excited 'Ion-pair' state, the crossing between the covalent and ionic surfaces and concommitant electron jump should lead to near-zero relative kinetic energy of the dissociating H and Cl^-. This then, of course, suggests that a very substantial fraction of the available energy may be disposed as internal energy excitation of the Rg^+Cl^- exciplex.

Figure 6.7 shows schematic potential energy surfaces for the reactions $Xe^* + HCl$ and $HCl^* + Xe$. It illustrates in a qualitative manner various reagent entrance and product exit channels that can be coupled via the Xe^+ $(^2P_{\frac{3}{2}})$, $HCl^-(^2\Sigma^+)$ ionic surface.

In the case of the $HCl^* + Xe$ reaction,

FIGURE 6.7 Schematic potential energy surfaces for the reaction Xe* + HCl and HCl* + Xe.

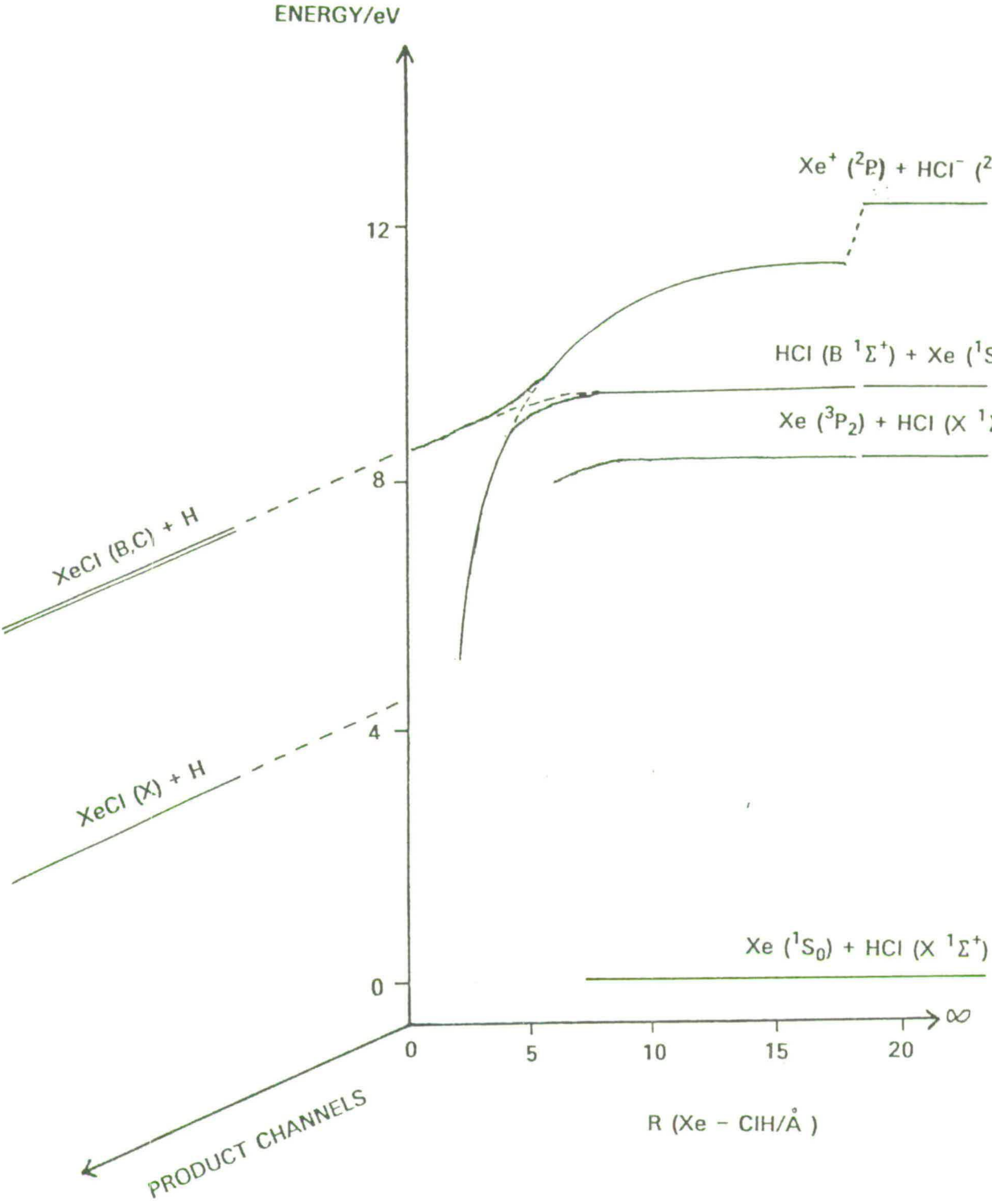

predominantly XeCl (B $^2\Sigma^+$) appeared to be formed. A similar result was observed by Ku and Setser [2] for the reaction of Xe* (6p) with HCl. Collisional coupling of the (B) and (C) states of the XeCl* exciplex will always occur and its importance has been well recognised [12]. Herein may lie the explanation for the apparent preponderance of XeCl* (B) state formation. Setser et al [12] have shown that XeCl* (B) state has a radiative lifetime of 11.7± 0.5 ns and the XeCl* (C) state a radiative lifetime of 131 ± 10 ns. Using time-resolved measurement techniques described in Chapter 3 the temporal behaviour of the XeCl* (B) state formed by the HCl* + Xe reaction can be studied. An HCl and Xe pressure of 2 Torr (266.6Nm^{-2}) and 5 Torr (666.6Nm^{-2}) respectively, was used. The emission showed a fast decay lasting ~40ns, apparently followed by a slower component lasting a further 120ns. The rise time of the emission was prompt and closely followed the leading edge of the laser pulse. This behaviour was very similar to that seen by Setser et al [12,14] for XeCl* (B) state formation in laser photo-association reactions. They postulated that it was indicative of collisional feeding from the XeCl* (C) state into the almost iso-energetic (B) state. For a given total gas pressure, because of its longer lifetime, more XeCl* (C) state molecules will be collisionally transferred to the (B) state than vice-versa. Hence, as Setser et al [6] pointed out, the relative intensity of the XeCl* (B) state emission, with respect to the (C) state, emission should increase with increasing pressure, to some upper limit. Only at low total gas pressures($\sim$0.1 Torr, 13.33Nm^{-2}) were the nascent $XeCl^*$ (B) and (C) state populations maintained.

In conclusion the results in this chapter have illustrated the possibility of studying reactions of highly excited electronic states of diatomic molecules, in this case HCl, at a state selected level. Indeed, even reactions of excited electronic states of molecular hydrogen with rare gases, leading to rare gas hydride excimer formation, have recently been performed by Zimmerer et al, using tunable synchrotron radiation [24]. Here again initial, single rotation level selection of the diatomic molecule was possible. These experimental results are all the more interesting given that excited state potential energy surface calculations for the H_2^*...rare gas atom systems are feasible [25]. In due course similar calculations of excited HCl^*...rare gas atom potential energy surfaces may well become available.

6.4 REFERENCES

1. K. Johnson, J.P. Simons, P.A. Smith, C. Washington and A. Kvaran, Mol. Phys., 57, 225 (1986).
2. J.K. Ku and D.W. Setser, Appl. Phys. Lett., 48, 689 (1986).
3. D.J. Wren, D.W. Setser and J.K. Ku, J. Phys. Chem., 86, 284 (1982).
4. C.T. Rettner and J.P. Simons, Faraday. Discuss. Chem. Soc., 67, 329 (1979).
5. D.W. Setser, T.D. Dreiling, H.C. Brashears, Jnr., and J.H. Kolts, Faraday. Discuss. Chem. Soc., 67, 255 (1979).
6. J.H. Kolts, J.E. Velazco and D.W. Setser, J. Chem. Phys., 71, 1247 (1979).
7. K. Tamagake, J.H. Kolts and D.W. Setser, J. Chem. Phys., 71, 1264 (1979).
8. J. Balamuta, M.F. Golde and A.M. Moyle, J. Chem. Phys., 82, 3169 (1985).
9. R.S.F. Chang, J. Chem. Phys., 76, 2943 (1982).
10. C.E. Moore in 'Atomic Energy Levels', Nat. Stand. Ref. Data. Ser., Nat. Bur. Stand. (U.S.), 35/Vol III, (1971).
11. M.T. Jones, T.D. Dreiling, D.W. Setser and R.N. McDonald, J. Phys. Chem., 89, 4501 (1985).
12. G. Inoue, J.K. Ku and D.W. Setser, J. Chem. Phys., 80, 6006 (1984).
13. A.W. McCown and J.G. Eden, J. Chem. Phys., 81, 2933 (1984).

14. J.K. Ku, G. Inoue and D.W. Setser, J. Phys. Chem., 87, 2989 (1983).

15. H.F. Grieneisen, H. Xue-Jing and K.L. Kompa, Chem. Phys. Lett., 82, 421 (1981).

16. M. Boivineau, J. Le Calvé, M.C. Castex and C. Jouvet, Chem. Phys. Lett., 128, 528 (1986).

17. M. Boivineau, J. Le Calvé, M.C. Castex and C. Jouvet, Chem. Phys. Lett., 130, 208 (1986).

18. T. Ishiwata, A. Tokunaga and I. Tanaka, Chem. Phys. Lett., 112, 356 (1984).

19. M.C. Castex, J. Le Calvé, D. Haaks, B. Jordan and G. Zimmerer, Chem. Phys. Lett., 70, 106 (1980).

20. J.P.T. Wilkinson, E.A. Kerr, K.P. Lawley, R.J. Donovan, D. Shaw, A. Hopkirk and I. Munro, Chem. Phys. Lett., 130, 213 (1986).

21. H.S. Taylor, E. Goldstein and G.A. Segal, J. Phys. B: Atom. Molec. Phys., 10, 2253 (1977).

22. E.F. van Dishoek, M.C. van Hemert and A. Dalgarno, J. Chem. Phys., 77, 3693 (1982).

23. M.G. Prisant, C.T. Rettner and R.N. Zare, J. Chem. Phys., 81, 2699 (1984).

24. T. Möller, M. Beland and G. Zimmerer, Phys. Rev. Lett., 55, 2145 (1985).

25. J. Römelt, S.D. Peyerimhoff and R.J. Buenker, Chem. Phys., 41, 133 (1979).

CHAPTER 7

MULTIPHOTON DISSOCIATION OF C_2H_3Cl AND C_2H_3Br - A PHOTOCHEMICAL SOURCE OF $B^1\Sigma^+$ HCl and HBr, RESPECTIVELY

7.1 INTRODUCTION

Multiphoton dissociation of polyatomic molecules using high power excimer lasers is now an established technique for producing electronically excited and ground state species for subsequent spectroscopic or kinetic study [1-3]. The excitation mechanisms involved in these multiphoton dissociation processes can be identified with three cases:

(1) Simultaneous excitation of the parent molecule via a virtual electronic state or states.

(2) Sequential or multiple-photon excitation of the parent molecule via a real intermediate state or states.

(3) Stepwise dissociative excitation processes via an intermediate fragment or fragments.

A crucial question in regard to the multiphoton dissociation of polyatomic molecules is to specify which one of these mechanisms dominates. Generally, answers have remained inconclusive because little is known about the relevant intermediate species, the quantum states in which they are populated and how they act as intermediates. The formation of $B\ ^1\Sigma^+$ HCl or $B\ ^1\Sigma^+$ HBr 'Ion-pair' states and other photo-fragments following multiphoton dissociation of C_2H_3Cl or C_2H_3Br with an ArF

(193.3nm) excimer laser illustrates the above points.

7.2 DISCUSSION

The photo-excitation of chloroethenes in the UV and VUV has been extensively studied [4-8] in the past. Among the most recent and pertinent studies are the following. Translational energy release in chloroethene fragmentation upon photodissociation at 193nm (ArF laser) by Umemoto et al [8]. The infra-red emission studies of chloroethene photo-fragments again following 193nm excitation by Moss et al [7]. Vibrationally excited HCl photo-fragment emission, following photodissociation of C_2H_3Cl, has been studied by Berry using HCl laser gain measurements [6] and also by Donaldson and Leone [9] using Fourier-Transform Infra-Red (FTIR) techniques coupled to a high repetition rate (400Hz) ArF laser.

Some multiphoton dissociation studies of chloroethenes using an ArF laser have been performed [5,10] and emission from electronically excited species has been observed. Particularly noticeable in this latter instance was the strong emission around 230nm which has been assigned to fluorescence from low vibrational levels in the B $^1\Sigma^+$ 'Ion-pair' state of HCl to high vibrational levels in the ground state [10]. Most recently, multiphoton ionisation of chloroethene (C_2H_3Cl) at 193nm in a time-of-flight mass spectrometer has been performed [11]. At low laser power density (an unfocussed beam) only HCl^+ ions were detectable.

According to Umemoto et al, the two primary pathways of chloroethene fragmentation at 193.3nm are as follows:-

$$C_2H_3Cl \xrightarrow[193\ nm]{h\nu} C_2H_2^{\ddagger} + HCl^{\ddagger} \qquad 7.1$$

$$C_2H_3Cl \xrightarrow[193\ nm]{h\nu} C_2H_3^{\ddagger} + Cl^{\bullet} \qquad 7.2$$

where ‡ implies a vibrationally excited moiety.

Chlorine atom rejection (reaction 7.2) occurs by transition from the initially pumped (π,π^*) state to a dissociative (n,σ^*) state whose potential energy surface crosses that of the (π,π^*) state in the C-Cl co-ordinate. From the (n,σ^*) state the molecule dissociates to a $Cl^{\bullet}$ atom and a $C_2H_3^{\bullet}$ radical. The HCl elimination (reaction 7.1) is likely to occur by an internal conversion to vibrationally excited levels of a low lying state, probably the (π,σ^*) state. From here the transition to highly vibrationally excited levels in the ground electronic state occurs and this carries the C_2H_3Cl molecule to the transition state for HCl elimination. Recent measurements by Rossi and Helm [11] suggest a branching ratio for reactions 7.1 and 7.2 of 67:33. This can be usefully compared to the result of Umemoto et al [8] who quote a ratio of 47:53. The formation of vibrationally excited HCl by reaction 7.1 is of particular importance in understanding subsequent events due to multiphoton absorption.

7.3 RESULTS

7.3.1 PHOTO-FRAGMENT EMISSIONS FOLLOWING MULTIPHOTON DISSOCIATION OF C_2H_3Cl AT 193 nm

The formation of B $^1\Sigma^+$ 'Ion-pair' state HCl via reaction 7.3:

$$C_2H_3Cl \xrightarrow[193nm]{2h\nu} C_2H_2 + HCl(B'\Sigma^+) \qquad 7.3$$

has an energy threshold of ~10.5 eV and thus a minimum of two ArF (6.41eV) photons are required. (The necessary thermochemical data can be obtained from JANAF tables [12].) Following excitation of a low pressure of C_2H_3Cl (50 mTorr, $6.66Nm^{-2}$) with an unfocussed ArF laser, delivering ~50mJ per pulse, very weak emission around 230nm was observed. This corresponded to the B $^1\Sigma^+$ - X $^1\Sigma^+$ transition in HCl. No other emission could be observed in the 200nm-700nm wavelength range. Low resolution spectra over extended wavelength ranges were performed using the Jarell-Ash Monospec 27 spectrometer in conjunction with the Optical Multi-channel Analyser (OMA). The C_2H_3Cl was slowly flowed through the fluorescence cell so as to reduce the build-up of photolysis products. Particularly noticeable was the rapid build-up of a brown polymeric material on the entrance window where the laser beam entered the fluorescence cell. This necessitated frequent window removal and cleaning. Mildly focussing the laser with a 25cm or 50cm focal length lens considerably increased the emission intensity around 230nm. The emission was viewed about 1cm away from the tightly focussed region. Figure 7.1 shows the dispersed emission recorded between 198nm and 242nm. The spectrum, at a resolution of ~0.15nm f.w.h.m., was averaged over 200 laser pulses on the OMA detector head attached to the Monospek 1000 spectrometer. Tentative spectral assignments were made by calculating the positions of various band origins as shown. Under these focussed beam conditions a variety of other electronically excited photo-fragment emissions were seen, particularly C_2^* and CH^*. Intense C_2^* (d $^3\pi_g$ - a $^3\pi_u$) Swan band emission in the region 460-525nm was observed. Also prominent was CH^* (A $^2\Delta$- X $^2\pi$) emission around 430nm. Martin et al [5], who also excited C_2H_3Cl with a focussed ArF laser, have suggested a plausible formation mechanism for C_2^* (d $^3\pi_g$) via the bent di-radical $H\text{-}\dot{C}\text{-}\dot{C}\text{-}H$ or the vinylidencarbene $:C{=}CH_2$ radical by spin-forbidden and spin-allowed processes following subsequent photon absorption. The formation of CH^*A $^2\Delta$ will again involve some high order multiphoton process.

Time-resolved studies of the C_2^* d $^3\pi_g$ and CH A $^2\Delta$ emissions were performed, as described in Chapter 3, either by viewing the emissions directly on a fast oscillocope or by using a Gould Biomation 8100 transient digitiser interfaced to an Apple II microcomputer. For C_2^* d $^3\pi_g$ - a $^3\pi_u$ emission, the (0-0) transition was observed around 516.5nm. At a C_2H_3Cl pressure of 10 mTorr ($1.33Nm^{-2}$) the C_2^* emission intensity rose as fast

FIGURE 7.1 Dispersed emission following excitation of 50 mTorr of C_2H_3Cl using a focussed ArF laser.

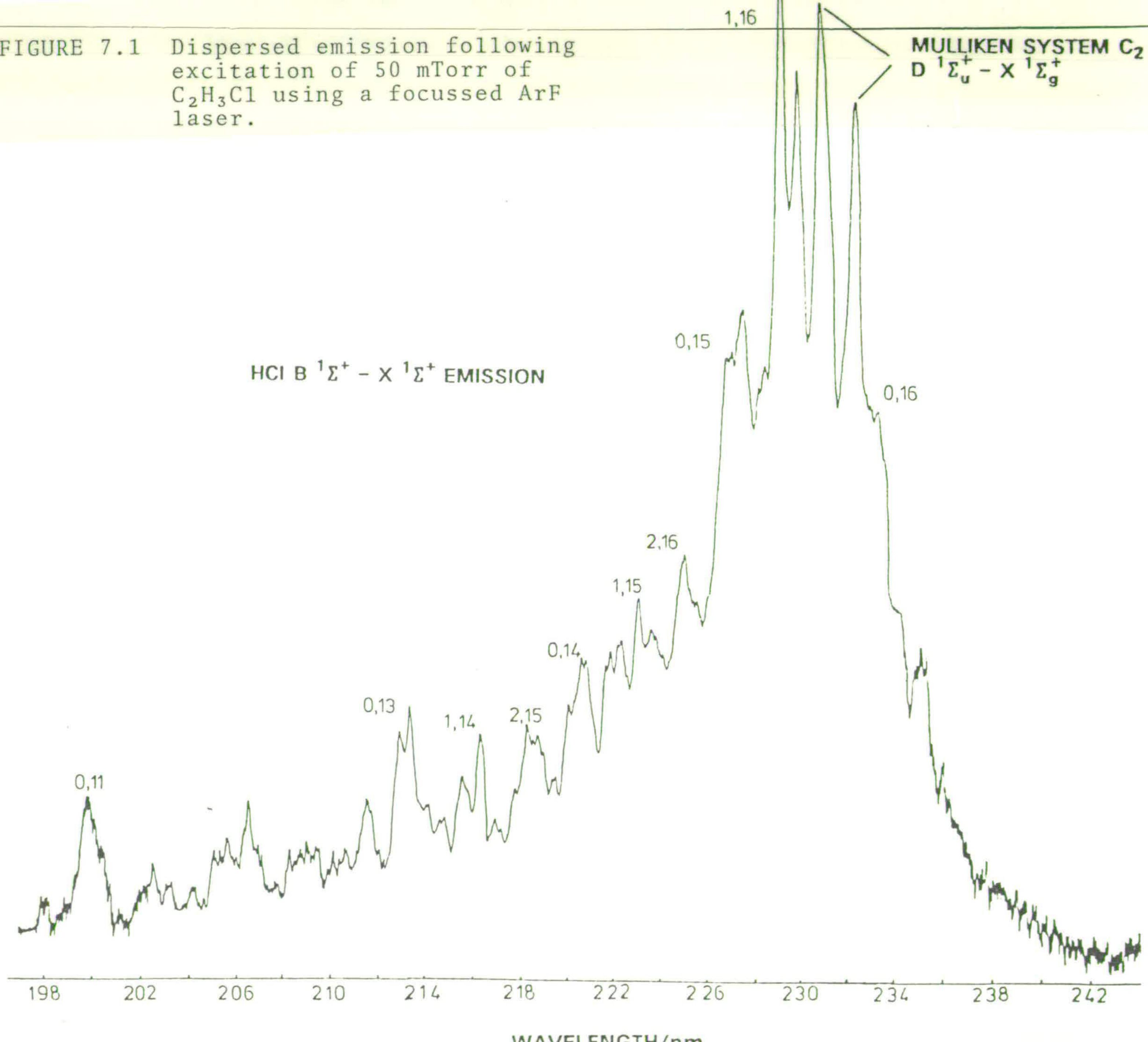

as the laser pulse and decayed exponentially with a radiative lifetime of 120 ± 10ns. This compares favourably with that measured by McDonald et al [13] who obtained a zero pressure, extrapolated value of 119 ± 6 ns for the radiative lifetime. For CH^*, the $A\ ^2\Delta - X\ ^2\pi$ emission was observed around the Q head of the (0-0) transition at 431.5nm. Again the emission signal rose with the duration of the laser pulse (~15ns) and then decayed exponentially. At 10 mTorr ($1.33Nm^{-2}$) pressure of C_2H_3Cl the radiative lifetime of the CH^* A state was determined to be 540 ± 10ns. This is in good agreement with the reported natural radiative lifetime, 534 ± 11ns [14] and that obtained recently (543±10ns) via multiphoton dissociation of $(CH_3)_2CO$ by Nagata et al [1]. Time resolved studies of the HCl^* $B\ ^1\Sigma^+ - X\ ^1\Sigma^+$ emission around 230nm showed that the $B\ ^1\Sigma^+$ 'Ion-pair' state fluorescence essentially followed the time profile of the laser pulse. This confirms the observation made in Chapter 6 and suggests a radiative lifetime of a few nanoseconds for the 'Ion-pair' state. From these measurements one may conclude that C_2^* $d\ ^3\pi_g$, CH^* $A\ ^2\Delta$ and HCl^* $B\ ^1\Sigma^+$ states are primary, nascent products of the photodissociation.

The power dependence of the $B\ ^1\Sigma^+$ HCl^* emission (with the beam focussed by a 25cm lens) was measured and was found to be linear over the laser pulse energy range 1-15mJ (see Figure 7.2). Chloroethene absorbs 193nm

FIGURE 7.2 $B'\Sigma^+$HCl Emission Intensity as a function of laser energy

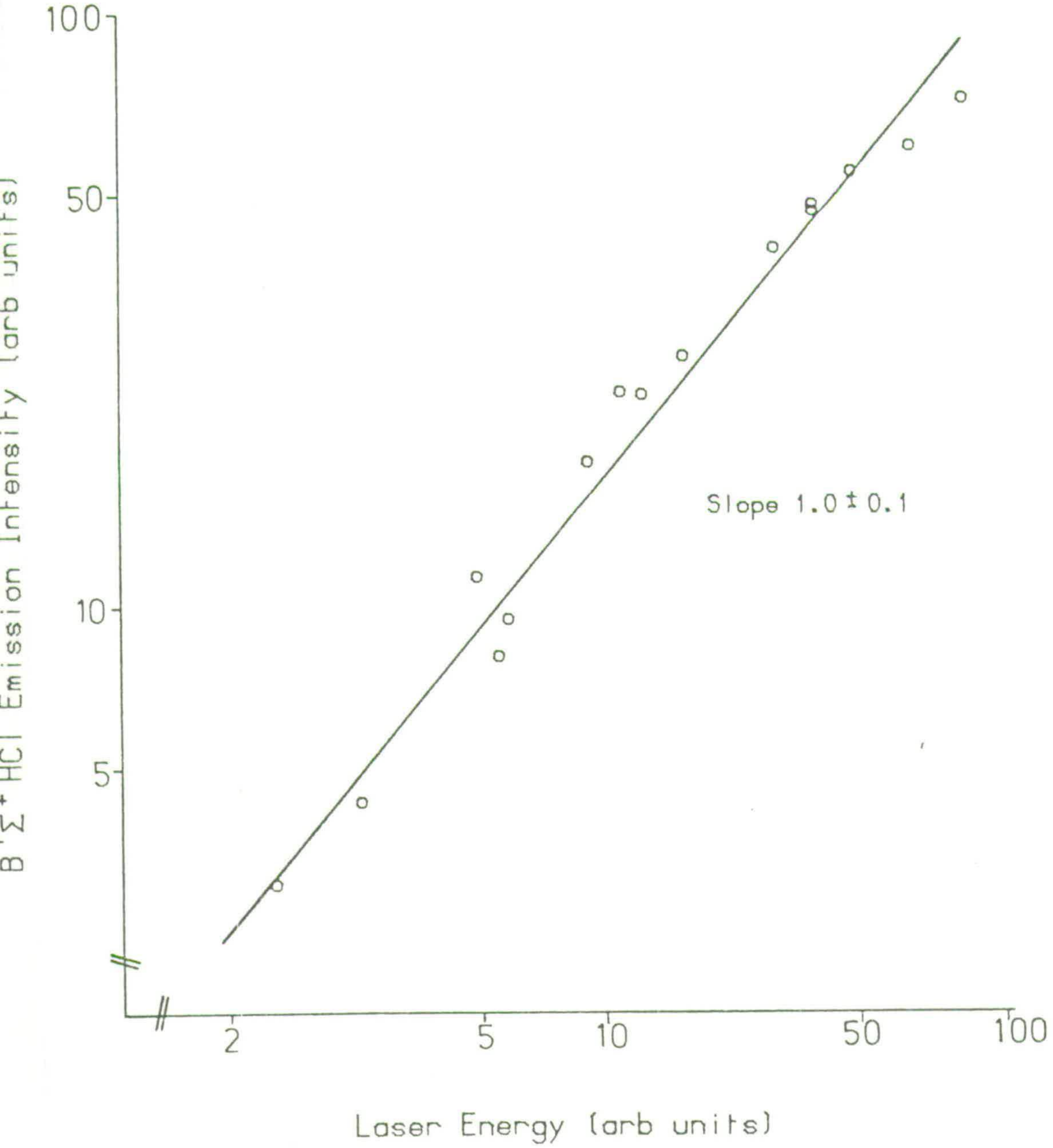

radiation strongly [6] and it is likely that this step is 'kinetically' saturated. Subsequent excitation of the $C_2H_3Cl^*$ to produce a 'superexcited' state $C_2H_3Cl^{**}$ which fragments to give B $^1\Sigma^+$ HCl^* appears unlikely because of the very rapid non-radiative decay (≤1ps) of the initially pumped $C_2H_3Cl^*$ state. Highly vibrationally excited HCl is known to be produced by the single-photon photolysis of C_2H_3Cl at 193nm [6,7,9], however the full quantum state distribution has yet to be measured. The photolysis of chloroethene at 193nm leading to ground state C_2H_2 and HCl is exothermic by 5.39eV [12] and if all of this energy were available to the HCl fragment then there is sufficient to cause dissociation of the molecule. The analysis of Berry [6] suggests that only 180-210kJ mol^{-1} (1.9-2.2eV) (based on the activation energy for thermal decomposition of C_2H_3Cl) are available for vibrational excitation of the HCl. The energy available is that between the crest of the barrier to elimination on the ground state C_2H_3Cl surface and the separated products, C_2H_2 and HCl. The observed HCl vibrational distribution is however considerably more excited than would be obtained assuming this amount of available energy. Recently, Donaldson and Leone [9] have performed a modified statistical calculation which produces results more closely matching the observed HCl vibrational distribution and predict significant population of vibrational levels $v'' > 4$. If there is significant population in higher vibrational levels, i.e.

v" = 10, 11, ... then these can be pumped with a 193nm photon into the B $^1\Sigma^+$ 'Ion-pair' state (see Figure 7.3). The one-photon power dependence of the B $^1\Sigma^+$ emission intensity is then a manifestation of this rate determining step.

Recently, Stuhl et al [15] have postulated an identical model to explain the B $^1\Sigma^+$ HCl^* emission observed following multiphoton excitation at 193nm of $CHCl_3$ or CH_2Cl_2. Vibrationally excited HCl was produced following absorption of a 193nm photon by the parent $CHCl_3$ or CH_2Cl_2 molecule. A second 193nm photon in the same laser pulse excited the vibrationally hot HCl into the B $^1\Sigma^+$ 'Ion-pair' state. The multiphoton ionisation of C_2H_3Cl, at 193nm, which according to Rossi and Helm [11], produced predominantly HCl^+ and Cl^+ ions and no parent $C_2H_3Cl^+$ ions when a focussed laser beam was used, required a similar mechanism whereby vibrationally hot HCl in its ground state was pumped via an excited electronic state (the 'Ion-pair' state) to the ionisation continuum.

The formation of B $^1\Sigma^+$ HBr following multiphoton dissociation of C_2H_3Br must follow a similar process to that cited above for B $^1\Sigma^+$ HCl formation. Figure 7.4 shows the observed HBr B $^1\Sigma^+$ emission produced following photolysis of C_2H_3Br at 193nm. The spectrum was recorded in a similar manner to that of the HCl case. The B $^1\Sigma^+$ state in HBr still remains poorly characterised. Discharge excited emission of the B $^1\Sigma^+$ - X $^1\Sigma^+$ system has been studied [16], however the electronic origin and

FIGURE 7.3

HCl $X^1\Sigma^+$ ground and $B^1\Sigma^+$ ion-pair states

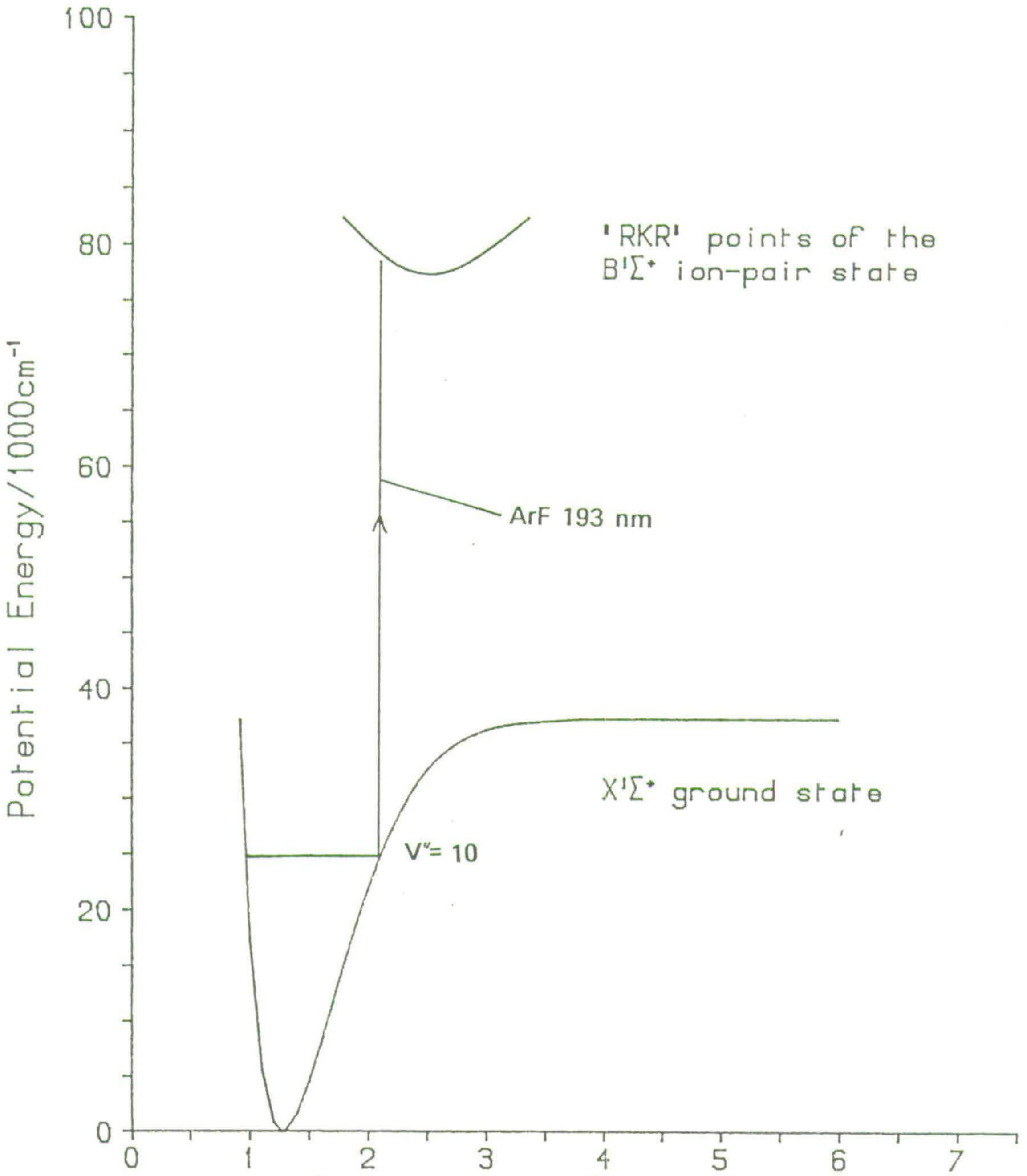

FIGURE 7.4 Dispersed emission following excitation of 50 mTorr of C_2H_3Br using a focussed ArF laser.

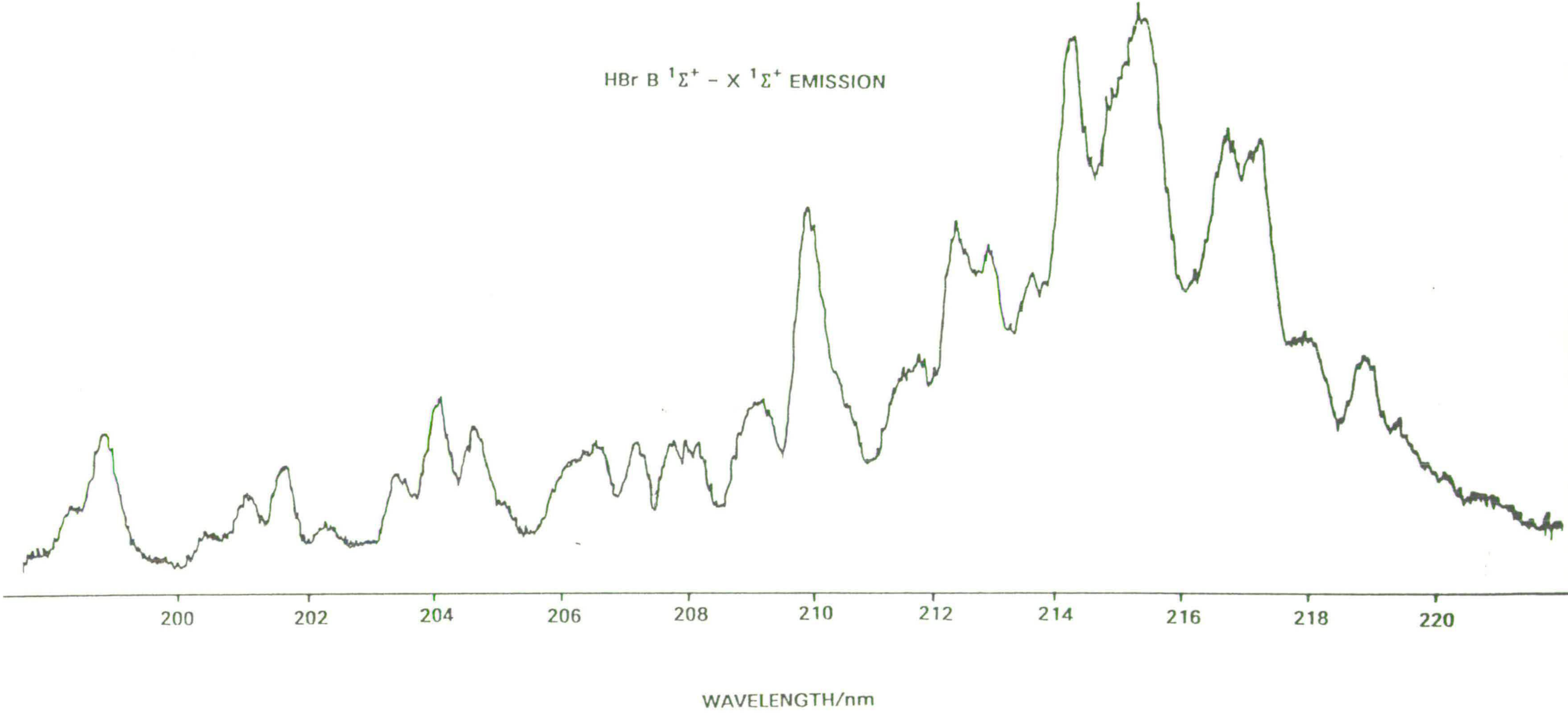

vibrational numbering of the state have yet to be properly determined [16,17].

7.3.2 REACTIONS AND QUENCHING OF HCl^* AND HBr^* 'ION-PAIR' STATES WITH RARE GASES.

The multiphoton dissociation of C_2H_3Cl and C_2H_3Br at 193nm is an efficient and convenient way to prepare B $^1\Sigma^+$ 'Ion-pair' state HCl and HBr in low vibrational levels of the respective states.

The addition of rare gases produced a dramatic effect on the HCl^* and HBr^* emission intensity. In both cases quenching of the fluorescence was observed. An analysis of the integrated fluorescence as a function of rare gas pressure was performed. Inherent in the analysis was the assumption that the electronically excited HCl^* (or HBr^*) + rare gas collision system could be modelled by the Stern-Volmer relation:

$$\frac{I_o}{I_Q} = \frac{k_Q}{k_f}[Q] \qquad 7.4$$

where [Q] is the pressure of the rare gas.

I_o is the HCl^* or HBr^* emission intensity in the absence of quenching gas.

I_Q is the HCl^* or HBr^* emission intensity at the quenching gas pressure [Q].

k_f is the HCl^* or HBr^* radiative lifetime.

k_Q is the desired HCl^* or HBr^* total removal rate.

At a given rare gas pressure the HCl^* emission intensity, following photolysis of 80 mTorr ($10.66Nm^{-2}$) of C_2H_3Cl

at 193nm, was integrated on the OMA detector head for 10-20 laser shots. The powerful data handling routines in the OMA III system allowed the total HCl^* integrated emission intensity to be calculated at each quenching gas pressure. Figure 7.5 shows the Stern-Volmer plot for the quenching of $B\ ^1\Sigma^+$ HCl by helium (He). Good linear behaviour was observed suggesting that the above assumptions were reasonable. From the observed slope of the graph the total removal rate, assuming a radiative lifetime of 5ns, was $1.04 \pm 0.12 \times 10^{-10}\ cm^3\ molecule^{-1} s^{-1}$. The lifetime of the $B\ ^1\Sigma^+$ state of HCl has been theoretically calculated to be 2-4ns [18]. For quenching by Ar and Xe, again using a 5ns radiative lifetime, a removal rate of $3.4 \pm 0.2 \times 10^{-10}\ cm^3\ molecule^{-1}\ s^{-1}$ and $3.6 \pm 0.2 \times 10^{-10}\ cm^3\ molecule^{-1}\ s^{-1}$, respectively, were determined. Again, good Stern-Volmer behaviour was observed. In the presence of Xe strong $XeCl^*$ B - X exciplex emission was observed, as expected, thus confirming the results of Martin et al [10]. The power dependence of the $XeCl^*$ B - X emission intensity was observed to be close to one, see Figure 7.6. Again the laser energy was varied between ~1 and ~15mJ with the beam focussed with a 25cm focal length lens. In addition the attenuation of the $XeCl^*$ exciplex emission intensity closely followed that of the excited HCl^* emission intensity, as a function of added Ar buffer gas, see Figure 7.7. This experiment was performed by irradiating at 193nm a mixture of C_2H_3Cl (80 mTorr, $10.66Nm^{-2}$) in Xe

FIGURE 7.5 Stern Volmer plot for quenching of HCl ($B'\Sigma^+$) by Helium

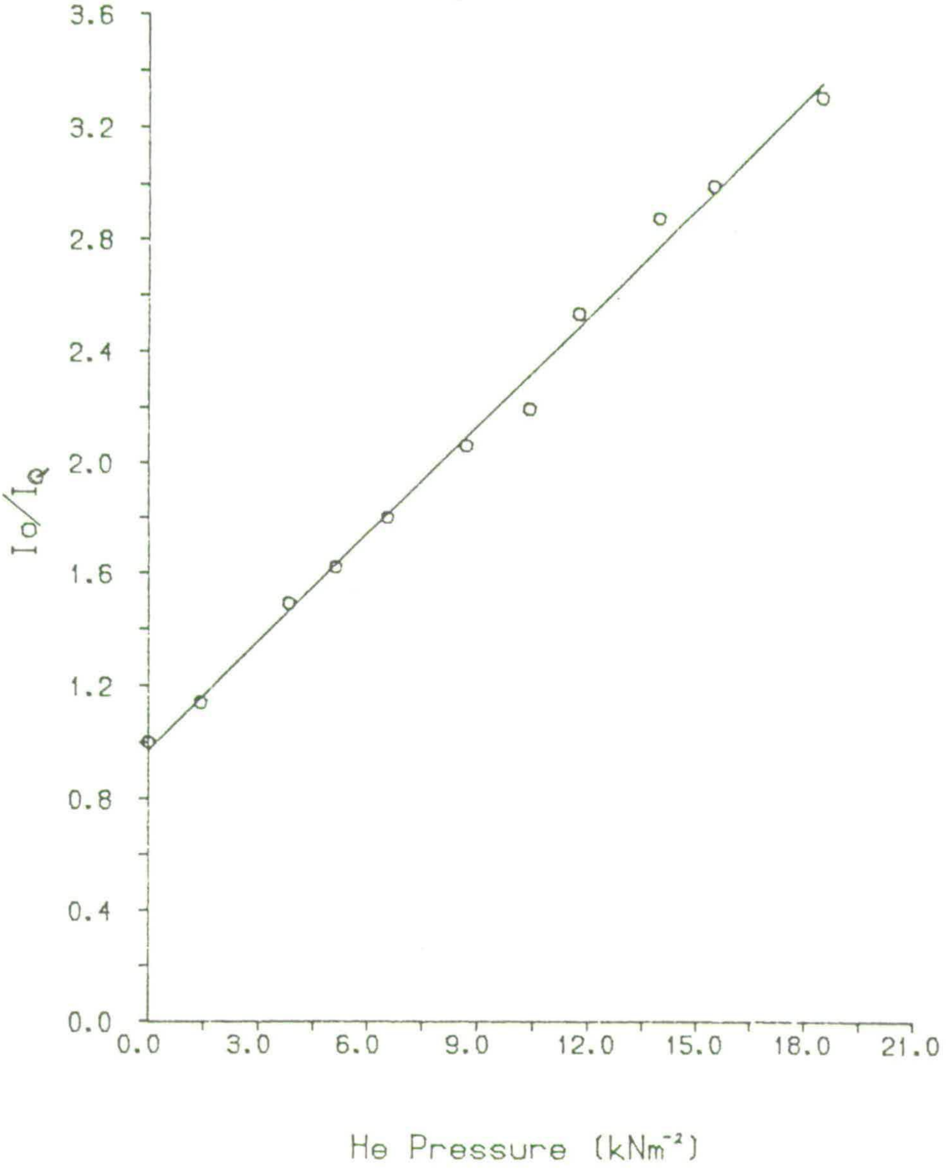

FIGURE 7.6 XeCl (B→X) Emission Intensity as function of laser energy

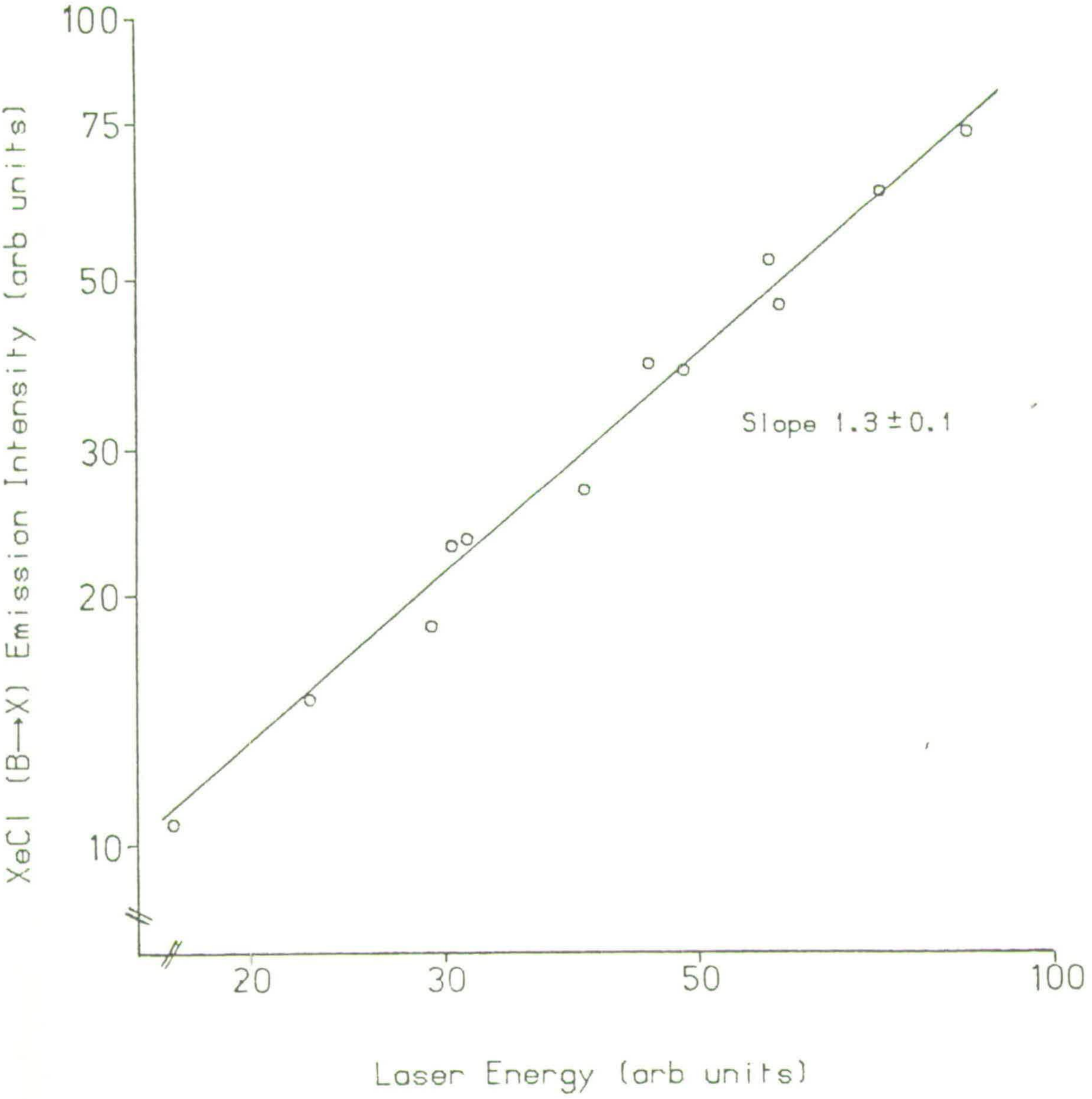

FIGURE 7.7 XeCl $(B \rightarrow X)$ and $B'\Sigma^{+}$ HCl emission intensity as a function of argon pressure

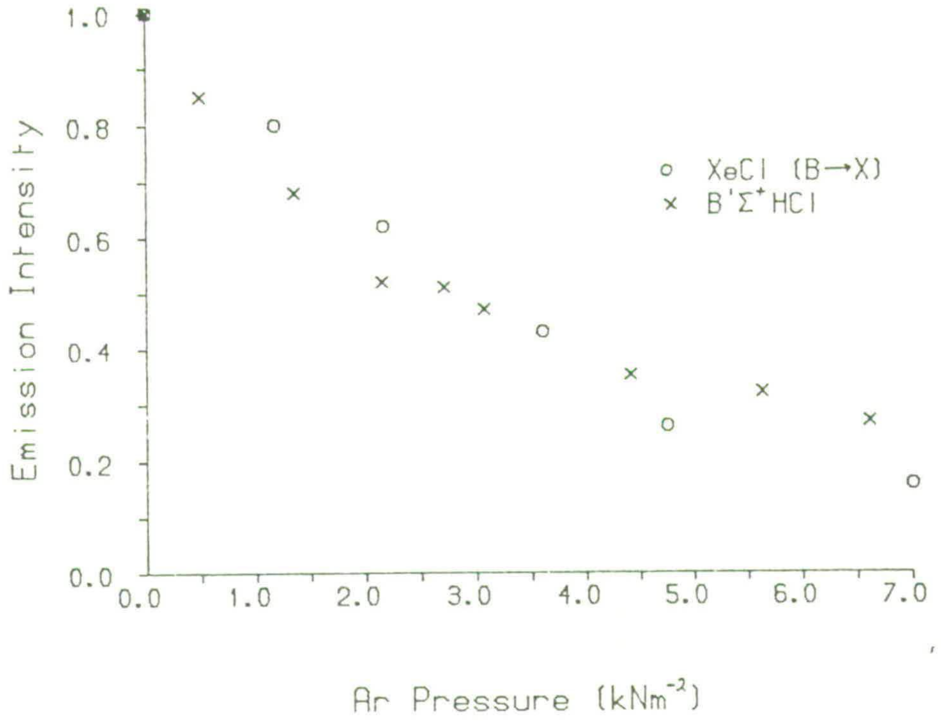

(20 Torr, 2.66kNm^{-2}) and adding Ar buffer gas up to a pressure of ~55 Torr (7.33kNm^{-2}). Both these observations suggest strongly that it is the excited B $^1\Sigma^+$ HCl* molecule that is reacting with ground state Xe to form the XeCl* exciplex.

With Kr present no KrCl* exciplex emission around 222 nm was seen. This was hardly surprising considering that the excited HCl* was being prepared in vibrational levels below the exciplex formation threshold. Strong XeBr* B - X exciplex emission around 282nm was seen when B $^1\Sigma^+$ HBr was formed via photolysis of C_2H_3Br (80 mTorr, 10.66Nm^{-2}) at 193nm in the presence of Xe (30 Torr, 3.99kNm^{-2}), see Figure 7.8. The reaction:

$$HBr + Xe \longrightarrow XeBr\ (B^2\Sigma^+) + H \qquad 7.5$$

has an energy threshold of ~8.16 eV. Thus formation of B $^1\Sigma^+$ HBr* with ~9.3 eV of energy [16] provides an energy excess for exciplex formation and hence reaction proceeds. In the presence of rare gases the B $^1\Sigma^+$ HBr* emission quenches with an efficiency comparable to that of B $^1\Sigma^+$ HCl*.

The above tentative quenching rates for electronically excited HCl* are typical for the total removal rates of 'Ion-pair' state molecules [19-23]. They can be usefully compared to data on the removal of electronically excited Xe by ground state HCl. For Xe*($6s^3P_2$) a quenching rate of 5.6×10^{-10} cm^3 molecule^{-1} s^{-1} was measured [24]. The Xe*(6p) excited states quenched at a typical rate of 8.0×10^{-10} cm^3 molecule^{-1} s^{-1} [25].

FIGURE 7.8 XeBr* exciplex emission following excitation of C_2H_3Br (80 mTorr) in the presence of Xe (30 Torr).

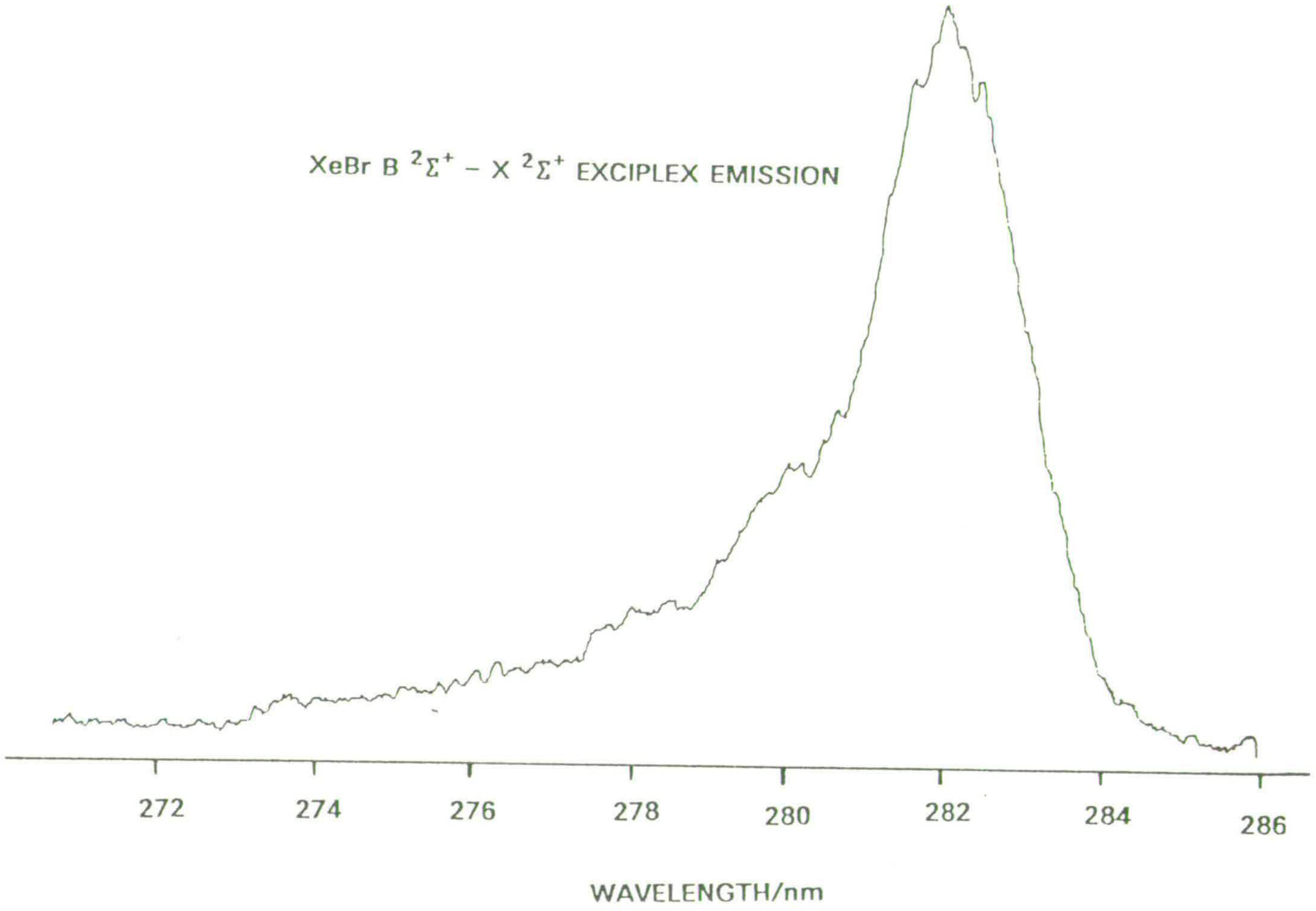

In all cases, whether it be an electronically excited atom or diatomic molecule, the excited state removal rate was very efficient. The dominant reactive channel for electronically excited HCl^* in the presence of Xe and electronically excited $Xe^*(6p)$ states in the presence of HCl (as discussed in Chapter 6) appeared to be that of $XeCl^*$ exciplex formation.

7.4 CONCLUSION

The multiphoton dissociation of C_2H_3Cl or C_2H_3Br with an ArF (193nm) laser has been shown to be a convenient means of preparing HCl or HBr in low vibrational levels of the electronically excited B $^1\Sigma^+$ 'Ion-pair' state. This region of the potential is otherwise experimentally impossible to access because of poor Franck-Condon overlap with the $v'' = 0$ vibrational level of the ground state. Indeed, single-photon dissociation of C_2H_3X (where X=Cl, Br, I or F) followed by excitation of HX using tunable, coherent VUV radiation could provide a tractable, selective route into the lowest vibrational levels of the respective 'Ion-pair' potentials.

The problem of measuring accurately the radiative lifetime of the 'Ion-pair' state, given its apparently short duration (2-4ns[18]), remains a difficult one. At present the limiting factor in this process is the production of the excited state population on a sub-nanosecond time scale. Ideally the radiative lifetime determination should be made by observing fluorescence in a time-resolved manner from vibrational levels at the bottom of the 'Ion-pair' potential. However, direct access from thermally populated levels in the ground state is virtually impossible because of poor Franck-Condon overlap. Two-photon excitation, using tunable UV laser radiation, has been shown in this work to be a feasible means of exciting higher vibrational levels $v'>9$ of the 'Ion-pair' state. However, those levels accessed are badly perturbed and this itself may have some interesting affects on the lifetime.

If direct two-photon excitation of HCl is to be used then intense sub-nanosecond, tunable UV light pulses around 240 nm will be required. This would mean frequency doubling the output of a short pulse dye laser operating in the visible around 480nm. The standard method of obtaining high energy sub-nanosecond pulses is to amplify with a 'Q'-switched Nd:YAG laser the short pulses from a dye laser driven by a mode-locked Argon-ion laser [26]. A cheaper alternative described by Austin and Le Grange [27] uses a sub-nanosecond pulsed laser (e.g. N_2 or XeCl excimer laser) to pump a dye laser, its output is then amplified with a synchronously fired high power Nd:YAG or XeCl excimer laser. With either of the above systems then, typically pulse energies of a few mJ with ~300ps duration in the visible could easily be obtained.

Another alternative method to produce 'Ion-pair' state HCl could be to photolyse C_2H_3Cl with a focussed sub-nanosecond ArF laser, similar to the one described by Rhodes et al [28,29]. Typical output pulse energies of the laser described were 10mJ with a pulse-width of 5 ps.

One approach, not using laser radiation, could be to use pulsed (single-bunch mode) synchrotron radiation to excite HCl fluorescence by single-photon absorption. Operating in this fashion a typical synchrotron [20] could produce a pulse-width of $\sim$200ps at a repetition time of $\sim$320ns. This method has been used successfully to measure the radiative lifetimes of several 'Ion-pair' state molecules [19,20,30]. One can safely predict that in the near future direct, time-resolved lifetimes and quenching rate measurements of highly excited electronic states, such as those found in HCl, will be performed on routine basis.

7.5 REFERENCES

(1) T. Nagata, M. Suzuki, K. Suzuki, T. Kondow and K. Kuchitsu, Chem. Phys., 88, 163 (1984).

(2) C.J. Nokes and R.J. Donovan, Chem. Phys., 90, 167 (1984).

(3) R.J. Donovan in 'Gas Kinetics and Energy Transfer', Specialist Periodical Reports, Vol. 4 p.117 (1981), Royal Society of Chemistry, edited by P.G. Ashmore and R.J. Donovan.

(4) R. Ausubel and M.H.J. Wijnen, J. Photochem., 5, 233 (1976).

(5) M. Castillejo, J.M. Figuera and M. Martin, Chem. Phys. Lett., 107, 561 (1984).

(6) M.J. Berry, J. Chem. Phys., 61, 3114 (1974).

(7) M.G. Moss, M.D. Ensminger and J.D. McDonald, J. Chem. Phys., 74, 6631 (1981).

(8) M. Umemoto, K. Seki, H. Shinohara, U. Nagashima, N. Nishi, M. Kinoshita and R. Shimada, J. Chem. Phys., 83, 1657 (1985).

(9) D.J. Donaldson and S.R. Leone, Chem. Phys. Lett., 132, 240 (1986).

(10) M. Castillejo, J.M. Figuera and M. Martin, Chem. Phys. Lett., 117, 181 (1985).

(11) M.J. Rossi and H. Helm, J. Chem. Phys., 87, 902 (1987).

(12) 'JANAF Thermochemical Tables', Natl. Stand. Ref. Data. Ser. Natl. Bur. Stand. No. 37 (U.S. GPO, Washington D.C., 1971), edited by D.R. Stull and H. Prophet.

(13) J.R. McDonald, A.P. Baronavski and V.M. Donnelly, Chem. Phys., 33, 161 (1978).

(14) J. Brzozwski, P. Bunker, N. Elander and P. Erman, Astrophys. J., 207, 414 (1976).

(15) R.D. Kenner, H.K. Haak and F. Stuhl, J. Chem. Phys., 85, 1915 (1986).

(16) J.G. Stamper and R.F. Barrow, J. Phys. Chem., 65, 250 (1961).

(17) D.S. Ginter and M.L. Ginter, J. Mol. Spectrosc., 90, 152 (1981).

(18) E.F. van Dishoek, M.C. van Hemert and A. Dalgarno, J. Chem. Phys., 77, 3693 (1982).

(19) R.J. Donovan, G. Gilbert, M. MacDonald, J.P.T. Wilkinson, I. Munro and D. Shaw, J. Photochem., 31, 1 (1985).

(20) R.J. Donovan, G. Gilbert, M. MacDonald, I. Munro, D. Shaw and G.R. Mant, Chem. Phys. Lett., 109, 279 (1984).

(21) R.J. Donovan, B.V. O'Grady, L. Lain and C. Fotakis, J. Chem. Phys., 78, 3727 (1983).

(22) T. Ishiwata, A. Tokunaga and I. Tanaka, Chem. Phys. Lett., 112, 356 (1984).

(23) D.J. Kligler, J. Bokor and C.K. Rhodes, Phys. Rev. A., 21, 607 (1980).

(24) J.H. Kolts, J.E. Velazco and D.W. Setser, J. Chem. Phys., 71, 1247 (1979).

(25) J.K. Ku and D.W. Setser, Appl. Phys. Lett., 48, 689 (1986).

(26) R.L. Fork, C.V. Shank and R. Yen, Appl. Phys. Lett., 41, 223 (1982).

(27) R.H. Austin and J.D. LeGrange, Rev. Sci. Instrumen., 56, 630 (1985).

(28) T.S. Luk, H. Egger, W. Muller, H. Pummer and C.K. Rhodes, J. Chem. Phys., 82, 4479 (1985).

(29) H. Egger, T.S. Luk, K. Boyer, D.F. Muller, H. Pummer, T. Srinivasan and C.K. Rhodes, Appl. Phys. Lett., 41, 1032 (1982).

(30) G. Zimmerer , p.357 in 'Photophysics and Photochemistry above 6 eV', edited by F. Lahmani (Elsevier Science Publishers, Amsterdam 1985).

APPENDIX I

TWO-PHOTON ABSORPTION THEORY

For two-photon transitions of a rotating symmetric top molecule with quantum numbers E,V,JKM for the electronic, vibrational, and rotational operators there exists a tensor

$$S(E,V,JKM \longrightarrow E',V',J'\ K'\ M')$$

describing each transition, where the absorptivity δ may be described by the formula:

$$\delta = |\underline{e}_1 . S . \underline{e}_2|^2 \qquad 1.1$$

where $\underline{e}_1$ and $\underline{e}_2$ are the normalised polarisation vectors for the two photons. States which differ only by M or M' are degenerate therefore:

$$\delta(E,V,JKM \longrightarrow E',V',J'\ K'\ M') =$$
$$\sum_{MM'}\sum |\underline{e}_1 . S(E,V,JKM \longrightarrow E',V',J'\ K'\ M') . \underline{e}_2|^2 \qquad 1.2$$

$\underline{e}_1$, $\underline{e}_2$ and S must be expressed in the same coordinate system, which is taken as laboratory co-ordinates.

Thus the two-photon absorption tensor of the rotating molecule in laboratory fixed co-ordinates may be written as:

$$S = \langle JKM|\langle EV|\hat{R}(\omega)\hat{\mathscr{J}}(x,y,z)|E'V'\rangle J'K'M'\rangle \qquad 1.3$$

where $\hat{\mathscr{J}}(x,y,z)$ is the two-photon tensor operator written in internal molecular co-ordinates (x,y,z) and $\hat{R}(\omega)$ is the operator that rotates the frame (x,y,z) into the laboratory frame (X,Y,Z). The relative orientation of the two frames being specified by the three Euler angles (α,β,γ). Equations 1.1-1.3 are valid regardless of whether the vectors and tensors are expressed in Cartesian or in an irreducible representation. The latter is however more useful.

The irreducible representation of the two-photon absorption tensor operator, $\hat{\mathscr{J}}_{jk}$ is given by:

$$\hat{\mathscr{J}}_{jk} = \sum_{\mathscr{J}-\sigma=k} (11jk|1\mathscr{J}1-\sigma)D_{\mathscr{J}A}\hat{\mathscr{J}}_{AB}D_{B,-\sigma} \qquad 1.4$$

where $\hat{\mathscr{J}}_{AB}$ is the two-photon tensor operator in Cartesian co-ordinates. The bracketed quantity is the Clebsch-Gordon coefficient $(j_1j_2jm|j_1m_1j_2m_2)$ with $j_1=j_2=1$ and $m_1=\mathscr{J}$ and $m_2 = -\sigma$. Thus, j and m run over $\{j=0,m=0\}$, $\{j=1,m=-1,0,+1\}$ and $\{j=2,m=-2,-1,0,+1,+2\}$. A and B will run over X, Y and Z while $\mathscr{J}$ and σ run over the 'spherical representation' indices -1, 0, +1. The transformation matrices $D_{\mathscr{J}A}$ and $D_{B,-\sigma}$ are given by McClain and Harris (Chapter 2, reference [4]) equation (96).

The two-photon absorption S_{jm} in irreducible representation, expressed in terms of molecular wave-functions and the Cartesian two-photon operator $\hat{\mathscr{J}}_{AB}$

is given by:

$$S_{jm} = \langle JKM|\langle EV|\sum_{k=-j}^{+j} \mathcal{D}^{j}_{mk}(\omega) \sum_{\mathcal{f}-\sigma=k} (11jk|1\mathcal{f}1-\sigma) \times D_{\mathcal{f}A}\hat{\mathcal{S}}_{AB}D_{B,-\sigma}|E'V'\rangle|J'K'M'\rangle \qquad 1.5$$

where $\mathcal{D}^{j}_{mk}(\omega) = [8\pi^2/(2j+1)]^{\frac{1}{2}}\psi_{jmk}(\omega)$ and $\psi_{jmk}(\omega)$ is the Schrödinger eigenfunction for a symmetric top.

Hence, the irreducible two-photon tensor S_{jm} can be written:

$$S_{jm} = \sum_{k=-j}^{+j} \langle JKM|\mathcal{D}^{j}_{mk}|J'K'M'\rangle \times \langle EV\hat{\mathcal{S}}_{jk}E'V'\rangle \qquad 1.6$$

From McClain and Harris, (Chapter 2, reference [4] equation (103) then

$$\langle JKM|\mathcal{D}^{j}_{mk}|J'K'M'\rangle = [(2J+1)(2J'+1)]^{\frac{1}{2}}(-1)^{M-K} \times \begin{pmatrix} J & j & J' \\ -M & m & M' \end{pmatrix} \begin{pmatrix} J & j & J' \\ -K & k & K' \end{pmatrix} \qquad 1.7$$

Hence, the dependence of the irreducible tensor elements upon rotational quantum number is given by:

$$S_{jm} = (-1)^{M-K}(2J+1)^{\frac{1}{2}}(2J'+1)^{\frac{1}{2}} \begin{pmatrix} J & j & J' \\ -M & m & M' \end{pmatrix} \times \sum_{k=-j}^{+j} \begin{pmatrix} J & j & J' \\ -K & k & K' \end{pmatrix} \mathcal{S}_{jk}(EV \rightarrow E'V') \qquad 1.8$$

where $\mathcal{S}_{jk}$ is the irreducible form of the Cartesian two-photon tensor $\mathcal{S}_{AB}$ for the rotationless vibronic transition EV ⟶ E'V'.

The next step is to construct amplitudes by taking scalar products of these tensors with the polarisation vectors, to square the amplitudes to obtain transition probabilities and finally to sum over the M degeneracies.

In Cartesian terms the probability amplitude

$$A = \underline{e}_{1A} S_{AB} \underline{e}_{2B} = \tau_{AB} S_{AB} \qquad 1.9$$

where $\tau_{AB} = \underline{e}_{1A}\underline{e}_{2B}$ is the 'polarisation dyad' second rank tensor which can be transferred to an irreducible representation τ_{jm}. Thus, defining the absorptivity :

$$\delta = \sum_{MM'}\sum |A|^2 \qquad 1.10$$

Then:

$$\delta = \sum_{j=0}^{2} \{ \sum_{m=-j}^{+j} |\tau_{jm}|^2 \} \times \{ (2J+1)(2J'+1) | \sum_{k=-j}^{+j} \frac{\begin{pmatrix} J & j & J' \\ -K & k & K' \end{pmatrix}}{(2j+1)^{\frac{1}{2}}} \mathcal{S}_{jk}|^2 \} \qquad 1.1$$

$$\text{or} \quad = P_o Q_o + P_1 Q_1 + P_2 Q_2 \qquad 1.12$$

where the P's depend only on the polarisation and the Q's depend only on the molecular properties. The polarisation functions can be calculated, (McClain and Harris, (Chapter 2, reference [4]) equations (119), (120), (121)) and are:

$$P_0 = \frac{1}{3} |\underline{e}_1 \cdot \underline{e}_2|^2 \qquad 1.13$$

$$P_1 = \frac{1}{2} (1 - |\underline{e}_1 \cdot \underline{e}_2{}^*|^2) \qquad 1.14$$

$$P_2 = \frac{1}{2} (1 + |\underline{e}_1 \cdot \underline{e}_2|^2 - \frac{2}{3} |\underline{e}_1 \cdot \underline{e}_2{}^*|^2) \qquad 1.15$$

APPENDIX II

MATERIALS

HCl - BDH Electronic grade, 99.99% minimum purity.

DCl - MSD Isotopes, 99.5% min. isotopic purity.

5% HCl/Ar - B.O.C. Special Gases.

C_2H_3Cl - Matheson Gases, 99.95 min. purity.

C_2H_3Br - Aldrich Chemicals, 98% min. purity. (with 300-500 ppm hydroquinone monomethyl ether inhibitor).

Ar - B.O.C. Research grade 99.995% min. purity.

Xe - B.O.C. Research grade 99.995% min. purity.

Kr - B.O.C. Research grade 99.995% min. purity.

He - B.O.C. Grade "A" 99.995% min. purity.

Ne - B.O.C. CP grade 99.995% min. purity.

CH_4 - B.O.C. Research grade 99.995% min. purity.

APPENDIX III

TABLE 1.1 HCl F ${}^1\Delta_2$ - X ${}^1\Sigma^+$ (0 - 0)

ROTATIONAL LINE	MEASURED POSITION /cm^{-1}	CALCULATED POSITION /cm^{-1}	RESIDUAL /cm^{-1}
R(1)	82888.09	82888.18	+0.09
R(2)	82908.48	82908.28	-0.20
R(3)	82927.87	82928.02	+0.15
R(4)	82947.24	82947.34	+0.10
R(5)	82966.12	82966.15	+0.03
R(6)	82984.09	82984.33	+0.24
R(7)	83001.52	83001.79	+0.27
R(8)	83018.27	83018.38	+0.11
R(10)	83048.47	83048.36	-0.11
Q(2)	82846.31	82846.44	+0.13
Q(3)	82845.64	82845.70	+0.06
Q(4)	82844.59	82844.64	+0.05
Q(5)	82843.16	82843.20	+0.04
Q(6)	82841.64	82841.32	-0.32
S(0)	82909.31	82909.06	-0.25
S(1)	82950.16	82950.02	-0.14
S(2)	82990.52	82990.61	+0.09
S(3)	83030.93	83030.73	-0.20
S(5)	83109.38	83109.16	-0.22
S(6)	83147.54	83147.23	-0.31
S(7)	83184.52	83184.35	-0.17
S(8)	83220.10	83220.35	+0.25
P(3)	82783.72	82783.85	+0.13
P(4)	82762.45	82762.31	-0.14
P(5)	82740.60	82740.50	-0.10
P(6)	82718.33	82718.28	-0.05
P(7)	82695.72	82695.88	+0.16
P(8)	82672.73	82672.93	+0.20
O(4)	82700.16	82700.47	+0.31
O(5)	82658.06	82658.17	+0.11
O(6)	82615.65	82615.67	+0.02

Reduced $\chi^2 = 1.02$

$T_o = 82847.13 \pm 0.08\ cm^{-1}$

$B_v = 10.328 \pm 0.003\ cm^{-1}$

$D_v = 1.147 \pm 0.029 x 10^{-3}\ cm^{-1}$

TABLE 1.2 DCl F $^{1}\Delta_{2}$ - X $^{1}\Sigma^{+}$ (0 - 0)

ROTATIONAL LINE	MEASURED POSITION /cm^{-1}	CALCULATED POSITION /cm^{-1}	RESIDUAL /cm^{-1}
R(1)	82929.68	82929.77	+0.09
R(2)	82939.40	82939.21	-0.19
R(3)	82948.24	82948.20	-0.04
R(4)	82956.82	82956.72	-0.10
R(5)	82964.68	82964.77	+0.09
R(6)	82972.28	82972.34	+0.06
R(7)	82979.56	82979.43	-0.13
R(8)	82986.08	82986.03	-0.05
R(9)	82992.05	82992.12	+0.07
Q(2)	82908.28	82908.21	-0.07
Q(3)	82906.92	82906.87	-0.05
Q(4)	82905.12	82905.09	-0.03
Q(5)	82902.44	82902.87	+0.43
Q(6)	82899.84	82900.18	+0.34
Q(7)	82896.80	82897.04	+0.24
Q(8)	82893.24	82893.44	+0.20
Q(9)	82889.22	82889.37	+0.15
Q(10)	82884.58	82884.83	+0.25
S(0)	82940.60	82940.55	-0.05
S(1)	82960.96	82960.78	-0.18
S(2)	82980.64	82980.54	-0.10
S(3)	82999.79	82999.82	+0.03
S(4)	83018.96	83018.62	-0.34
S(5)	83037.20	83036.93	-0.27
S(6)	83055.08	83054.73	-0.35
S(7)	83072.48	83072.02	-0.46
S(8)	83088.80	83088.77	-0.03
O(4)	82832.80	82832.77	-0.03
O(5)	82809.72	82809.92	+0.20
P(3)	82876.04	82875.87	-0.17
P(4)	82863.68	82863.77	+0.09
P(5)	82850.92	82851.24	+0.32
P(6)	82838.32	82838.28	-0.04
P(7)	82824.80	82824.88	+0.08
P(8)	82811.03	82811.05	+0.02

Reduced $\chi^{2} = 1.05$

$T_{O} = 82909.54 \pm 0.08$ cm^{-1}

$B_{V} = 5.171 \pm 0.004$ cm^{-1}

$D_{V} = 1.67 \pm 0.35\text{x}10^{-4}$ cm^{-1}

TABLE 1.3 $H^{35}Cl$ F $^1\Delta_2$ - X $^1\Sigma^+$ (1 - 0)

ROTATIONAL LINE	MEASURED POSITION /cm^{-1}	CALCULATED POSITION /cm^{-1}	RESIDUAL /cm^{-1}
R(1)	85403.55	85403.78	+0.23
R(2)	85422.85	85422.84	-0.01
R(3)	85441.09	85441.05	-0.04
R(4)	85458.28	85458.50	+0.22
R(5)	85474.23	85474.68	+0.45
R(6)	85489.06	85489.48	+0.42
Q(2)	85361.81	85362.03	+0.22
Q(3)	85360.22	85360.28	+0.06
Q(4)	85357.65	85357.77	+0.12
Q(5)	85354.50	85354.36	-0.14
Q(6)	85350.01	85349.86	-0.15
Q(7)	85344.34	85344.05	-0.29
S(0)	85424.41	85424.65	+0.24
S(1)	85464.61	85464.609	-0.001
S(2)	85503.53	85503.74	+0.21
S(3)	85541.58	85541.88	+0.30
S(4)	85578.89	85578.82	-0.07
O(5)	85172.84	85172.76	-0.08
O(6)	85129.35	85128.81	-0.54
P(3)	85299.72	85299.45	-0.27
P(5)	85253.92	85253.63	-0.29
P(6)	85229.80	85229.53	-0.27
P(8)	85178.03	85178.08	+0.05
P(9)	85150.32	85150.28	-0.04

Reduced $\chi^2 = 0.98$

$T_0 = 85363.68 \pm 0.17$ cm^{-1}

$B_v = 10.18 \pm 0.01$ cm^{-1}

$D_v = 2.06 \pm 0.16 \times 10^{-3}$ cm^{-1}

TABLE 1.4 $H^{37}Cl$ $F\ ^1\Delta_2 - X\ ^1\Sigma^+$ (1 - 0)

ROTATIONAL LINE	MEASURED POSITION /cm^{-1}	CALCULATED POSITION /cm^{-1}	RESIDUAL /cm^{-1}
R(1)	85401.94	85402.16	+0.22
R(2)	85421.05	85421.12	+0.07
R(3)	85439.31	85439.28	-0.03
R(4)	85456.06	85456.51	+0.45
R(5)	85472.50	85472.56	+0.16
R(6)	85487.08	85487.54	+0.46
Q(3)	85358.24	85358.63	+0.39
Q(4)	85356.06	85356.02	-0.04
Q(5)	85352.74	85352.53	-0.21
Q(6)	85348.25	85348.02	-0.23
Q(7)	85342.78	85342.31	-0.47
S(1)	85462.68	85462.80	+0.12
S(2)	85501.74	85501.77	+0.03
S(3)	85539.60	85539.78	+0.18
S(4)	85576.74	85576.65	-0.09
O(5)	85171.59	85171.39	-0.20
P(3)	85298.11	85297.99	-0.12
P(4)	85275.59	85275.37	-0.22
P(5)	85252.36	85252.04	-0.32
P(6)	85228.07	85227.89	-0.18
P(8)	85176.57	85176.59	+0.02
P(9)	85149.13	85149.07	-0.06

Reduced $\chi^2 = 0.89$

$T_0 = 85362.25 \pm 0.19\ \text{cm}^{-1}$

$B_v = 10.14 \pm 0.01\ \text{cm}^{-1}$

$D_v = 1.76 \pm 0.19\text{x}10^{-3}\ \text{cm}^{-1}$

TABLE 1.5 $D^{35}Cl$ F $^1\Delta_2$ - X $^1\Sigma^+$ (1 - 0)

ROTATIONAL LINE	MEASURED POSITION /cm^{-1}	CALCULATED POSITION /cm^{-1}	RESIDUAL /cm^{-1}
P(4)	84690.32	84690.62	+0.30
P(5)	84677.24	84677.25	+0.01
P(6)	84663.35	84663.24	-0.11
P(7)	84648.64	84648.56	-0.08
Q(2)	84735.91	84735.67	-0.24
Q(4)	84731.13	84731.11	-0.02
Q(5)	84727.84	84727.82	-0.02
Q(6)	84723.85	84723.86	+0.01
Q(7)	84719.36	84719.20	-0.16
Q(8)	84713.80	84713.84	+0.04
Q(10)	84700.96	84700.92	-0.04
Q(11)	84693.31	84693.33	+0.02
R(1)	84757.37	84757.24	-0.13
R(2)	84765.88	84766.06	+0.18
R(3)	84774.05	84774.21	+0.16
R(4)	84781.59	84781.67	+0.08
R(5)	84788.66	84788.44	-0.22
R(6)	84794.69	84794.50	-0.19
R(7)	84799.69	84799.83	+0.14
S(0)	84767.97	84768.02	+0.05
S(1)	84787.88	84787.62	-0.26
S(3)	84824.44	84824.78	+0.34
S(5)	84858.95	84859.09	+0.14

Reduced $\chi^2 = 0.74$

$T_0 = 84737.62 \pm 0.09$ cm^{-1}

$B_v = 5.068 \pm 0.004$ cm^{-1}

$D_v = 2.27 \pm 0.32\times10^{-4}$ cm^{-1}

TABLE 1.6 $D^{37}Cl$ F $^1\Delta_2$ - X $^1\Sigma^+$ (1 - 0)

ROTATIONAL LINE	MEASURED POSITION /cm^{-1}	CALCULATED POSITION /cm^{-1}	RESIDUAL /cm^{-1}
P(5)	84675.20	84675.09	-0.11
P(6)	84660.91	84661.08	+0.17
Q(5)	84725.57	84725.48	-0.09
Q(6)	84721.68	84721.51	-0.17
Q(7)	84717.11	84716.87	-0.24
Q(8)	84711.53	84711.54	+0.01
R(1)	84755.04	84754.90	-0.14
R(3)	84771.70	84771.76	+0.06
R(4)	84779.04	84779.18	+0.14
R(5)	84785.74	84785.91	+0.17
R(6)	84792.07	84791.95	-0.12
R(7)	84797.12	84797.28	+0.16
S(1)	84785.16	84785.17	+0.01
S(2)	84803.86	84804.01	+0.15

Reduced $\chi^2 = 0.69$

$T_0 = 84735.38 \pm 0.20$ cm^{-1}

$B_V = 5.047 \pm 0.012$ cm^{-1}

$D_V = 1.67 \pm 1.38 \times 10^{-4}$ cm^{-1}

Appendix IV

```
c      Program calculates the O,P,Q,R,S branch intensities and positions
c     for a two photon D(OMEGA)=0+ - 0+ or 0+ - 2 electronic transition.
c     It also simulates the spectrum.The unblended line strengths, positions
c     and relative positions are sent to 'HONLLOND', the plotting data is sent
c     to 'PLOT'.
      PARAMETER(NPAR=250)
      IMPLICIT DOUBLE PRECISION(A-H,O-Z)
      DIMENSION B(2),NRB(2),NVL(2),NLAMB(2),RBC(20,2),RDC(20,2)
      DIMENSION OI(NPAR),SI(NPAR),RI(NPAR),QI(NPAR),PI(NPAR)
      DIMENSION OP(NPAR),SP(NPAR),RP(NPAR),QP(NPAR),PP(NPAR)
      DIMENSION NVC(2),VWC(20,2),GV(2),TE(2),NRD(2),D(2)
      COMMON/ALL1/K,I,K1SIGN,RHL,QHL,PHL,OHL,SHL
     1,NRMJ,NQMJ,NPMJ,NOMJ,NSMJ,NLAMB,SUM1,SUM2,SUM3,SUM4,DF
      OPEN(UNIT=7,FILE='DATA')
      OPEN(UNIT=8,FILE='PLOT',FILETYPE='CHARACTER')
      OPEN(UNIT=9,FILE='HONLLOND',FILETYPE='CHARACTER')
    1 FORMAT(' Transitions from V**=',I2,' to V*=',I2//40X,'EJo_o='
     c,F11.4//10X,' Intensities',20X
     c//15X,'R',12X,'Q',12X,'P',12X,'O',12X,'S',12X)
    2 FORMAT(I4)
    3 FORMAT(' Plot lines up to J=',I4)
    4 FORMAT(2X,'J"=',I3,2X,6(G12.6,1X))
    5 FORMAT(2X,'J"=',I3,2X,5(G12.6,1X),3X)
    6 FORMAT(2(G12.6))
    7 FORMAT(I2)
    8 FORMAT(2X,'J"=',I3,2X,3(G20.14,1X))
    9 FORMAT(15X,' For lower level')
   10 FORMAT(15X,' For upper level')
   11 FORMAT(2X,'J"=',I3,2X,2(G20.14,1X),4X,'*****')
   12 FORMAT(//)
   13 FORMAT(10X,' Intensities',15X,' Relative positions (cm-1)')
   14 FORMAT(20X,' Absolute Positions (cm-1)',//)
c     The intensity of the P(0) band is set to zero
c     The data is read in from 'DATA' or the terminal
      PI1=0.0D0
      CALL EMAS3PROMPT('File(1) or Terminal(2):')
      READ*,NN
      IF(NN.NE.1) THEN
      NO1=5
      ELSE
      NO1=7
      ENDIF
      DO 73 J=1,2
      IF(NN.EQ.1) GOTO74
      WRITE(6,*)
      IF(J.EQ.1) THEN
      WRITE(6,9)
      ELSE
      WRITE(6,10)
      ENDIF
   74 WRITE(6,*)
      CALL EMAS3PROMPT('No. of V-,B- & D-constants:')
      READ(NO1,*) NVC(J),NRB(J),NRD(J)
      CALL EMAS3PROMPT ('Vib. constants:')
      READ(NO1,*) ( VWC(I,J), I=1,NVC(J))
      CALL EMAS3PROMPT ('Rot. constants:')
      READ(NO1,*) ( RBC(I,J), I=1,NRB(J))
```

```
      CALL EMAS3PROMPT('Cent. Terms:')
      READ(NO1,*) ( RDC(I,J), I=1,NRD(J))
      CALL EMAS3PROMPT('Te Value:')
      READ(NO1,*) TE(J)
      CALL EMAS3PROMPT('Vib. Level:')
      READ(NO1,*) NVL(J)
      CALL EMAS3PROMPT('OMEGA Value:')
      READ(NO1,*) NLAMB(J)
   73 CONTINUE
      CALL EMAS3PROMPT('Rot. Temp. & Laser Width:')
      READ(NO1,*) T,W
c     The vibrational term value is initialised and then calculated
   30 GV(1)=0.0D0
      GV(2)=0.0D0
      DO 32 J=1,2
      DO 32 K=NVC(J),1,-1
   32 GV(J)=(GV(J)+VWC(K,J))*(NVL(J)+0.5D0)
c     The Bv and Dv constants are initialised and then calculated
      B(1)=0.0D0
      B(2)=0.0D0
      D(1)=0.0D0
      D(2)=0.0D0
      DO 40 J=1,2
      DO 50 I=NRB(J),2,-1
   50 B(J)=(B(J)+RBC(I,J))*(NVL(J)+0.5D0)
      B(J)=B(J)+RBC(1,J)
      DO 55 I=NRD(J),2,-1
   55 D(J)=(D(J)+RDC(I,J))*(NVL(J)+0.5D0)
      D(J)=D(J)+RDC(1,J)
   40 CONTINUE
c     The min. and max. deviations in position from the origin are
c     initialised. The rotationless transition energy is calculated.
      PMIN=10.0D0
      PMAX=-10.0D0
      DIFF=GV(2)-GV(1)+TE(2)-TE(1)
c     The lowest rotational levels in each respective branch
c     for a given 0+ - 0+ or 0+ - 2 electronic transition are
c     determined.
c     The positions of the branches are calculated and the min.
c     and max. deviations calculated.
      NDLAMB=NLAMB(2)-NLAMB(1)
      IF(NDLAMB.EQ.0) THEN
      NRMJ=NLAMB(2)
      NQMJ=NLAMB(2)
      NPMJ=NLAMB(2)+1
      NOMJ=NLAMB(2)+2
      NSMJ=NLAMB(2)
      ENDIF
      IF(NDLAMB.EQ.2) THEN
      NRMJ=NLAMB(2)-1
      NQMJ=NLAMB(2)
      NPMJ=NLAMB(2)+1
      NOMJ=NLAMB(2)+2
      NSMJ=NLAMB(2)-2
      ENDIF
      IF(NDLAMB.EQ.-2)THEN
      NRMJ=NLAMB(1)
```

```
      NQMJ=NLAMB(1)
      NPMJ=NLAMB(1)
      NOMJ=NLAMB(1)
      NSMJ=NLAMB(1)
      ENDIF
      DO 45 I=1,20
      QP(I)=0.0D0
      RP(I)=0.0D0
      PP(I)=0.0D0
      OP(I)=0.0D0
      SP(I)=0.0D0
      K=I-1
      IA=(K+2)*(K+3)
      IB=K*(K+1)
      IC=(K+1)*(K+2)
      ID=K*(K-1)
      IE=(K-1)*(K-2)
      IF(K.GE.NQMJ) THEN
      QP(I)=(B(2)-D(2)*IB)*IB-(B(1)-D(1)*IB)*IB
      ENDIF
      IF(K.GE.NRMJ) THEN
      RP(I)=(B(2)-D(2)*IC)*IC-(B(1)-D(1)*IB)*IB
      ENDIF
      IF(K.GE.NPMJ) THEN
      PP(I)=(B(2)-D(2)*ID)*ID-(B(1)-D(1)*IB)*IB
      ENDIF
      IF(K.GE.NOMJ) THEN
      OP(I)=(B(2)-D(2)*IE)*IE-(B(1)-D(1)*IB)*IB
      ENDIF
      IF(K.GE.NSMJ) THEN
      SP(I)=(B(2)-D(2)*IA)*IA-(B(1)-D(1)*IB)*IB
      ENDIF
      Y=MIN(QP(I),RP(I),PP(I),SP(I),OP(I))
      IF(Y.LT.PMIN) PMIN=Y
      Z=MAX(QP(I),RP(I),PP(I),SP(I),OP(I))
      IF(Z.GT.PMAX) PMAX=Z
   45 CONTINUE
c     The Boltzmann factor BF is calculated.
      NDLAMB=NLAMB(2)-NLAMB(1)
      IF(NDLAMB.EQ.0) THEN
      NRMJ=NLAMB(2)
      NQMJ=NLAMB(2)
      NPMJ=NLAMB(2)+1
      NOMJ=NLAMB(2)+2
      NSMJ=NLAMB(2)
      ENDIF
      IF(NDLAMB.EQ.2) THEN
      NRMJ=NLAMB(2)-1
      NQMJ=NLAMB(2)
      NPMJ=NLAMB(2)+1
      NOMJ=NLAMB(2)+2
      NSMJ=NLAMB(2)-2
      ENDIF
      IF(NDLAMB.EQ.-2) THEN
      NRMJ=NLAMB(1)
      NQMJ=NLAMB(1)
      NPMJ=NLAMB(1)
```

```
      NOMJ=NLAMB(1)
      NSMJ=NLAMB(1)
      ENDIF
      NPLAMB=NLAMB(1)+NLAMB(2)
      N=0
c     An intensity factor is input to terminate the calculation when
c     the intensity of all three branches falls below this value.
      CALL EMAS3PROMPT('Intensity factor:')
      READ(5,*)FAC
      PRINT*,'Damping factor'
      READ(5,*)DF
      WRITE(9,1)NVL(1),NVL(2),DIFF
c     Two photon line strength factors are calculated for D(OMEGA)=0+ - 0+
c     or 0+ - 2 electronic transition.
      DO 60 I=1,20
      BF=1.438789469/T
      N=N+1
      K=I-1
      IB=K*(K+1)
      K1SIGN=-1
      RHL=0.0D0
      PHL=0.0D0
      QHL=0.0D0
      OHL=0.0D0
      SHL=0.0D0
      IF(NDLAMB.EQ.0) CALL HNFAC
      IF(NDLAMB.EQ.2) CALL HNLFAC
      IF(NDLAMB.EQ.-2) THEN
      K1SIGN=1
      CALL HNLFAC
      ENDIF
c     The unblended line intensities are calculated
      TW=-((B(1)-D(1)*IB)*IB*BF)
  100 QI(I)=EXP(TW)*QHL
      RI(I)=EXP(TW)*RHL
      OI(I)=EXP(TW)*OHL
      PI(I)=EXP(TW)*PHL
      SI(I)=EXP(TW)*SHL
c     The condition for termination is applied
      FACMAX=MAX(QI(I),RI(I),PI(I),OI(I),SI(I))
      IF(FACMAX.LT.FAC) GOTO130
      IF(K.LE.20)GOTO 120
c     The intensities and relative positions are sent to 'HONLLOND'
  120 IF(I.GE.1)THEN
      WRITE(9,5)K,RHL,QHL,PHL,OHL,SHL
      WRITE(9,5)K,RI(I),QI(I),PI(I),OI(I),SI(I)
      WRITE(9,4)K,RP(I),QP(I),PP(I),OP(I),SP(I)
      ENDIF
   60 CONTINUE
  130 WRITE(6,3)N
      PRINT*,'Band ranges between ',PMIN,'and ',PMAX,' wavenumbers'
      CALL EMAS3PROMPT('Plotting increment:')
      READ*,STEP
      BEG=PMIN-4.0D0*W
      NUM=(PMAX-PMIN+8.0D0*W)/STEP+0.5D0
      PRINT*,'Number of steps is ',NUM
      CON=1.0D0/(W*SQRT(2.0D0*3.141592654))
```

```
      POS=BEG
c     The 'integrated' signal intensity at step 'STEP' is determined
      DO 150 J=1,NUM
      HINT=0.0D0
      FREQ=POS
      DO 160 I=1,N
      K=I-1
c     The integration is performed
      IF((ABS(FREQ-RP(I))).LE.10.0D0*W) THEN
      HINT=HINT+CON*RI(I)*EXP(-0.5D0*((FREQ-RP(I))/W)**2)
      ENDIF
      IF((ABS(FREQ-PP(I))).LE.10.0D0*W) THEN
      HINT=HINT+CON*PI(I)*EXP(-0.5D0*((FREQ-PP(I))/W)**2)
      ENDIF
      IF((ABS(FREQ-QP(I))).LE.10.0D0*W) THEN
      HINT=HINT+CON*QI(I)*EXP(-0.5D0*((FREQ-QP(I))/W)**2)
      ENDIF
      IF((ABS(FREQ-SP(I))).LE.10.0D0*W)THEN
      HINT=HINT+CON*SI(I)*EXP(-0.5D0*((FREQ-SP(I))/W)**2)
      ENDIF
      IF((ABS(FREQ-OP(I))).LE.10.0D0*W)THEN
      HINT=HINT+CON*OI(I)*EXP(-0.5D0*((FREQ-OP(I))/W)**2)
      ENDIF
  160 CONTINUE
      AFREQ=DIFF+FREQ
      WRITE(8,*) AFREQ,HINT
      POS=FREQ+STEP
  150 CONTINUE
      WRITE(9,12)
      WRITE(9,14)
      DO 170 I=1,N
      QP(I)=QP(I)+DIFF
      RP(I)=RP(I)+DIFF
      PP(I)=PP(I)+DIFF
      SP(I)=SP(I)+DIFF
      OP(I)=OP(I)+DIFF
      WRITE(9,8) I-1,RP(I),QP(I),PP(I),SP(I),OP(I)
  170 CONTINUE
      REWIND(8)
      CALL PLTRDC
      CLOSE(7)
      CLOSE(8)
      CLOSE(9)
  110 STOP
      END
c
c
c
      SUBROUTINE HNLFAC
      IMPLICIT DOUBLE PRECISION(A-H,O-Z)
      DIMENSION NLAMB(2)
      COMMON/ALL1/K,I,K1SIGN,RHL,QHL,PHL,OHL,SHL
     1,NRMJ,NQMJ,NPMJ,NOMJ,NSMJ,NLAMB,SUM1,SUM2,SUM3,SUM4,DF
      IF(K.GE.NRMJ) THEN
      SUM1=((I-1)+K1SIGN*NLAMB(1))
      SUM2=(I-1-K1SIGN*NLAMB(1)+1)
      SUM3=(I-1-K1SIGN*NLAMB(1)+2)
```

```
      SUM4=(I-1-K1SIGN*NLAMB(1)+3)
      RHL=SUM1*SUM2*SUM3*SUM4/(15*(I-1)*(I)*(I+1))
      RHL=RHL/((1+(DF*K*(K+1)))**2)
      ENDIF
      IF(K.GE.NPMJ) THEN
      SUM1=((I-1)+K1SIGN*NLAMB(1))
      SUM2=(I-1+K1SIGN*NLAMB(1)-1)
      SUM3=(I-1+K1SIGN*NLAMB(1)-2)
      SUM4=(I-1-K1SIGN*NLAMB(1)+1)
      PHL=SUM1*SUM2*SUM3*SUM4/(15*(I-1)*(I)*(I-2))
      PHL=PHL/((1+(DF*K*(K+1)))**2)
      ENDIF
      IF(K.GE.NQMJ)THEN
      SUM1=(I-1+K1SIGN*NLAMB(1))
      SUM2=(I-1+K1SIGN*NLAMB(1)-1)
      SUM3=(I-1-K1SIGN*NLAMB(1)+1)
      SUM4=(I-1-K1SIGN*NLAMB(1)+2)*(2*(I-1)+1)
      QHL=SUM1*SUM2*SUM3*SUM4/(5*(I-1)*I*(2*(I-1)-1)*(2*(I-1)+3))
      QHL=QHL/((1+(DF*K*(K+1)))**2)
      ENDIF
      IF(K.GE.NOMJ) THEN
      SUM1=(I-1+K1SIGN*NLAMB(1))
      SUM2=(I-1+K1SIGN*NLAMB(1)-1)
      SUM3=(I-1+K1SIGN*NLAMB(1)-2)
      SUM4=(I-1+K1SIGN*NLAMB(1)-3)
      OHL=SUM1*SUM2*SUM3*SUM4/(30*(I-1)*(I-2)*(2*(I-1)-1))
      OHL=OHL/((1+(DF*K*(K+1)))**2)
      ENDIF
      IF(K.GE.NSMJ) THEN
      SUM1=(I-1-K1SIGN*NLAMB(1)+1)
      SUM2=(I-1-K1SIGN*NLAMB(1)+2)
      SUM3=(I-1-K1SIGN*NLAMB(1)+3)
      SUM4=(I-1-K1SIGN*NLAMB(1)+4)
      SHL=SUM1*SUM2*SUM3*SUM4/(30*I*(I+1)*(2*(I-1)+3))
      SHL=SHL/((1+(DF*K*(K+1)))**2)
      ENDIF
      RETURN
      END
c
c
c
      SUBROUTINE HNFAC
      IMPLICIT DOUBLE PRECISION(A-H,O-Z)
      DIMENSION NLAMB(2)
      COMMON/ALL1/K,I,K1SIGN,RHL,QHL,PHL,OHL,SHL
     1,NRMJ,NQMJ,NPMJ,NOMJ,NSMJ,NLAMB,SUM1,SUM2,SUM3,SUM4,DF
      IF(NLAMB(1).EQ.0)THEN
      RHL=0.0D0
      ELSE IF(K.GE.NRMJ) THEN
      SUM1=NLAMB(1)**2
      SUM2=(I**2-NLAMB(1)**2)
      RHL=2*SUM1*SUM2/(30*(I-1)*I*(I+1))
      RHL=RHL/((1+(DF*K*(K+1)))**2)
      ENDIF
      IF(K.GE.NSMJ)THEN
      SUM1=(I**2-NLAMB(1)**2)
      SUM2=((I+1)**2-NLAMB(1)**2)
```

```
      SHL=SUM1*SUM2/(30*I*(I+1)*(2*(I-1)+3))
      SHL=SHL/((1+(DF*K*(K+1)))**2)
      ENDIF
      IF(K.EQ.NQMJ) THEN
      SUM1=(2*(I-1)+1)
      PRINT*,SUM1
      SUM2=(2*(I-1)+1)
      SUM3=(I-1)*I
      SUM4=(45*(2*(I-1)-1)*(2*(I-1)+3))
      QHL=(SUM1/9)+((SUM2*SUM3)/SUM4)
      QHL=QHL/((1+(DF*K*(K+1)))**2)
      ELSE IF(K.GT.NQMJ)THEN
      SUM1=(2*(I-1)+1)
      SUM3=(((I-1)*I)-(3*(NLAMB(1)**2)))**2
      SUM2=(2*(I-1)+1)
      SUM4=(45*(I-1)*I*(2*(I-1)-1)*(2*(I-1)+3))
      QHL=(SUM1/9)+((SUM2*SUM3)/SUM4)
      QHL=QHL/((1+(DF*K*(K+1)))**2)
      ENDIF
      IF(NLAMB(1).EQ.0)THEN
      PHL=0.0D0
      ELSE IF(K.GE.NPMJ)THEN
      SUM1=NLAMB(1)**2
      SUM2=((I-1)**2-NLAMB(1)**2)
      PHL=2*SUM1*SUM2/(30*(I-1)*I*(I-2))
      PHL=PHL/((1+(DF*K*(K+1)))**2)
      ENDIF
      IF(K.GE.NOMJ)THEN
      SUM1=((I-1)**2-(NLAMB(1)**2))
      SUM2=((I-2)**2-(NLAMB(1)**2))
      OHL=SUM1*SUM2/(30*(I-1)*(I-2)*(2*(I-1)-1))
      OHL=OHL/((1+(DF*K*(K+1)))**2)
      ENDIF
      RETURN
      END
c
c
c
      SUBROUTINE PLTRDC
      IMPLICIT DOUBLE PRECISION (A-C)
      DIMENSION B(20000),C(20000),D(20000),E(20000),F(20000),G(20000)
      A=0.0D0
      N=0
      DO 10,I=1,20000
      READ(8,*,END=15) B(I),C(I)
      N=N+1
      D(I)=B(I)
      IF(C(I).GT.A) THEN
      A=C(I)
      ENDIF
   10 CONTINUE
   15 DO 20,I=1,N
      C(I)=C(I)/A
      IF(C(I).LT.1.0D-03) THEN
      E(I)=0.0
      ELSE
      E(I)=C(I)
```

```
      ENDIF
   20 CONTINUE
      IK=0
      DO 30,I=1,N
      IF(E(I).NE.0.0) GOTO31
   30 CONTINUE
   31 IK=I
      IL=0
      DO 40,I=N,1,-1
      IF(E(I).NE.0.0) GOTO41
   40 CONTINUE
   41 IL=I
      REWIND(8)
      DO 50,I=IK,IL
   50 WRITE(8,*) D(I),E(I)
      REWIND(8)
      CALL OUTPUT
      RETURN
      END
C
C
C
      SUBROUTINE OUTPUT
      CHARACTER*40 FILE,FILE2(40)*1
      EQUIVALENCE (FILE,FILE2)
      DIMENSION D(20000),E(20000)
      OPEN(UNIT=11,FILE='TEMP',FILETYPE='CHARACTER')
    1 FORMAT(A40)
    2 FORMAT(I1)
      CALL EMAS3PROMPT('Base Output File: ')
      READ(5,1) FILE
      DO 10,I=40,1,-1
      IF(FILE2(I).NE.' ') THEN
      K=I+1
      GOTO 11
      ENDIF
   10 CONTINUE
   11 L=2
   12 L=L+1
      IF(L.LT.10) THEN
      WRITE(FILE2(K),2) L
      ELSE
      LL=L-10
      L1=1
      WRITE(FILE2(K),2) L1
      WRITE(FILE2(K+1),2) LL
      ENDIF
      KN=0
      DO 20,I=1,1000
      READ(8,*,END=21) D(I),E(I)
      KN=KN+1
      WRITE(11,*) D(I),E(I)
   20 CONTINUE
      REWIND(11)
      CALL EMAS3('COPY','TEMP,'//FILE,IHG)
      GOTO 12
   21 DO 30,I=1,KN
```

```
30 WRITE(11,*) D(I),E(I)
   REWIND(11)
   CALL EMAS3(‘COPY’,‘TEMP,’//FILE,IHG)
   RETURN
   END
```

LECTURES ATTENDED

In accordance with the regulations of the University of Edinburgh, Department of Chemistry, the post-graduate lecture courses etc. attended during the period of study are as listed below.

1. Rydberg-Klein-Rees (RKR) Methods.
2. Least Squares Methods.
3. Molecular Electronics.
4. Lasers.
5. Numerical Methods.
6. Signal Processing.
7. Mass Spectrometry.
8. Micro-computing.
9. Scientific German.
10. SERC Sponsored Short Course on Gas Kinetics (July 1985).

In addition many of the regular departmental seminars and all of the laser group meetings were attended.

CONFERENCES ATTENDED

1. Faraday Division, Gas Kinetics Discussion Group Meeting, Leicester (Jan. 1985).
2. Faraday Divison, Gas Kinetics Discussion Group Meeting, Cambridge (July 1985).
3. Faraday Division, High Resolution Spectroscopy Group Meeting, York (December 1985).
4. 9th Internationl Symposium on Gas Kinetics, Bordeaux, France (July 1986).
5. Faraday Division, Gas Kinetics Discussion Group Meeting, Edinburgh (July 1987).
6. 11th International Symposium on Molecular Beams, Edinburgh (July 1987).